Ph. D DISSERTATION

# Numerical analysis of nonlinear fiber laser systems in the ultrashort pulse regime

## 초단 펄스 영역에서 비선형 광섬유 레이저 시스템의 수치해석 연구

By

YOUNGCHUL KWON

AUGUST 2017

DEPARTMENT OF ELECTRICAL AND

COMPUTER ENGINEERING

COLLEGE OF ENGINEERING

SEOUL NATIONAL UNIVERSITY

# Abstract

## Numerical analysis of nonlinear fiber laser systems in the ultrashort pulse regime

YOUNGCHUL KWON
DEPARTMENT OF ELECTRICAL AND
COMPUTER ENGINEERING
COLLEGE OF ENGINEERING
SEOUL NATIONAL UNIVERSITY

In this dissertation, nonlinear fiber laser systems in the sub-ps pulse regime are numerically investigated. The main research subjects of this dissertation are categorized into two groups: (1) nonlinear effects in noncavity configurations, e.g. nonlinear fiber sections pumped by ultrashort pulses and (2) nonlinear effects in cavity configurations, e.g. mode-locked fiber ring lasers. When the systems accompany large amount of nonlinearity, the nonlinear effects result in extreme spectral broadening, called supercontinuum generation (SCG) for the former case and multi-pulse operation for the latter case. By exploiting the master equations based on the nonlinear Schrödinger equation (NLSE), I numerically simulate the ultrashort-pulse evolution in the nonlinear fiber laser systems. By analyzing the simulation results, I optimize the system performance or verify unclarified phenomenon in the investigated systems.

In the first two parts of the dissertation, I focus on studying the SCG in noncavity configurations. First, I numerically study the dynamics of SCG for a variety of possible combinations of photonic crystal fibers (PCFs) and ultrafast fiber laser pulses that current technologies offer. Three types of PCFs typically used in SCG and four representative types of ultrafast fiber laser pulses are considered for this combinatorial study. I numerically model and qualitatively discuss the nonlinear evolution of the pulses for their 12 combinatorial cases. I also quantitatively analyze their output spectra and organize a performance chart for them in terms of spectral bandwidth, flatness, and degree of spectral coherence. Through these works, I suggest the most viable combinations among the given PCFs and ultrafast fiber laser pulses in order to generate a target SC spectrum for various specific cases.

In the second part of this dissertation, I numerically study the dynamics of SCG in a ytterbium-doped highly nonlinear PCF (HNL-PCF) in the sub-ps regime. I disucss the enhancement of the energy spectral density and the recovery of the peak power depletion in the SCG process through the fiber in comparison with the SCG based on a passive-type fiber. As a unique application of the novel characteristics of the active HNL-PCF, I also analyze the direct amplification of a SC pulse through it, showing that the incident SC pulse can be amplified by 10 dB without undergoing significant degradations in terms of spectral bandwidth and flatness. These numerical investigations on the active HNL-PCF will be helpful for opening up new opportunities for fiber-based SCG

technology in the sub-ps pulse regime.

In the third part of this dissertation, I focus on the nonlinear effects in cavity configurations. I numerically investigate quasi-mode-locked (QML) multi-pulse dynamics in a fiber ring laser in the anomalous dispersion (AD) regime. I show that the laser cavity can operate in five constitutively different QML regimes, depending on the saturation power of the saturable absorber element and the length of the passive fiber section that parameterize the overall nonlinearity and dispersion characteristics of the laser cavity. I classify them into the incoherent noise-like pulse (NLP), partially-coherent NLP, symbiotic, partially-coherent multi-soliton, and coherent multi-soliton regimes, accounting for their coherence and multi-pulse formation features. In particular, I numerically clarify and confirm the symbiotic regime for the first time to the best our knowledge, in which NLP and multi-solitons coexist stably in the cavity that has recently been observed experimentally. Furthermore, I analyze the shot-to-shot coherence characteristics of the individual QML regimes relative to the amount of the nonlinear-phase shift per roundtrip, and verify a strong correlation between them. I also show that the net-cavity dispersion plays a critical role in determining the multi-pulse dynamics out of the partially-coherent NLP, symbiotic, and partially-coherent multi-soliton regimes, when the cavity bears moderate nonlinearity. I quantify and visualize all those characteristics onto contour maps, which will be very useful and helpful in discussing and clarifying the complex QML dynamics.

In the fourth part of this dissertation, I extend the analysis of the AD QML cavity into the normal-dispersion (ND) QML cavity. While adjusting two chosen cavity parameters: saturation power of the SA and the length of the ND passive fiber, I verify three distinctive QML operation regimes. Accounting for the temporal dynamics in three QML regimes, I classify them into the NLP, transient, and symbiotic regimes. In each regime, I quantitatively analyze the shot-to-shot stability of the QML pulse and its relation with the cavity nonlinearity by visualizing the results on contour maps. Finally, I discuss the origin of the degradation of the shot-to-shot stability in the ND QML cavity.

Keywords : Nonlinear fiber optics, fiber lasers, ultrashort pulses, fiber amplifiers, mode-locked lasers
Student Number : 2011-20791

# Contents

# List of Figures

# List of Tables

# Chapter 1

# Introduction

## 1.1 Overview on fiber optics

An optical fiber is a cylindrical waveguide, capable of transmitting optical signal through itself. Since the demonstration of the low-loss fiber confining light by total-internal-reflection [1], optical fibers have led huge research attention as a reliable and flexible transmitting medium of optical signal and found numerous applications in optical sensing, spectroscopy, imaging, and so on [2,3]. Thanks to extensive experimental and theoretical studies up to date [4-6], principles of signal propagation through an optical fiber are now well-understood and easily predictable. According to the studies, there exist various fiber optic effects that modulate optical signal in propagation. Those effects are categorized into two areas: linear fiber-optic effects and nonlinear fiber-optic effects [4-6]. Those effects simultaneously and continuously occur through the fiber and cause modulation of optical signal in the temporal and spectral domains. In this section, I provide brief explanation of those fiber-optic effects. I note that the theoretical analysis of signal evolution under the fiber-optic effects can be

carried out by NLSE [6], which will be explained in section 3 and 4 with more details.

### 1.1.1 Linear fiber-optic effects

While an optical signal propagating along a fiber, the temporal characteristics of the signal such as pulse duration, peak power, pulse shape, etc., can be changed by various linear fiber optic effects. There exist mainly three types of linear fiber-optics effects, which are loss, gain, and dispersion, as shown in Fig. 1.1.1.

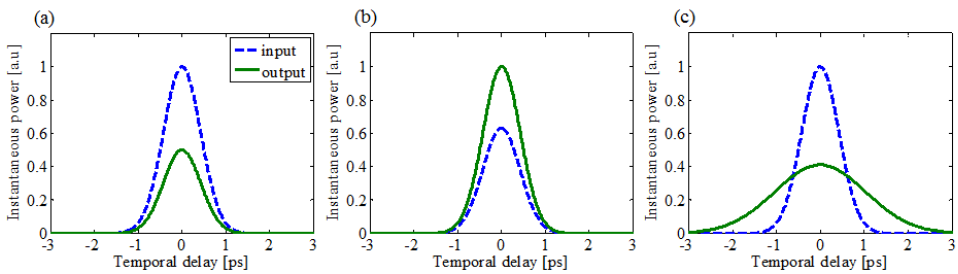


Fig. 1.1.1. Linear fiber-optic effects in the temporal domain by (a) loss, (b) gain, and (c) dispersion.

Fiber loss causes attenuation of an optical signal power and originates from absorption and scattering. Its amount critically depends on the working wavelength. In this thesis, taking account of the working wavelength of conventional fiber lasers, the signal wavelength is considered to be either 1.06 $\mu$m or 1.55 $\mu$m and the length of fibers under consideration is a few meter. Under this circumstance, the fiber loss is not significant if the chosen fibers are typical silica-based fibers [7]. Thus, in this thesis, the fiber loss effect is not included in the analysis. However, I note that if the fiber material is not typical silica (e.g. soft glass types) [8] or the

signal interacts with metal [9], the loss effects can be noticeable even within a few meter of propagation length.

If a fiber is an active type, in which rare-earth (RE) ions are doped, the optical signal inside the fiber would be under the gain effect. The gain increases the power of the signal until the signal power reaches the saturation level. If the bandwidth (BW) of the signal is comparatively narrow to the gain BW, the gain effect can be simply considered as an exponential factor multiplied to the signal. Whereas, if a pulse signal is in the sub-ps regime, the signal BW would be comparable with the gain BW. For that case, the gain effect should be rigorously considered in the spectral domain in which the gain has a profile with a finite BW. This issue will be discussed in section 2.2.2 with more details.

Dispersion is an effect leading the temporal dispersion of a pulse signal, originated from the difference in the group velocities of the various signal contents. Typically, the difference in the group velocity comes from the different wavelength location of the signal contents. Thus, the broader the pulse BW is, the more significant the dispersion is. The dispersion can be categorized in terms of its origin. The most dominant contribution to the dispersion is material dispersion, coming from that the refractive index of material is a function of the wavelength. On the other hand, depending on the wavelength, spatial profile of the signal becomes different, i.e. confinement of the signal to the core becomes different, resulting in that the effective refractive index of the signal becomes a function of the wavelength. This kind of dispersion is called as waveguide

dispersion. Usually, the material dispersion and the waveguide dispersion are regarded together, called as chromatic dispersion. In addition to the chromatic dispersion, there exist other kinds of dispersion, in which the difference of the group velocity comes from the other factors, such as modal dispersion and polarization-mode dispersion [10]. In this thesis, fibers are assumed to be single mode fiber (SMF) without any degenerated polarization states. Thus, as the dispersion effect, I only consider the chromatic dispersion in this thesis.

### 1.1.2 Nonlinear fiber-optic effects

In optical fibers, signal propagates while being confined within a tight core. In other words, the signal can have high intensity and interaction length long enough to achieve nonlinear effects. In this regard, optical fibers can be thought as a nonlinear medium. Nonlinearity in optical fibers is third order, in which variation of the refractive index is proportional to the intensity of optical signal, because of the centrosymmetry of the optical fibers [6,10]. The nonlinear fiber-optic effects mainly cause either spectral broadening or generation of new spectral contents, as shown in Fig. 1.1.2.

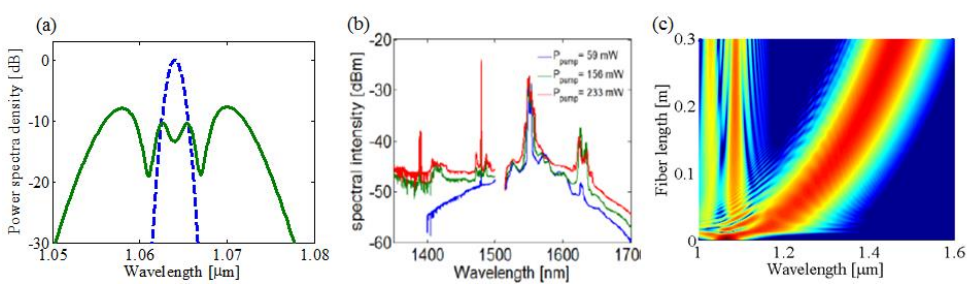

Fig. 1.1.2. Nonlinear fiber-optic effects in the spectral domain by (a) SPM, (b) FWM, and (c) SSFS.

One of the most dominant nonlinear effects is self-phase modulation (SPM), resulting in nonlinear phase accumulation whose amount is proportional to the signal intensity. The nonlinear phase induces a change of instantaneous frequency, resulting in broadening of spectrum. I note that the SPM itself does not changes temporal intensity profile of pulses but change temporal phase and spectral shape, contrasting to the case of the dispersion that change spectral phase and temporal pulse shape. Depending on the type of the dispersion, the effects from the SPM and the dispersion can be either enhanced or suppressed. When the dispersion is normal, the temporal broadening of pulse is boosted, whereas in the anomalous dispersion (AD) regime, a part of nonlinear phase can be canceled by the dispersion, eventually forming a stationary pulse called as soliton [11].

Four-wave mixing (FWM) is a nonlinear interaction in which four frequency components are involved. Typically, the intense frequency component is called as pump and two newly arisen components are called as signal and idler. In the view point of my study, the input pulse corresponds to the pump and it generates signal and idler that are away from the input spectrum. In the temporal domain, the FWM can be thought to form different harmonic components away from the central frequency component, which results in pulsing of the input pulse, called as modulation

instability (MI). It is noteworthy that the FWM can be achieved only if both the frequency matching and phase matching conditions are satisfied [6,10]. Generally speaking, those conditions can be fulfilled with only AD condition [6].

The aforementioned nonlinear effects are based on optical Kerr effect, whereas there exists another group of nonlinear effects based on inelastic scattering. Two kinds of nonlinear scattering effects in optical fibers are Brillouin scattering and Raman scattering. The former is originated from the interaction between light and material waves, resulting in the frequency shift of the signal in GHz level. Taking account of that the signal BW in the sub-ps regime is in THz level, the Brillouin scattering effect is ignorable for ultrashort pulses. Whereas the latter is a scattering of a photon from molecules and the shifting frequency ranges in THz level. For the ultrashort pulses, it leads shifting of pulse spectrum toward longer wavelength side, called as intrapulse Raman scattering (IRS). If the dispersion is anomalous, the IRS can be continuously induced in the form of soliton, called as soliton self-frequency shift (SSFS). SSFS can cause significant spectral broadening over the wavelength range of few hundreds nm, playing an important role in the area of supercontinuum (SC) generation (SCG) [12].

## 1.2 Motivation of this dissertation

As discussed in the last section, various fiber-optic effects can be supported while a signal propagating through a fiber. In particular,

nonlinear effects can be induced when the signal is intense enough. Since the amount of the nonlinearity is proportional to the signal peak power, the sub-ps pulses having narrow pulse width and high peak power are easily affected by the nonlinear effects. In other words, the nonlinear effects are necessarily considered in the fiber laser systems supporting sub-ps pulses. The nonlinear fiber laser systems can be categorized into two configurations: noncavity configurations and cavity configurations. In the former, input sub-ps pulse propagates along a nonlinear fiber section and its spectrum is modulated by the nonlinear effects. If the nonlinearity becomes intense enough, the spectrum is extremely broadened, resulting in the SCG [12]. Whereas, in the latter, a sub-ps pulse circulates within a cavity. In that case, the nonlinearity tends to disturb stable single pulse operation and causes multi-pulse formation [13]. In this thesis, I numerically simulate the both types of nonlinear fiber laser systems and analyze their operations in various system conditions.

The SCG supported by noncavity fiber laser configurations is an extreme spectral broadening process based on the nonlinear effects, even realizing an octave spanning of a pulse spectrum [14]. Since 2000, the combination of ultrafast fiber lasers and photonic crystal fibers (PCFs) has led revolution of the SCG in the sub-ps regime. Up to date, various types of SC spectra have been demonstrated in fiberized systems and numerical analysis has been carried out for physical interpretation of the various SCG process [12]. Consequently, SCG has been continually optimized and improved in

terms of its output performance such as BW, coherence, spectral flatness (SF), etc. However, there still exist insufficiencies to be explored further, despite of the extensive studies up to date.

First, in previous studies, fiber characteristics and pulse characteristics have not been combinatorially but individually considered. In particular, differences in SCG depending on various ultrashort pulse types obtained from conventional fiber lasers have not yet been studied. Conventional ultrafast fiber lasers can support following four type of pulses: soliton, Gaussian, similariton, dissipative soliton. As those four types of pulses have different spectra and pulse shapes, i.e. initial state of SCG becomes different; the resultant SC spectrum can be significantly altered. In addition, there have been extensive studies in SCG based on various types of PCFs diversified in terms of dispersion profiles. In this thesis, I consider both the input pulse types and the PCF types together as critical factors for the SCG. I numerically simulate SCG through various combinations of the ultrashort pulses and the PCFs and quantify the performance of the resultant SCG. From this study, I suggest the most viable combinations of the ultrashort pulses and the PCFs.

Second, there has never been research about active-fiber-based SCG in sub-ps pulse regime. In fact, active-fiber-based SCG is recently attracting research attention as a novel SCG platform [15-22]. Those previous works have been carried out in relatively long pulse regimes: ns, sub-ns and ps regimes and have not yet been extended into sub-ps regimes, which implies that the

active-fiber-based SCG research is still in the early stage. Taking account of previous works [12,23],sub-ps pulses exploited for active-fiber-based SCG can allow faster and broader spectral evolution. Moreover, if the active fiber is realized in a PCF format, its dispersion and nonlinearity characteristics can also be tailored more sophisticatedly, which will further enhance or diversify the resultant SC characteristics. Hence, in this thesis, I numerically simulate SCG through an active highly nonlinear PCF (HNL-PCF) and analyze the effects of RE-ion gain in the SC evolution. From this study, I verify the potential improvements of the SCG by adopting the proposed active fiber in the sub-ps regime.

Now I turn my attention on nonlinear fiber ring cavity configurations. Up to date various operation regimes in fiber ring cavities have been demonstrated, which includes mode-locked regimes, quasi-mode-locked (QML) regimes [13], Q-switching regimes, CW regimes, and so on. In this thesis, I focus on the quasi-mode-locked regimes and analyze alternation of the sub-regimes depending on the cavity conditions by means of numerical simulations. I note that I study both an AD cavity and a normal dispersion (ND) cavity. For both types of nonlinear cavities, I quantify the phase stability of QML pulses and nonlinear phase shift (NPS) per RT. Then, by analyzing the relation between two quantities, I draw conclusions about the effects of cavity nonlinearity on the QML operations.

## 1.3 Scope and organization

The contents of this dissertation cover the nonlinear fiber-optic effects in the sub-ps pulse regime, especially focusing on the SCG in noncavity configuration and QML operation in cavity configurations.

In Chapter 2, I numerically investigate the extreme nonlinear spectral broadening: SCG in the sub-ps pulse regime. In Ch. 2.1, as the nonlinear medium, I consider three types of passive PCFs and as the input pulse, I consider four types of ultrashort pulses generated from conventional ultrafast fiber lasers. For those twelve combinations of the PCFs and the ultrashort pulses, I simulate the SCGs and quantitatively analyze their output performance. In Ch. 2.1.1, I explain numerical model to simulate the SCG in the sub-ps pulse regimes and introduce the characteristics of the PCFs and ultrashort pulses in consideration. In Ch. 2.1.2, I show the SC outputs of all cases by means of spectrogram and modulus of first order degree of coherence (MDOC). In Ch. 2.1.3, I quantify the performance of SCG in each case in terms of 20-dB BW, SF, and MDOC. With those results, I suggest most viable combinations for the SCG.

In Ch. 2.2, I numerically investigate SCG evolution through an active HNL-PCF in the sub-ps regime. In Ch. 2.2.1, I introduce numerical model to rigorously consider both the nonlinear effects and the RE-ion gain effect. In Ch. 2.2.2, by comparative analysis in temporal and spectral domains, I verify potential improvement of

the SCG coming from the addition of the gain effect. Furthermore, I numerically simulate the amplification of a SC spectrum, exploiting the active HNL-PCF. In Ch. 2.2.3, I summarize the overall simulation results.

In Ch. 3, I investigate the nonlinear fiber cavity systems, focusing on QML multi-pulse dynamics. In Ch 3.1, I numerically investigate multi-pulse dynamics and shot-to-shot coherence property in an AD fiber ring cavity. In Ch. 3.1.1, I explain the numerical model for the simulation of QML operation in a fiber ring cavity and provide the cavity conditions in details. In 3.1.2, I demonstrate five distinctive QML regimes obtained from different saturation power of the saturable absorber (SA) and length of the SMF. I also analyze the phase stability of the multi-pulses in the five regimes, with two-dimensional map of the MDOC. Then, I discuss the relation of the MDOC and the NPS of multi-pulses per each RT.

In Ch. 3.2, I numerically investigate QML dynamics and shot-to-shot coherence property in a ND fiber ring cavity. In Ch. 3.2.1, I introduce the model of the ND fiber ring cavity under the consideration. In 3.2.2, by adjusting the cavity conditions, I demonstrate the alternation of the cavity operation regimes and analyze the phase stability of the QML pulses by means of the MDOC. Then, I discuss the origin of the coherence degradation of the QML pulses in the ND cavity.

Finally, In Ch 4, I summarize my research and draw conclusions.

# Chapter 2

# Nonlinear dynamics in noncavity configurations: Supercontinuum generation

Noncavity nonlinear fiber laser systems can be implemented by applying an intense pulse signal to a nonlinear medium, resulting in an extreme spectral broadening: SCG. In this study, I consider sub-ps pulses as the input signal. For the nonlinear medium, three types of conventional passive PCFs are chosen in section 2.1. Then, in section 2.2, an active-type HNL PCF is exploited to achieve SCG. In both types of PCFs, the performance of the output SC spectra is quantitatively discussed.

## 2.1 Passive supercontinuum generation in the sub-ps regime

SCG is based on the extensive spectral broadening by a multitude of nonlinear effects, such as SPM, FWM, Raman scattering, MI, soliton fission, etc. Over the past decade, it has received a lot of research attention owing to its novel characteristics applicable to a variety of different areas of science and technology, such as microscopy [24], optical coherence tomography [25], metrology [26],

telecommunications [27], biomedicine [28], etc. In principle, this novel nonlinear phenomenon is an outcome of a photonic circuitry comprising a HNL medium and a light source of massive instantaneous power, i.e., a high-peak-power laser source. In this regard, the resultant SC spectra are critically affected not only by the individual characteristics of the nonlinear medium and the high-peak-power laser used but also by how they are paired as a combined unit. In fact, many different combinations are possible for it. As for the nonlinear medium, one can use crystals, gases, optical fibers, etc., and as for the ultrafast laser source, one can use all different forms of high-peak-power lasers in terms of their temporal and spectral characteristics [29-37]. Amongst various viable configurations, all-fiberized formats based on optical fibers intensely pumped by fiber-based high-peak-power lasers have emerged as a frequent choice for SCG, because of their compactness as well as high efficiency [37-50]. This success has been led by the advances in two important technologies, namely, PCF technology and ultrafast fiber laser technology.

PCF technology has enabled optical fibers to have tailored nonlinearities and dispersions, which are crucial factors in determining the conversion efficiency of SCG and its spectral characteristics [39-52]. In particular, a distinctive feature of PCFs is the fact that they can be designed and engineered to have zero-dispersion wavelengths (ZDWs) close to the typical operating wavelengths of Ti:sapphire lasers [39-42] or ytterbium(Yb)-doped fiber (YDF) lasers [43-45], which can eventually lead to an

AD regime at the pump wavelength. SCG seeded by femtosecond pulses in the AD regime near the ZDW is dominated by soliton dynamics and results in ultra-broad spectra that are often in excess of even an optical octave span [40]. Although the SCG through this kind of PCFs can readily give rise to extremely wide spectral broadening, its spectral characteristics (e.g., flatness and degree of coherence) strongly depend on the input signal [40,43-46. For example, in the femtosecond regime, input pulses with a low soliton order (i.e., pulse widths ~ 50 fs or N << 16) benefit from an initial spectral broadening arising from SPM and soliton fission effects while reducing MI seeded from noise [40]. The resulting spectral shape in these cases is highly structured due to the low soliton order of the input pulse, while the degree of spectral coherence is high due to the suppression of MI-induced noise amplification. On the contrary, longer pulses (i.e., pulse widths > 150 fs or N > 16) used as an initial seed, can develop flatter spectral structures but with lower degree of spectral coherence [40]. This is due to the fact that SCG seeded with such long pulses can develop an initial spectral broadening arising from MI seeded from noise. In addition, the complex interaction of higher-order solitons and dispersive waves (DWs), by means of cross-phase modulation (XPM), eventually leads to spectral shapes with fine spectral content [40], [43]. In order to deal with these issues, various research groups have investigated fibers with modified dispersion profiles that can enhance nonlinear effects, such as SPM and FWM, together with the stabilization of spectral broadening

[47−51]. For example, the use of PCFs having two ZDWs can suppress the unnecessary noise amplification as well as pulse splitting in the time domain [47,48]. Unfortunately, the spectral broadening process dominated by FWM in these PCFs tends to form a significantly wide spectral depletion near the input radiation wavelength, and thus the resultant spectra are not evenly flat. Meanwhile, all−ND (ANDi) fibers have alternatively been considered for SCG [49,50]. For example, it has been shown that pulse preserving flat−top spectra can be achieved in these PCFs via the SPM−dominant spectral evolution. Yet, their spectral BWs are a bit limited [49].

On the other hand, the ultrafast fiber laser technology has offered efficient and compact, coherent light sources emitting high energy pulses within a very short duration of time, which are ideal for pumping the aforementioned PCFs. In general, the ultrashort pulse characteristics from these sources are determined by their cavity properties, such as dispersion, NPS, and amplitude modulation along the cavity fiber [53−61]. To date, various different types of ultrashort pulses have been achieved, depending on the cavity properties [53,57,60]. In particular, taking account of the cavity dispersion map as well as the pulse evolving feature inside the cavity, the pulse types are often categorized into the following four groups [57]: Soliton, Gaussian, similariton, and dissipative soliton pulses. Soliton pulses, a type of well−known stationary wave solutions obtained out of the NLSE, are generally supported by AD cavities [53,57]. In fact, the soliton formation is

based on the balance between the dispersion detuning and the NPS in the cavity for each round trip, so that there is a limitation on the maximum obtainable pulse energy [53,57]. To reduce the nonlinearity and to scale up the pulse energy, a section of fiber with ND is inserted into the AD cavities. In these cavities, one can obtain breathing pulses with a Gaussian profile [53,54,57]. If the ND property prevails to form ND cavities, one can obtain self-similar pulses with significantly higher pulse energy, i.e., similariton pulses [55-57]. These pulses evolve through the cavity while maintaining their parabolic pulse shape. In ANDi cavities, one can further obtain so-called dissipative soliton pulses that can reach even higher pulse energy, e.g., >10 nJ [57,58].

Considering the wide range of differences in the available technologies for PCFs and ultrafast fiber lasers, one may sensibly raise a question about what combination amongst them will make the best-optimized performance for a targeted SC radiation. In other words, one can significantly improve and optimize the characteristics of the SC radiation in a desired direction by means of making most of the PCFs and ultrafast fiber lasers that are currently available. In principle, it is noteworthy that the characteristics of a PCF determine the nonlinearity and dispersion coefficients in the NLSE whereas those of a ultrafast fiber laser determine the initial conditions of the pumping pulses. Whilst both characteristics are crucial for efficient SCG at the same time, the investigations to date have mostly considered each factor individually or separately. In fact, a variety of novel types of PCFs

have been introduced and investigated for SCG in recent years [40,44,52]; however, little attention have been paid to the consequence of the use of different types of ultrashort pulses except for a handful of cases that exploited the effects of the extra modulation of the ultrashort pulses [62–64].

Here I carry out a combinatorial study for SCG, which is based on various types of the currently available, state–of–the–art PCFs and ultrafast fiber lasers. I numerically analyze the consequences of the different combinations of PCFs and ultrafast fiber lasers in order to improve their SCG characteristics in terms of three primary parameters that can represent the characteristic properties of the generated SC spectrum: its spectral BW, flatness, and degree of spectral coherence. For this study, I take into consideration three and four typical types of PCFs and ultrafast fiber lasers, respectively. As for the PCFs, I consider (1) AD near a single ZDW with a negative slope, (2) flattened all–ND (FAND) with no ZDW, and (3) flattened AD (FAD) with two ZDWs, which are basically named after the dispersion property at the input radiation wavelength. As for the ultrafast fiber lasers, I consider (1) soliton, (2) Gaussian, (3) similariton, and (4) dissipative soliton pulses. (In principle, one can say that the first two pulse types form a family group generated from net AD cavities and the last two form a family group generated from net ND cavities.) For each combination amongst the PCFs and the ultrashort pulses from fiber lasers, I analyze its SCG dynamics, utilizing a numerical model based on the generalized NLSE (GNLSE) [6,12]. Through this combinatorial

study and via quantitative comparisons, I suggest what combinations amongst the PCFs and the ultrafast fiber lasers be considered for the best performance in terms of spectral BW, SF, and MDOC of the output spectrum.

### 2.1.1 Numerical model

I solve the GNLSE to analyze the pulse evolution in optical fibers, which is given by [6]

$$\frac{\partial U}{\partial z}+\sum_{m=2}^{\infty}\frac{i^{m-1}}{m!}\beta_m\frac{\partial^m U}{\partial T^m} = i\gamma\left(1+i\tau_{shock}\frac{\partial}{\partial T}\right)\left[U(z,T)\int_{-\infty}^{\infty}R(T')|U(z,T-T')|^2dT'\right], \quad 2.1.(1)$$

where the left-hand side of the equality corresponds to the linear responses that include the consequences by the group velocity dispersion (GVD) and higher-order dispersion (HOD), whereas the right-hand side corresponds to the nonlinear responses that include the effects of SPM, FWM, self-steepening, and Raman scattering. The parameter ɣ is the nonlinear coefficient, determined by Kerr coefficient of material and effective area of the signal mode [6]. In my simulation, the parameter ɣ is kept constant as a function of wavelength. The parameter τshock is associated with the self-steepening effect and is characterized by $1/\omega_0$ [12] while the parameter R(T) is the nonlinear response function which is defined by [6]

$$R(T)=(1-f_R)\delta(T)+f_R h_R(T), \quad 2.1.(2)$$

where $(1-f_R)\delta(T)$ corresponds to the electronic response of the nonlinear medium and $f_R h_R(T)$ represents the Raman effects. The

Raman response function hR(T) is represented by

$$h_R(T) = \frac{\tau_1^2+\tau_2^2}{\tau_1\tau_2^2}\exp\left(-\frac{T}{\tau_2}\right)\sin\left(\frac{T}{\tau_1}\right), \qquad 2.1.(3)$$

with $\tau_1$= 12.2 fs, $\tau_2$= 32 fs typically for silica fibers in general [6].

It is noteworthy that I hereafter assume for my numerical simulations an input radiation with the following characteristics: 1064−nm central wavelength, 200−fs pulse width, and 10 kW peak power. The fiber lengths under investigation are within 0.3 m, adjusted to set the maximum NPS $\phi_{\max} = \gamma \cdot P_0 \cdot L_{\text{fiber}} = 70$. For our case of study, the HOD parameters beyond $\beta_4$ can be neglected without loss of generality, because their dispersion lengths become even longer than several tens of meters. In addition, I ignore multi−modal and polarization effects, i.e. I assume a single−mode and single−polarization operation for all cases. With this hypothesis, I obtain the master equation of my whole simulation, plugging Eq. 2.1.(2) into Eq. 2.1.(1):

$$\frac{dU}{dz} + \sum_{m=2}^{4}\frac{i^{m-1}}{m!}\beta_m\frac{\partial^m U}{\partial T^m} = i\gamma\left(1 + i\tau_{shock}\frac{\partial}{\partial T}\right)$$
$$\left[(1-f_R)|U|^2 + f_R\int_{-\infty}^{\infty}h_R(T')|U(z,T-T')|^2\,dT'\right]U. \qquad 2.1.(4)$$

I utilize the well−known split−step Fourier method (SSFM) [6,12] in order to solve Eq. 2.1.(4), where the propagation step is adaptively adjusted to allow a tolerance of less than $10^{-5}$ between the steps. The number of grid points is set to $2^{13}$ with a 25−ps time window, corresponding to a 2058−THz frequency window with frequency bins of 0.5 THz. I note that the temporal window is wide enough to contain the maximum time delay of the pulses within the

fiber length and sampling is fast enough to contain the maximum frequency shift of the output signal, i.e., my grid selection satisfies the two constraints for accurately solving the GNLSE discussed in [12].

I consider four types of representative ultrashort pulses for the input radiation: soliton, Gaussian, similariton, and dissipative soliton pulses. It should be noted that in order to make fair comparisons amongst the pulse types, I assume that they have the same initial temporal width of TFWHM (i.e., 200 fs) defined by the full width at half maximum (FWHM) and are initially in transform−limited or time−BW−product−
minimized conditions, i.e., the pulses are chirp−free or chirp−minimized at T = 0 as the following:

Soliton pulses supported in AD cavities are represented by [53]

$$U(T) = U_0 \operatorname{sech}\left[2\ln\left(\sqrt{2}+1\right)\frac{T}{T_{FWHM}}\right]. \qquad 2.1.(5)$$

If an ND section is inserted in the AD cavity, Gaussian pulses can now be supported in this dispersion−mapped cavity, which are given by [54]

$$U(T) = U_0 \exp\left[-4\ln\left(\sqrt{2}\right)\left(\frac{T}{T_{FWHM}}\right)^2\right]. \qquad 2.1.(6)$$

On the other hand, if the laser cavity turns into net ND slightly, parabolic pulses, so−called similariton pulses, can be generated, which are represented by [56]

$$U(T) = U_0\left[1-\left(\frac{T}{\tau}\right)^2\right]^{1/2}\exp\left[-iC\left(\frac{T}{\tau}\right)^2\right], \qquad 2.1.(7)$$

where $\tau$ and $C$ denote the effective pulse width and the chirping

coefficient that are normally determined by the given laser cavity characteristics. In ANDi cavities, highly chirped pulses, so-called dissipative soliton pulses, can eventually be generated, which are given by [57]

$$U(T) = U_0 \sqrt{\frac{1}{\cosh\left(\frac{T}{\tau}\right)+B}} \exp\left\{-iC\ln\left[\cosh\left(\frac{T}{\tau}\right)+B\right]\right\}, \qquad 2.1.(8)$$

where it should be noted that in addition to $\tau$ and $C$ defined similarly as in Eq. 2.1.(7), there is another parameter $B$ to justify the pulse further. Without loss of generality, I assume that B is given by 0.5, which eventually leads to a pulse shape with very steep spectral edges, typically observed in ANDi cavity configurations [58], or cavities with strong ND [60]. It should also be noted that the initial similariton and dissipative soliton pulses are fully compressed to $T_{FWHM}$ = 200 fs.

Figure 2.1.1 shows the initial temporal intensity profiles and spectra of the four types of pulses described above. It is noteworthy that in Fig. 2.1.1(a) the compressed similariton (CS) and compressed dissipative soliton (CDS) pulses have slight residual side pules (RSPs) to the leading and trailing edges of the main pulse, which correspond to the contributions from the spectral components from the edges shown in Fig. 2.1.1(b). In addition, the tails of RSPs forms a background component with a power level of few tens of mW. It is worth mentioning that even though the pulses have same peak power and pulse width, the energy of each pulse is slightly different, e.g., soliton: 2.27 nJ, Gaussian: 2.13 nJ, CS: 2.25 nJ, and CDS: 3.67 nJ.

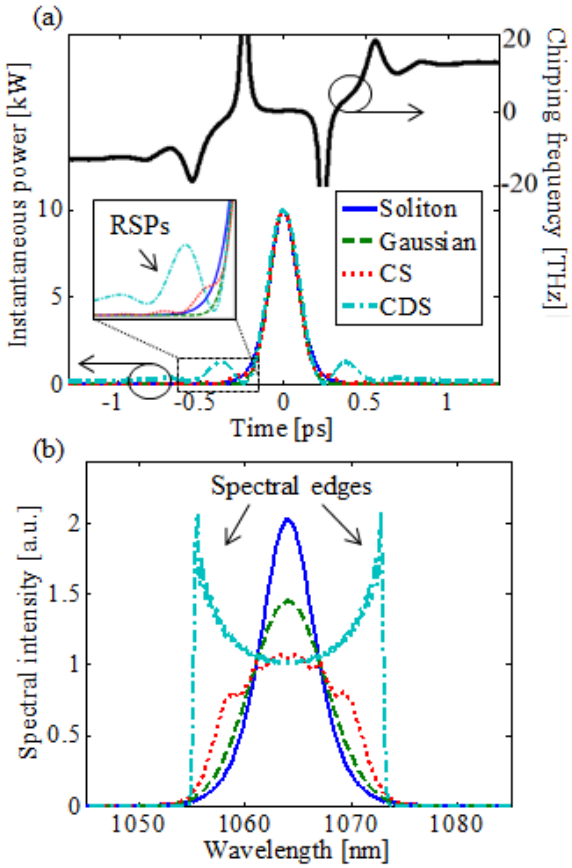


Fig. 2.1.1. (a) Temporal intensity profiles and (b) their corresponding spectra for soliton, Gaussian, CS, and CDS pulses. Top of (a) shows the chirping frequency of the CDS pulse.

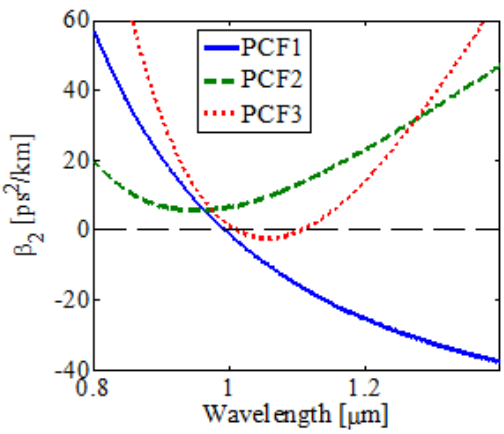


Fig. 2.1.2. GVD profiles for three different types of PCFs. The horizontal long-dashed trace represents the zero-dispersion line.

These four types of pulses are to be utilized as the input radiation to the three types of PCFs having different dispersion profiles to be described in the following: PCF1 has AD property with a decreasing slope ( $\beta_3 > 0$) near a single-valued ZDW, PCF2 has FAND property with no ZDW, and PCF3 has FAD property with double ZDWs. The ZDWs are all located near the input radiation wavelength at ~ 1064 nm. The dispersion curves of the abovementioned PCFs are plotted in Fig. 2.1.2. It is noteworthy that the parameters of PCF1 is specified based on the fiber that was investigated in Ref. [45] and those of PCF2 and PCF3 are specified based on the commercially available fibers (i.e., NL-1050-NEG-1 [65] and NL-1050-ZERO-2 [66], respectively) whilst in the case of PCF3 the detailed locations of the ZDWs are slightly adjusted from the latter. The whole fiber parameters of these PCFs are summarized in Table 2.1.1. In addition, it is noteworthy that the length of each PCF is adjusted to keep the product of $\gamma \cdot P_0 \cdot L_{\text{fiber}}$ the same for every case for the sake of fair comparison in terms of the NPS. Nevertheless, they are all within 0.3 m.

TABLE 2.1.1. PARAMETERS OF THREE PCFS USED IN THE SIMULATION.

| Quantity | PCF type | | |
|---|---|---|---|
| | PCF1 | PCF2 | PCF3 |
| $\beta_2$ [ps$^2$/m] | $-1.12\times10^{-2}$ | $1.02\times10^{-2}$ | $-2.24\times10^{-3}$ |
| $\beta_3$ [ps$^3$/m] | $-8.01\times10^{-5}$ | $-4.37\times10^{-5}$ | $-1.05\times10^{-5}$ |
| $\beta_4$ [ps$^4$/m] | $9.90\times10^{-8}$ | $2.03\times10^{-7}$ | $-7.18\times10^{-7}$ |
| ZDW [nm] | 990 | – | 1010, 1110 |

| | | | |
|---|---|---|---|
| γ [$W^{-1}km^{-1}$] | 29 | 37 | 37 |
| $L_{fiber}$ [m] | 0.2414 | 0.1892 | 0.1892 |
| N $=\sqrt{\gamma P_0 T_0^2/\lvert\beta_2\rvert}$ | 18 | 23 | 49 |

$\beta_x$: $x$−th dispersion coefficient, ZDW: zero−dispersion wavelength, $\gamma$: nonlinear coefficient, $L_{\text{fiber}}$: fiber length, $P_0$: peak power of the input radiation, $T_0$: half−width at 1/e intensity point, and N: soliton order.

In addition, I take into account quantum noise by adding to the input pulses a noise seed of one−photon−per−mode with random phase [40,43] in order to investigate the degree of spectral coherence properties of SCG in this combinatorial study. The degree of spectral coherence of the output signal is calculated with the MDOC defined as [40,43]:

$$\left|g_{12}^{(1)}(\lambda,\tau)\right| = \left|\frac{\langle E_1^*(\lambda,t)E_2(\lambda,t+\tau)\rangle}{\sqrt{\langle|E_1(\lambda,t)|^2\rangle\langle|E_2(\lambda,t+\tau)|^2\rangle}}\right|, \qquad 2.1.(9)$$

where the ensemble average is taken over 200 pairs of SC spectra, independently generated with random noise and temporal delay $\tau$ set as zero.

### 2.1.2 Simulation results

Firstly, I investigate the SCG in PCF1, i.e., a fiber with AD, which has a single ZDW with a negative slope (see the solid blue line in Fig. 2.1.2). In particular, I pay our attention to how differently the spectral broadening occurs in terms of the type of the input pulse. To consider simultaneously both temporal and spectral responses of the optical radiation in the fiber under investigation, I represent

them by means of a spectrogram as shown in Fig. 2.1.3. Previous studies have shown that soliton dynamics play a key role in the spectral broadening in this type of AD fiber in [40–46,67]. This is because input pulses with such high peak power and short duration, as in my case, can immediately evolve into higher–order solitons that can subsequently be split into fundamental solitons in the presence of perturbations such as HOD, MI, and Raman scattering effects. For PCF1 with an input pulse of $P_0$ = 10 kW and $T_{FWHM}$ = 200 fs, MI effects are dominant in the initial steps of SCG because the length scale for MI (LMI ~ 1.38 cm) is approximately 4.5 times shorter than that of soliton fission ($L_{fission}$ ~ 6.3 cm). For the four input pulses, MI triggers the break–up of the initial pulse into fundamental solitons. Meanwhile, in the time domain MI is perceived as intensity fluctuations at the central part of the input pulse. Once the initial pulse splits, the spectral broadening on the AD wavelength side is dominated by SSFS while on the ND wavelength side, the spectral broadening is dominated by FWM, i.e., phase–matched DWs emitted from the ejection of each fundamental soliton [40,44]. An interesting point to note here is that the CS and CDS pulses form broader spectra than those formed by the soliton and Gaussian pulses. One can also see from the spectrogram that the first–ejected solitons (FESs) out of the CS and CDS pulses locate at even longer wavelengths than those of the soliton and Gaussian pulses. This intriguing effect will be discussed later in this section. In addition, the spectral coherence properties of the output pulses are also shown in the upper part of each figure set in Fig. 2.1.3.

Numerical results show that the MDOC of each spectrum is partially coherent around the input pulse central wavelength, and it decays rapidly to zero as the wavelength moves to shorter and longer wavelengths. The degradation of the degree of spectral coherence can be attributed to the dominant MI effects responsible of the spectral broadening in the earlier stages of SCG. These results are in agreement with previous numerical results for input pulse durations of the order of hundreds of fs [40,43,44].

As mentioned previously, an interesting feature observed in the spectrograms shown in Fig. 2.1.3, is the broader spectral BW obtained for the CS and CDS pulses. To have a better insight of the origin of this intriguing effect, I investigate the pulse evolution of the CDS in more detail and compare it with the case of the soliton pulse. In Fig. 2.1.4(a) and (b) the temporal evolutions of the CDS and soliton pulses are shown, respectively. One can see that for the CDS case, a stronger intensity modulation is formed on top of the initial pulse in comparison to the soliton case. This strong modulation creates a complex break-up of the initial pulse, which results in an FES with also a complex transition into its fundamental solitonic state. For example, in Fig. 2.1.4(c) I see a group of sub-pulses colliding each other before forming an FES. Such interactions can induce larger non-linear phase shifts leading to shorter pulses with higher peak powers. To corroborate this feature, I tracked the peak power and pulse width of the FES from various CDS and soliton pulses with similar peak powers. In all cases, the FES peak power from the CDS pulses was higher than those measured for

soliton pulses. In this regard, the stronger self-frequency downshift observed for the CDS pulse in comparison to the soliton pulse can be related to the higher peak power and therefore broader BW of its FES. I think that this difference comes from the spectral shape of the CDS pulse [see Fig. 2.1.1(b)], which has a broader BW in addition to the spectral peaks that contain the RSPs with long tails. Thus one can expect that more spectral content is involved in the FES formation process of the CDS pulse compared to that of the soliton pulse. This allows the FES of the CDS to have broader BW, thereby leading to the higher peak power and the narrower pulse width.

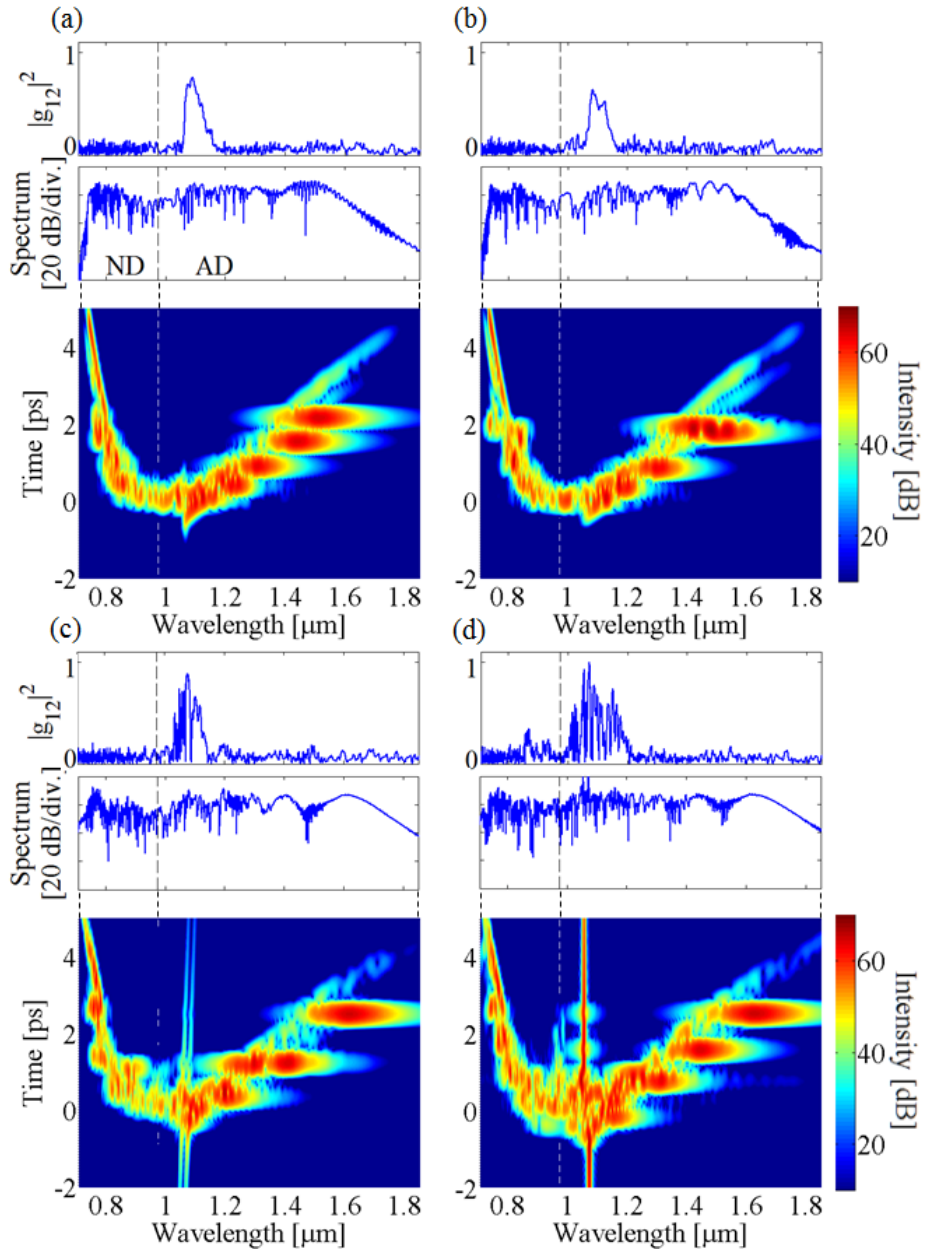


Fig. 2.1.3. Simulated spectrograms for (a) soliton, (b) Gaussian, (c) CS, and (d) CDS pulses after the propagation through PCF1.

Each spectrogram is projected onto an aggregated spectrum at the output point. The top figures show the calculated MDOC as a function of wavelength. The vertical dashed-lines denote location

of the ZDW.

It is also worth mentioning that in the CDS pulse case, the initial transition into the FES sees various DWs interacting with the RSP located at the pulse trailing edge. Such interactions also generate additional DWs [see the circular region indicated in Fig. 2.1.4(c)] that raise the spectral contents on the shorter wavelength side of the SC. For the CDS case, we also highlight the interaction of the fundamental solitons and DWs ejected from the initial pulse with the background radiation from the RSP tails. The consequence of this interaction becomes apparent in the spectrogram of Fig. 2.1.3(d) as the bright yellow circles formed at t = 1.6 and 2.5 ps along the spectral line nearby the input pulse central wavelength.

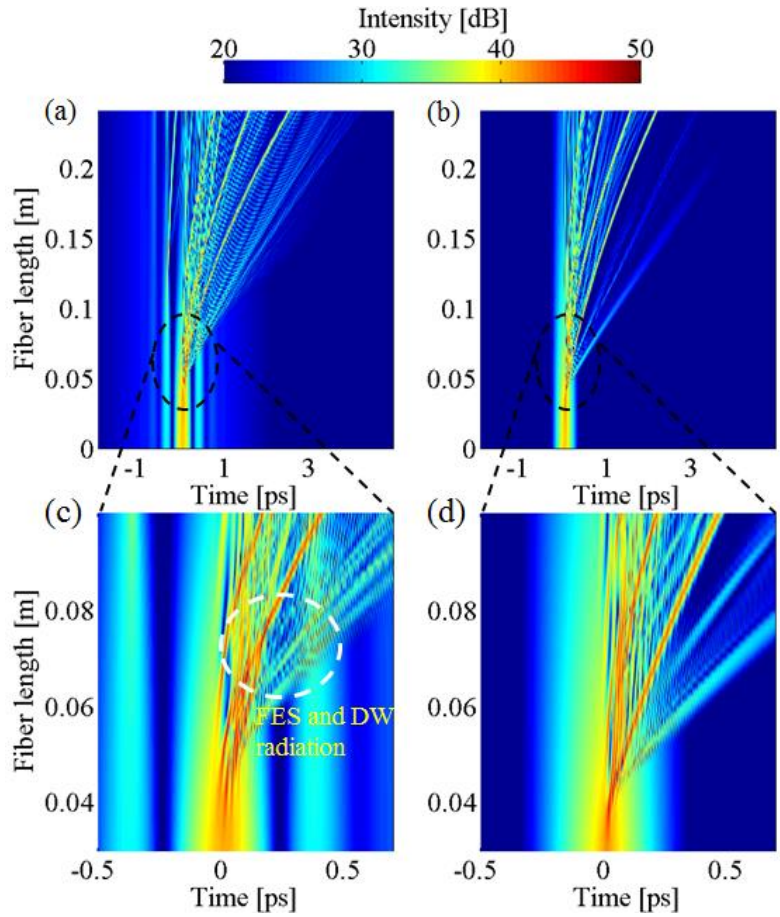


Fig. 2.1.4. Numerical simulations of the temporal evolutions for (a) CDS and (b) soliton pulses in PCF1. (c) and (d) Magnified figure of (a) and (b) at the FES ejected point.

Now I consider using PCF2, i.e., a fiber of the FAND profile with no ZDW, for SCG [see the dashed-line (green) in Fig. 2.1.2]. Fibers with this type of dispersion properties are usually fabricated by adjusting the structural parameters of PCF, such as the hole diameter and pitch length [51]. It is noteworthy that depending on a subtle change in those parameters, the dispersion near the input radiation wavelength can be either normal or anomalous [47,51], as

can be seen in Fig. 2.1.2. In fact, PCF2 is based exactly on a commercially available fiber commonly used for SCG (e.g., NL-1050-NEG-1 [65]). PCFs of this type have received a lot of research attention because they are very suitable for generating highly coherent, broad and flat spectra [49], which predominantly rely on SPM via the flattened dispersion property. Here, I analyze the detailed SCG characteristics of PCF2, applying the four different types of representative ultrashort pulses as the input radiation to it. The numerical results are shown in Fig. 2.1.5 and are discussed in the following.

In Fig. 2.1.5(a) and (b), one can see that the SC spectra generated by the soliton and Gaussian pulses exhibit very typical, spectral plateaus as demonstrated in previous reports using ANDi PCFs [49,50]. On the contrary, in Fig. 2.1.5(c) and (d), one can see that the CS and CDS pulses have led to SC with more spectral fluctuations, particularly at the central part than those of the soliton and Gaussian pulses. Such a tendency is more apparent with the CDS pulse, exhibiting that there are a number of uneven, spiky components in the spectral domain. This feature will be discussed in more detail later in this section. Regarding the degree of spectral coherence of the output radiation, one can see that the output spectrum for each different input pulse keeps a very high degree of spectral coherence over the nearly entire range. Whilst the widths of the individual MDOC distributions seem to vary slightly, each of them is broader than the 20-dB BW of its spectrum. Thus, one can consider that SC spectra formed through PCF2 are highly coherent

regardless of the type of the input pulse.

In addition, to clarify the origin of the distinctive spectral fluctuation features pointed out earlier, I further investigate the spectral and temporal evolutions of the pulses in terms of the propagation length, particularly paying my attention to the CDS and Gaussian input pulses. The results for Gaussian and CDS pulse are shown in Fig. 2.1.6(a) and (b), respectively.

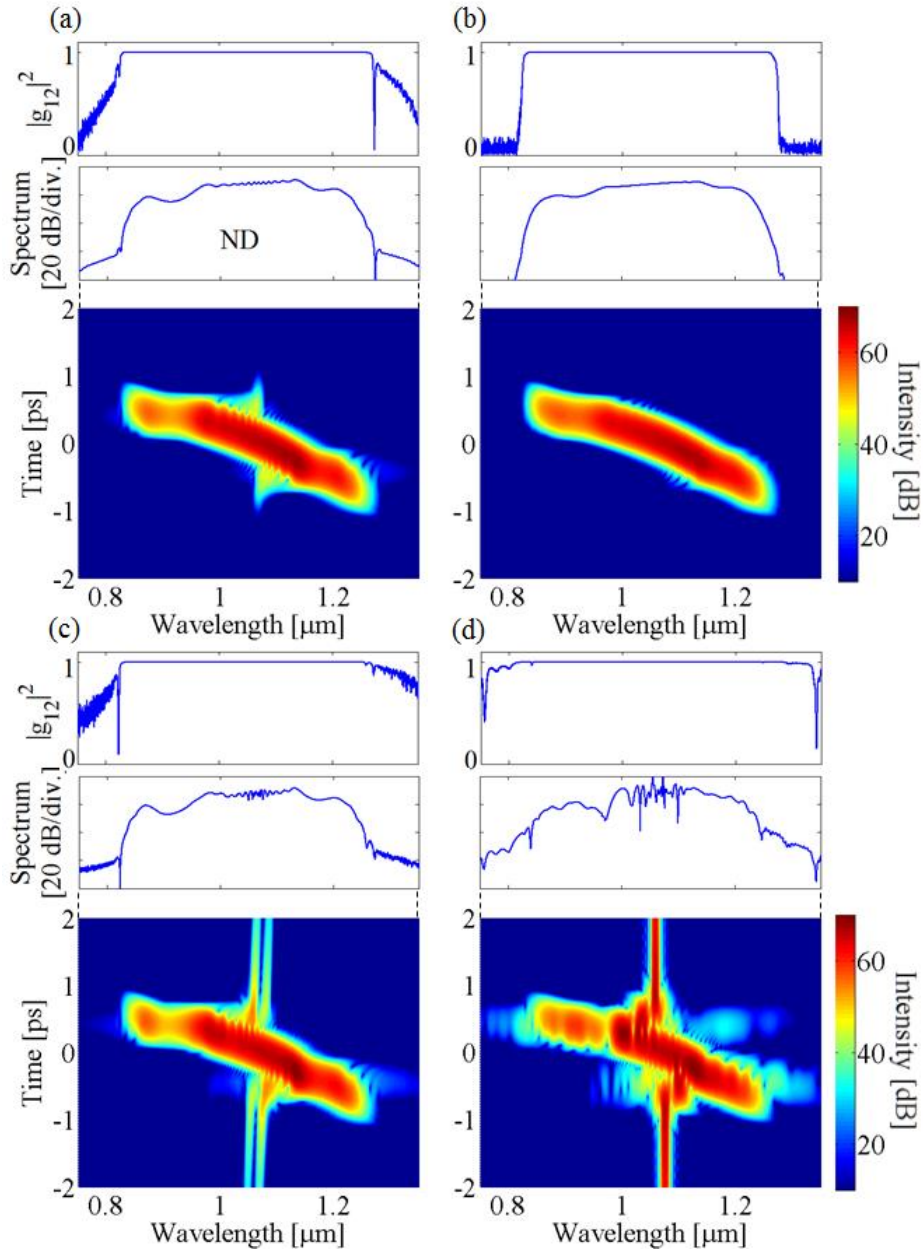


Fig. 2.1.5. Simulated spectrograms for (a) soliton, (b) Gaussian, (c) CS, and (d) CDS pulses after propagating in PCF2. Each spectrogram is projected onto an aggregated spectrum at the output point. The top figures show the calculated MDOC as a function of wavelength.

The initial spectral and temporal broadening of each pulse follows the typical behavior of pulses propagating in an ND fiber, i.e., SPM-induced spectral broadening is the predominant physical effect acting on the pulses. In particular, for the Gaussian-pulse case, one can observe that in the temporal domain a single output pulse is sustained. While there is a slight asymmetry observed in the output pulse intensity, caused by the action of normal GVD [see Fig. 2.1.6(a)], there is still no indication of optical wave-breaking (WB) at the trailing edge of the pulse [68]. The fact that the output pulses do not reach the optical WB threshold minimized the number of oscillations along the central wavelengths to those ones induced only by SPM. See for example, Fig. 2.1.5(b) and 2.1.6(c). However, in the case of the CDS pulse, the relatively smooth spectral broadening towards both shorter and longer wavelengths is clearly disrupted before a propagating distance of L = 0.1 m [see Fig. 2.1.6(d)].To understand this phenomenon, I tracked the location of the leading and trailing edges of the central pulse and their overlap with the RSPs propagating parallel to the central pulse. For a propagating distance L = 0.08 m the leading edge of the central pulse starts to overlap with its co-propagating RSPs. The overlap of these two sections of the pulses interacts by means of XPM and can induce optical WB [69]. Optical WB manifests as strong oscillations appearing at the overlap regions of the central pulse and the RSPs as seen in Fig. 2.1.6(b), which is asymmetric depending on the position of the pulse due to GVD. These strong pulse interactions at the leading and trailing edges of the central

pulse caused by XPM, in turn, introduce the strong asymmetric spectral oscillations around the central part of the pulse as seen in Fig. 5(d) and Fig. 2.1.6(d) [68]. Consequently, it is noteworthy that the CDS pulse should be considered as the last option for generating flat and smooth SC spectra if fibers with FAND profiles are selected.

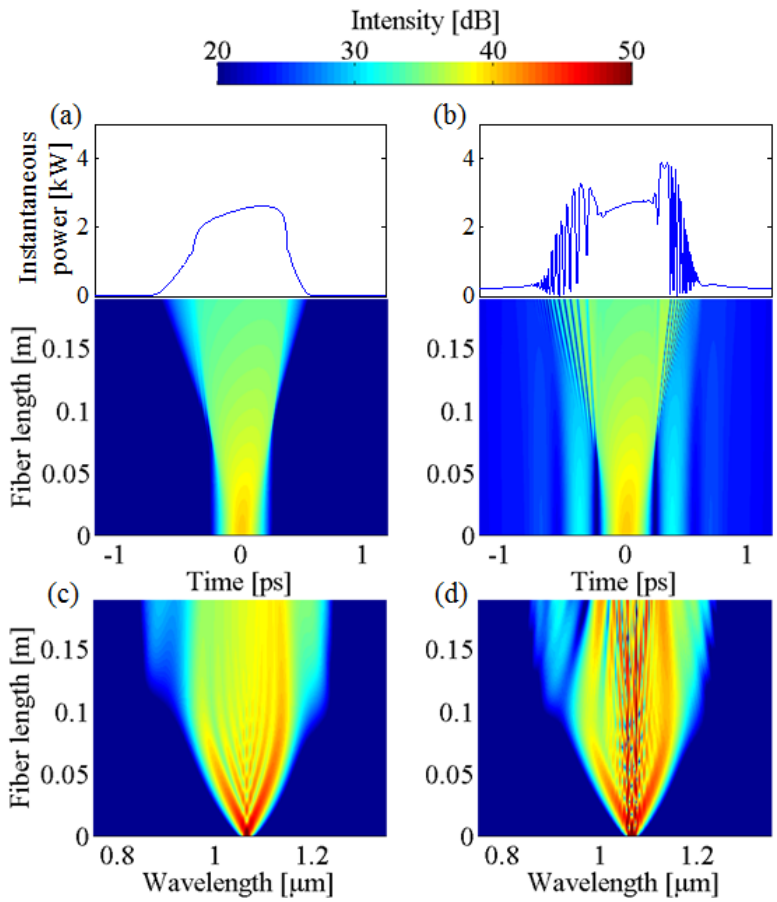


Fig. 2.1.6. Simulated temporal evolutions for (a) Gaussian and (b) CDS pulses and spectral evolutions for (c) Gaussian and (d) CDS pulses through PCF2.

Finally, I consider using PCF3 for SCG, i.e., a fiber of FAD with double ZDWs [see the dotted-line (red) in Fig. 2]. In recent years

PCFs of this type have extensively been investigated for SCG because FWM can readily occur along them, so that the use of them is relatively advantageous in terms of the suppression of the unwanted surge of MI seeded from noise [48]. They are also often used for optical parametric amplification [70]. In fact, once the FWM effect is initiated, the input radiation spectrum is primarily split into two parts across the double ZDWs, and each of them spectrally broadens via SPM while being positively chirped [47,48]. In this regard, these SCG dynamics are quite different compared to the other two previous cases. Thus, I investigate the detailed SCG characteristics of PCF3, applying in turn the four different types of representative ultrashort pulses as the input radiation to it. The numerical results are shown in Fig. 2.1.7.

Figure 2.1.7(a) and (b), one can see a very typical spectral feature of consecutive separations of the spectrum via FWM, whereas a wide spectral dip is formed near the input pulse wavelength. The dispersion profile of PCF3 presents a narrow AD spectral band ranging from 1010 nm to 1110 nm. It is very hard for such a narrow spectral band to allow for soliton formation [71]. Therefore, the spectral broadening of our signal within the AD band is predominantly supported by SPM and FWM rather than by soliton dynamics. In general, the spectral depletion becomes even more significant if the double ZDWs are located further apart [48]. In contrast, the CS and CDS pulses yield a slightly different feature. In Fig. 2.1.7(c) and (d), one can see that there are a number of spectral components that are more densely and irregularly

distributed near the input pulse wavelength range. Thus, one can expect that extra spectral contents near the center wavelength contribute to the overall SF of the output spectra. In addition, as explained briefly in the earlier part of this section, the overall spectral coherence properties are pretty high as in a similar manner with PCF2. The MDOC for each case is kept close to unity within the 20-dB BW range.

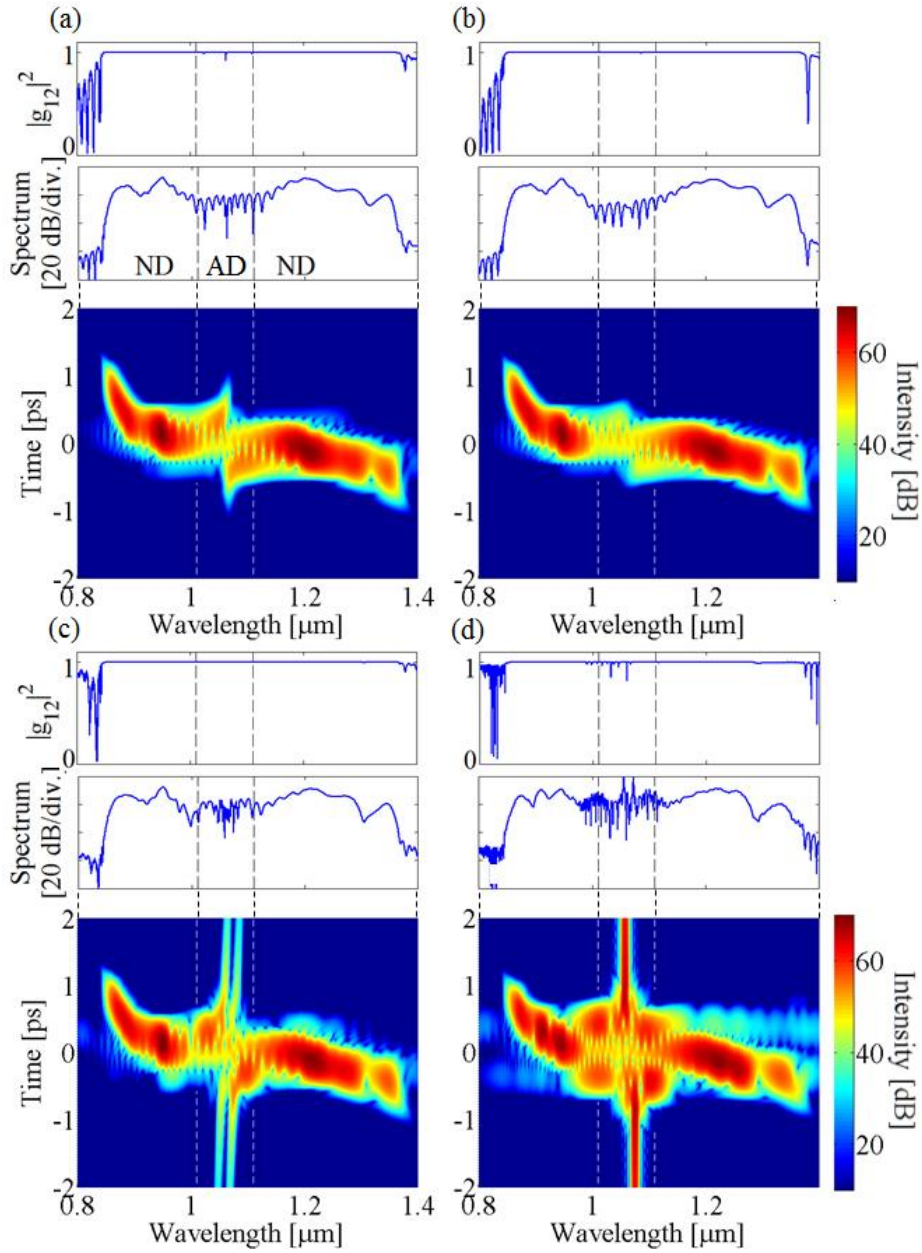


Fig. 2.1.7. Simulated spectrograms for (a) soliton, (b) Gaussian, (c) CS, and (d) CDS pulses after the propagation through PCF3. Each spectrogram is projected an aggregated spectrum at the output point. The top figures show the calculated MDOC as a function of wavelength. The dashed-lines denote the locations of the double ZDWs.

To understand the generation of the additional spectral components we should notice that the RSPs of the CS and CDS pulses also undergo spectral broadening via SPM. In particular, for the CDS pulse case spectral broadening of each of its RSPs is enhanced due to their relatively high peak power of ~ 1.2 kW. This allowed them to broaden their spectral contents all along the AD region, while propagating through the fiber length. In contrast, the RSPs of the CS pulse undergo less SPM-induced spectral broadening and their spectral contents never overlap as in the case of the CDS pulse. In particular, for the CDS pulse case its output spectrum around the AD spectral region will have contributions from the SPM-induced spectral broadening of each RSP [see Fig. 2.1.7(d)]. As a result, the wide spectral depletion, typically accompanying the soliton and Gaussian pulses, is now filled with highly structured spectral components generated from the nonlinear dynamics of the RSPs. However, for the CS pulse case, SPM-induced spectral broadening is drastically reduced, so that the spectral oscillations at the central part of the spectrum are significantly diminished. Nevertheless as I will show in the discussion section, the calculated SC-SF with the CS pulse is the highest among the other three input pulses. In this regard, the highly-structured spectrum in the AD region formed with the CDS input pulse seems to be detrimental in terms of SF. Thus now I focus on the CS pulse as the most eligible amongst the four pulse types for forming balanced SC spectra through PCF3.

In addition, to explicitly analyze the advantage of the spectral shape of the CS pulse over the cases of the Gaussian or the soliton pulses, I plot the spectral evolutions for the Gaussian and CS pulses in Fig. 2.1.8. In the case of the Gaussian pulse, the power spectral density (PSD) distribution has a wide spectral dip with a regular fringe pattern across the double ZDWs, having transferred most of the pulse energy to the side spectra centered at 900 and 1200 nm. In comparison, such effects are relatively diminished in the case of the CS pulse, having a decent level of new spectral components arising in the middle of the split spectra as well as producing a spectral BW as large as that of the Gaussian pulse. As discussed just before, these new spectral components are created from the SPM-induced spectral broadening of the RSPs of the CS pulse.

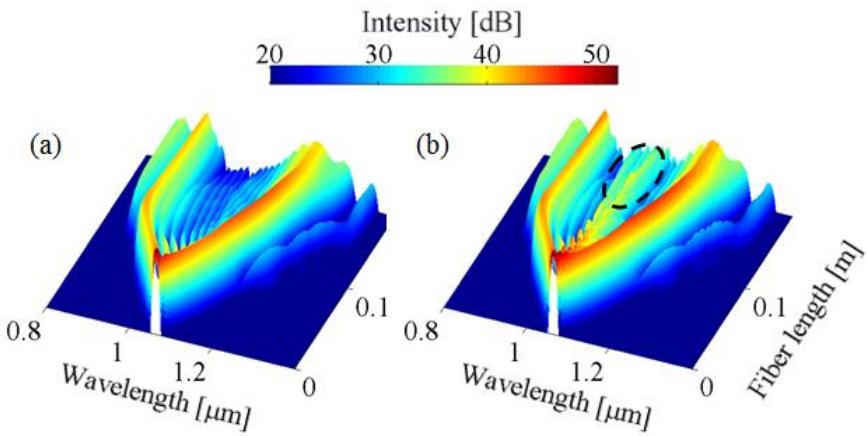


Fig. 2.1.8. Simulated spectral evolutions for (a) Gaussian and (b) CS pulses through PCF3.

### 2.1.3 Discussion

In the previous section, I have combinatorially investigated the spectral evolutions in three types of PCFs of distinct dispersion

properties, e.g., AD, FAND, and FAD, for the four types of the representative pulses of ultrafast fiber lasers, e.g., soliton, Gaussian, similariton, and dissipative soliton pulses. Building up from the achieved numerical results and putting them altogether, I here extend my discussion to drawing further quantitative and measurable outcomes in the following.

I quantify how wide the SC spectra extend by measuring the spectral BW at 20 dB (FWHM) of each of the SC spectrum outputs [18], [19]. In addition, we determine their SF by means of a SF measure (SFM) parameter [72]. The SFM is a normalized parameter to represent how uniformly the power spectrum is distributed within a defined spectral BW and is defined by [72].

$$\mathrm{SFM} = \frac{\exp\left[\frac{1}{(\omega_2-\omega_1)}\int_{\omega_1}^{\omega_2} \ln S(\omega)d\omega\right]}{\frac{1}{(\omega_2-\omega_1)}\int_{\omega_1}^{\omega_2} S(\omega)d\omega}, \qquad 2.1.(10)$$

where $S(\omega)$ is the PSD of the given optical radiation, and $\omega_1$ and $\omega_2$ denote the lower and upper boundary frequency values that determine the 20−dB BW. For example, if the SC spectrum forms a completely flat spectrum like a white noise, the SFM approaches to a unity. Otherwise, it decreases towards zero. Finally, I also discuss the degradation of spectral coherence for the different output spectra based on the MDOCs calculated in the previous sections. For convenience, the MDOC is averaged out over the wavelengths within 20−dB BW for each case. All quantified outcomes are summarized in Fig. 2.1.9.

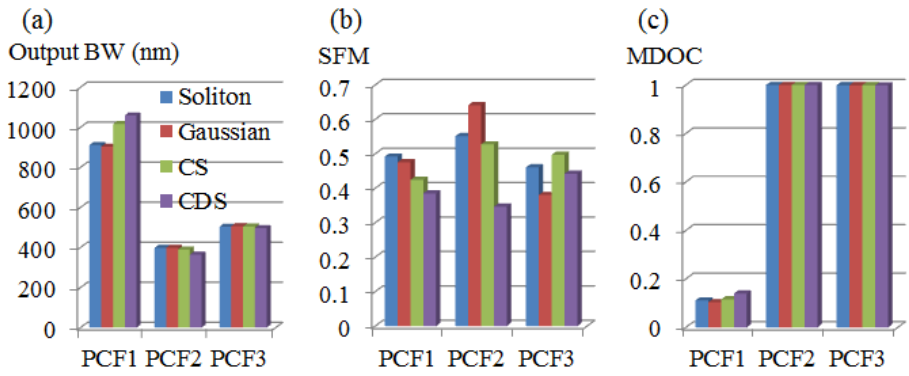


Fig. 2.1.9. Calculated (a) 20−dB BW, (b) SFM, and (c) MDOC values of the output spectra after propagating through PCF1, PCF2, and PCF3. 1st bar (blue): soliton, 2nd bar (red): Gaussian, 3rd bar (green): CS, and 4th bar (purple): CDS.

PCF1 has an AD curve with a negative dispersion slope at the input radiation wavelength. In general, the SCG with this type of fiber is primarily based on soliton dynamics, so that whatever pulse type is used as an input radiation, one can expect substantially larger spectral BWs than any other types of fiber, e.g., PCF2 and PCF3, as shown in Fig. 2.1.9(a). However, a drawback of using this type of fiber comes from the relatively low SF and degree of spectral coherence along the 20−dB BW, as shown in Fig. 2.1.9(b) and (c) respectively. Amongst the different pulse types of the input pulse, the compressed ND fiber laser pulses, e.g., the CS and CDS pulses, generate significantly broader spectra. This enhancement of the spectral broadening is mainly attributed to the initial status of the FES. In particular, I measured that the FESs of the CS and CDS cases showed higher peak power and broader BW compared to

those of soliton and Gaussian cases. Therefore, the FESs from CS and CDS pulses underwent significantly larger self-frequency downshifts. In particular, the output spectral BW obtained from the combination between PCF1 and the CDS pulse extends to ~ 1060 nm, which is ~ 150 nm broader than that of the combination between PCF1 and the soliton pulse. Consequently, for the sake of obtaining broad output spectra, a combination between PCF1-like fibers and CDS-like pulses can be the most viable option.

With fibers in the category of PCF2, one can expect relatively flat and coherent spectra broadened mainly by SPM whilst its spectral BW is relatively limited. As was discussed in Fig. 2.1.5(d) and 2.1.6(d), one can see that in the case of the CDS pulse combined with PCF2 the interactions of the leading and trailing edges of the central pulse with their corresponding RSPs result in stronger asymmetric spectral oscillations along the SC spectrum, thereby reducing its flatness. In fact, the combination of CDS pulses with PCF2 shows the lowest value of SFM for all cases as shown in Fig. 2.1.9(b). In contrast, the Gaussian pulse works very well with PCF2 in terms of SF, showing the highest value for all combinations of pulses and fibers. Regarding the spectral BW, CDS pulses show a slightly lower BW in comparison with the other pulses. Consequently, a combination between PCF2-like fibers and Gaussian-like pulses can be the most viable option if the SF is considered in the first place. Regarding the degree of spectral coherence for PCF2, one can see in Fig. 2.1.9(c) that the average MDOC within the 20-dB spectral BW reaches nearly unity,

regardless of the type of the input pulse.

Whilst PCF3 has a flattened dispersion profile similar to that of PCF2, it still holds AD properties at the input wavelength between the double ZDWs. Consequently, such fibers deliver significantly broader spectra than PCF2-like fibers as shown in Fig. 2.1.9(a). It is noteworthy that the spectral depletion across the double ZDWs is unavoidably formed in this type of fiber because of the dominance of FWM effects at the initial stage. However, the CS pulse can create a decent level of spectral components arising in the middle of the split spectra, filling the gap between the double ZDWs. This can be seen in Fig. 2.1.9(b) where the CS pulse case shows a higher SFM value. Consequently, from a relative viewpoint CS-like pulses can make a best match with PCF3-like fibers. In addition, PCF3 shows similar results as PCF2 regarding the spectral degree of coherence. The average MDOC within the 20-dB spectral BW reaches nearly unity, regardless of the type of the input pulse. Therefore, one can consider that PCF2 and PCF3 should be taken into account for high coherent SCG.

Whilst the combinatorial study presented here was carried out for a specific pulse width of $T_{FWHM}$ = 200 fs, I emphasize that the aforementioned discussions are still valid for longer input pulses. For example, by repeating the same simulation procedure with 500-fs pulses, we have verified that the pulse evolutions and the resultant performances of the SC spectra show similar trends as discussed above.

## 2.2 Active supercontinuum generation in the sub-ps regime

In recent years, the mainstream of the research on the fiber-based SCG has been focused on improving key characteristics of SC light that include BW, coherence, flatness, spectral shape, etc., by means of exploiting novel-types of fibers [52,73-76], novel-types of pump-light sources [62-64], or a variety of different combinations of them [23]. Whilst the optical fibers investigated for SCG to date have remained in passive types in most cases [23,62-64,73-76], active-type counterparts, i.e., optical fibers doped with active RE ions, have also started to attract considerable research attention as a novel fiber-based platform for SCG [15-21]. In this case, both amplification and nonlinear spectral broadening processes can occur at the same time through a single section of fiber. For example, Rui et al., investigated a SCG system based on a RE-doped large-mode-area fiber (LMAF) [16], through which they amplified low peak-power nanosecond (ns) pulses and eventually obtained power-scaled SCG via the nonlinear spectral broadening process in the active fiber itself. In fact, this system was very similar to a conventional fiber amplifier because it operated in ns optical pulses of relatively low peak powers, together with relatively low nonlinearity of the LMAF, so that the resultant spectral broadening was not so dramatic as that of a typical passive-fiber-based SCG [e.g., SCG in PCFs] that normally exploits nonlinear optical effects to an extensive level [12,40]. More recent works have verified that

the simultaneous interplay between the optical gain and nonlinear optical effects in active-type fibers could lead to more significant enhancements in spectral broadening when the SCG was realized by optical pulses with relatively short pulse widths and high peak powers [19-21]. For example, He et al. utilized 40-ps pulses for an YDF, which was still in a conventional type, and showed that the spectral overlapping between the Raman and Yb-ion gains could considerably extend the SC BW to 250 nm while amplifying the signal to 10 W [19]. My recent experimental work has also demonstrated the significance of the interplay between the optical gain and nonlinear optical effects in a highly erbium(Er)-doped soft glass fiber with high nonlinearity [20], which was seeded with 11-ps optical pulses. This work could noticeably demonstrate high gain per unit length (> 10 dB/m) as well as high spectral broadening per unit length (350 nm/m) [20].

However, to date "sub-picosecond (ps)" optical pulses that are widely utilized for passive-fiber-based SCG [23,62-64] have not been investigated extensively for active-fiber-based SCG. This presumably implies that the active-fiber-based SCG research is still in the early stage. Notwithstanding, such a real "ultrashort-pulse" regime can lead to a pivotal impact on the advance of the active-fiber-based SCG technology, because the nonlinear optical interactions in this regime can drastically increase in comparison with ns- or ps regimes, thereby leading to substantially faster and wider spectral broadening to the resultant optical signal as have already been verified in the passive-fiber-based SCG [40-49]. In

fact, if sub-ps optical pulses are exploited for active-fiber-based SCG, the total fiber length can considerably be shortened. Moreover, if the active fiber is realized in a PCF format, its dispersion and nonlinearity characteristics can also be tailored more sophisticatedly, which will further enhance or diversify the resultant SC characteristics. I here aim to carry out a rigorous numerical investigation on the active-fiber-based SCG in the sub-ps regime, and to discuss the potential improvements and prospects of the related technology. I stress that the active fiber under our consideration is a purposely designed, highly-nonlinear (HNL) and dispersion-engineered fiber, i.e., an active HNL-PCF, but that it can readily be fabricated even with the current fiber technology [22]. To construct a rigorous numerical model for analyzing the simultaneous amplification and nonlinear optical interactions of a sub-ps optical pulse in the active fiber, I take advantage of the generalized Ginzburg-Landau equation (GGLE) that includes all the nonlinear, dispersive, and complex-gain effects in the active HNL-PCF at the same time.

### 2.2.1 Numerical model

The conceptual schematic of the active-fiber-based SCG system under consideration is shown in Fig. 2.2.1. It is worth noting that the incident optical pulse is supposed to have a sub-ps pulsewidth, and to undergo amplification, dispersion, and nonlinear optical interactions through an active HNL-PCF.

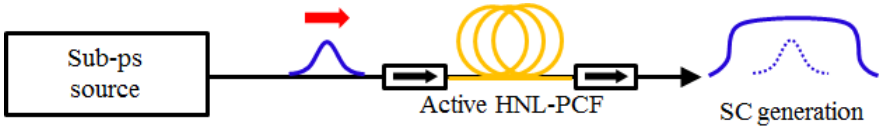


Fig. 2.2.1. Schematic of SCG based on an active HNL-PCF.

The optical pulse propagation through the active HNL-PCF section is analyzed by the GGLE as the following [77]:

$$\frac{\partial A}{\partial z} = -\frac{\alpha}{2}A - \sum_{m=2}^{\infty}\frac{i^{m-1}}{m!}\beta_m\frac{\partial^m A}{\partial T^m} + i\gamma\left(1 + i\tau_{shock}\frac{\partial}{\partial T}\right)(R * |A|^2) + G * A, \quad 2.2.(1)$$

where $A$ is the complex-valued envelope function of the optical radiation field, $z$ and $T$ are the propagation distance and the time measured in the reference frame moving at the group velocity of the optical pulse, respectively, and $*$ denotes the convolution operation. $\alpha$, $\beta_m$ and $\gamma$ denote the attenuation, m-th-order dispersion, and nonlinear coefficients, respectively. $\tau_{shock}$, the so-called shock coefficient, is characterized by the typical time scale specified at the center angular frequency ($\omega_0$) of the signal, i.e., $1/\omega_0$ [40], assuming that the effect of wavelength-dependent mode effective area is ignorable [40,42]. R(T) is the nonlinear response function and expressed as [6]

$$R(T) = (1 - f_R)\delta(T) + f_R h_R(T), \quad 2.2.(2)$$

where $f_R$ and $h_R(T)$ are the Raman fraction and the Raman response function, respectively. The latter is empirically approximated as [6]

$$h_R(T) = \frac{\tau_1^2+\tau_2^2}{\tau_1\tau_2^2}\exp\left(-\frac{T}{\tau_2}\right)\sin\left(\frac{T}{\tau_1}\right). \quad 2.2.(3)$$

For silica-based fibers, $f_R$ is typically given by 0.2, and $\tau_1$ and $\tau_2$

are given by 12.2, and 32 fs, respectively [6]. In contrast to the master equation for the conventional passive-fiber-based SCG [6,40], the last term of the right side of the Eq. 2.2.(1) is included in addition for representing the amplification process in the fiber. It is worth noting that in order to deal with the amplification process by the doped ions in the active fiber for a sub-ps optical pulse properly, the parabolic-gain approximation has been made into Eq. (1) [77], such that the gain response function $G(T)$ is inversely Fourier-transformed from the following:

$$\tilde{G}(\omega) = \frac{g_0}{2} \frac{1}{1-j(\omega-\omega_0)T_2}, \quad 2.2.(4)$$

where $g_0$ is the small signal gain coefficient at the center wavelength of the incident optical pulse that can effectively include the gain saturation effect [77]. It is also worth noting that without loss of generality, the gain spectrum of the active fiber is approximated by a Lorentzian function, the BW of which is characterized by the dipole relaxation time $T_2$ ($BW = 1/\pi T_2$) [77]. In addition, the gain saturation effect can approximately modeled by the following relation:

$$g_0 = \frac{g_{0,us}}{1+E_{pulse}/E_{sat}}, \quad 2.2.(5)$$

where $g_{0,us}$, $E_{pulse}$, and $E_{sat}$ are the unsaturated gain coefficient, the pulse energy, and the saturation energy, respectively.

The characteristics of the incident optical pulse are given as follows: It has a Gaussian-shaped envelope of 200-fs pulse-width in FWHM, and is tuned at a 1064-nm center wavelength as a typical example. The peak power of the incident optical pulse will

vary within the range of 4.7 to 47 kW, taking account of the output pulse energy levels that a typical, mode-locked fiber ring laser can offer, which are in the range of 1 to 10 nJ [57].

As for the passive characteristics of the HNL-PCF, I first need to consider its dispersion property. According to the previous research reported in Refs. [23] and [49], a normal dispersion-flattened fiber supports a coherent and flat-top SC spectrum, and is favored for achieving high power spectral density PSD or energy spectral density (ESD: energy per unit wavelength). Moreover, in this regime the pulse shape tends to be well preserved in the temporal domain even after the nonlinear broadening process. It is worth noting that these properties fit well with active-fiber-based SCG, because amplification and nonlinear spectral broadening processes are supposed to occur at the same time in this case. Thus, among the various types of HNL-PCFs that the current fiber technology offers, I choose to exploit a normal dispersion-flattened fiber type for the active-fiber-based SCG. The detailed fiber parameters are set to very typical ones, based on the specifications of a widely available commercial product [65]. In Fig. 2.2.2, I present the dispersion profiles including the sampled data from the product information and the fitted data with different contributions of the high-order dispersion coefficients. The dispersion profiles are described by the following equation

$$\beta_2(\omega) = \sum_{n=2}^{n=k} \frac{\beta_n(\omega_0)}{(n-2)!}(\omega - \omega_0)^{(n-2)}, \qquad 2.2.(6)$$

where $\omega_0$ corresponds to the central frequency of the incident

pulse. In Fig. 2, the blue-lined, green-dashed and red-dotted curves correspond to the dispersion profiles with k= 2, 4, and 6, respectively. It is noteworthy that the original dispersion profile is close to a parabolic curve so that the inclusion of the fourth order dispersion coefficient is essential. Whereas, the higher-order dispersion coefficients are not as significant as the four-order one, depicted in Fig. 2.2.2. In fact, their characteristic lengths are significantly longer than the maximum fiber length I am to consider (i.e., 3.6 m). Thus, in this numerical investigation, I consider the dispersion coefficients up to the fourth order without the significant loss of the accuracy. In addition, it is worth noting that the impacts by the dispersion coefficients of even orders (e.g., $\beta_4$) will be much larger than those by the dispersion coefficients of odd orders (e.g., $\beta_3$) in the case of a dispersion-flattened fiber, because its dispersion profile is flattened around the spectral range of the incident optical pulse, thereby approximately being parabolic as depicted in Fig. 2.2.2.

As for the active characteristics of the HNL-PCF, I assume that it is doped with Yb-ions matched for the incident optical pulse tuned at 1064 nm. In fact, the dipole relaxation time $T_2$ of the active ions determines the gain BW of the active fiber [see Eq. 2.2.(4)], which will also have an influence on the BW of the resultant SC spectrum to some extent. In this numerical investigation, the dipole relaxation time $T_2$ of Yb ions and the corresponding gain BW are specified to 16 fs and 20 THz (i.e., ~75 nm), respectively [33]. It is worth noting that this gain BW of Yb ions is significantly narrow

in comparison with the BW of typical SC radiation, which normally tends to extend to over hundreds of nm. Thus, a small variation on $T_2$ will not result in a significant change in the BW of the resultant SC radiation. In addition, I assume that the unsaturated gain coefficient $g_{0,us}$ of the doped fiber can vary from 0 to 20 dB/m, depending on how intensively it is pumped. It is worth noting that its maximum value can readily be obtained if the fiber is pumped with a high-brightness pump source [79]. The length of the HNL-PCF is purposely set to 3.6 m in order that it should be long enough to allow for at least 10-dB amplification of an incident optical pulse of 1-nJ pulse energy at the maximal pumping condition. In fact, the gain saturation effect will become apparent if the level of pumping power is relatively limited or the average power of the signal approaches the saturation power of the doped fiber [77], so that I take it into account by setting the effective saturation energy of the doped fiber to 3 nJ, which is a typical value for a doped fiber operating at a MHz-level repetition rate [80]. I stress that the 200-fs duration time of the incident optical pulse is sufficiently long in comparison with the dipole relaxation time $T_2$ of Yb-ions that is given by 16 fs. Thus, the parabolic approximation made to Eq. 2.2.(1) together with Eq. 2.2.(4) is valid. It is worth noting that if the pulse duration is comparable with the dipole relaxation time, it should be necessary to solve the whole set of Maxwell-Bloch equations [77] for the more accurate analysis. For example, in the anomalous dispersion regime, the initial pulse is splitted into multiple sub-100-fs solitons via either soliton fission or

modulation instability [12], [23]. Because the each soliton has comparable duration with the dipole relaxation time, the amplification of the solitons can not be simply described by the Eq. 2.2.(1). Thus, the whole set of the Maxwell-Bloch equations are necessary to analyze the case of the anomalous dispersion regime and in this study I limit my discussion into the only normal dispersion regime.

All the aforementioned parameters to be used for my numerical investigation are represented and summarized in Fig. 2.2.2 and Table 2.2.1. With them I solve Eq. 2.2.(1), utilizing the well-known split-step Fourier method [6]. The calculation step is determined, ensuring that the relative tolerance factor (i.e., $|A_{n+1} - A_n|/|A_{n+1}|$ ) is less than $10^{-5}$ between the two successive steps. Thus, I choose the number of grid and the temporal window size as $2^{14}$ and 50 ps, respectively, which correspond to the frequency window size of 330 THz and the frequency bin of 20 GHz, respectively. I note that according to the two computational conditions for validating the split-step Fourier method discussed in Ref. [12], the given grid resolution is appropriate enough for analyzing the nonlinear pulse evolution and its amplification in the given conditions of the active HNL-PCF under consideration.

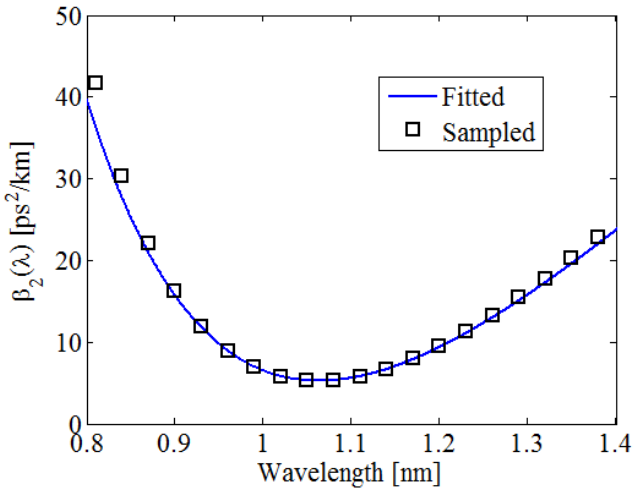


Fig. 2.2.2. Dispersion profiles from Taylor-expanded polynomials (blue-lined) and the sampled data (black-squared).

TABLE 2.2.1. PARAMETERS OF PCF AND INPUT PULSE USED IN THE SIMULATION.

| FIBER PARAMETER | VALUE | INPUT PULSE PARAMETER | VALUE |
|---|---|---|---|
| $\beta_2\,[ps^2/km]$ | 5.2494 | $T_{FWHM}\,[fs]$ | 200 |
| $\beta_3\,[ps^3/km]$ | $4.3701\times10^{-4}$ | $P_{peak}\,[kW]$ | 4.7 ~ 47 |
| $\beta_4\,[ps^4/km]$ | $2.0343\times10^{-4}$ | | |
| $\gamma\,[W^{-1}\cdot m^{-1}]$ | 37 | $E\,[nJ]$ | 1 ~ 10 |
| $g_0\,[dB/m]$ | 0 ~ 20 | | |
| $T_2\,[fs]$ | 15.92 | $\lambda\,[nm]$ | 1064 |

$\beta_m$: the m-th order dispersion coefficient, $\gamma$: nonlinear coefficient, $g_0$: small signal gain coefficient at central wavelength, $T_2$: dipole relaxation time, $T_{FWHM}$: FWHM duration, $P_{peak}$: peak power, $E$: pulse energy, and $\lambda$: central wavelength.

### 2.2.2 Simulation results

To investigate the gain-induced effects in SCG, I here carry out numerical simulations, considering two different gain conditions of $g_0 = 0$ and $g_0 = 20\,\mathrm{dB/m}$. In fact, it is worth noting that the former case implies that the HNL-PCF functions simply as a passive-type

fiber without having any gain effect. For both cases, the incident pulse energy is set to 1 nJ, which corresponds to a peak power of 4.7 kW. All the other conditions are the same as specified in Table 2.2.1. We show the evolutions of the signal spectra with respect to the fiber length for both cases in Figs. 2.2.3(a) and (b), from which we calculate the 20−dB BW and the ESD within 20−dB BW (AESD) and also show them in Figs. 2.2.3(c) and (d).

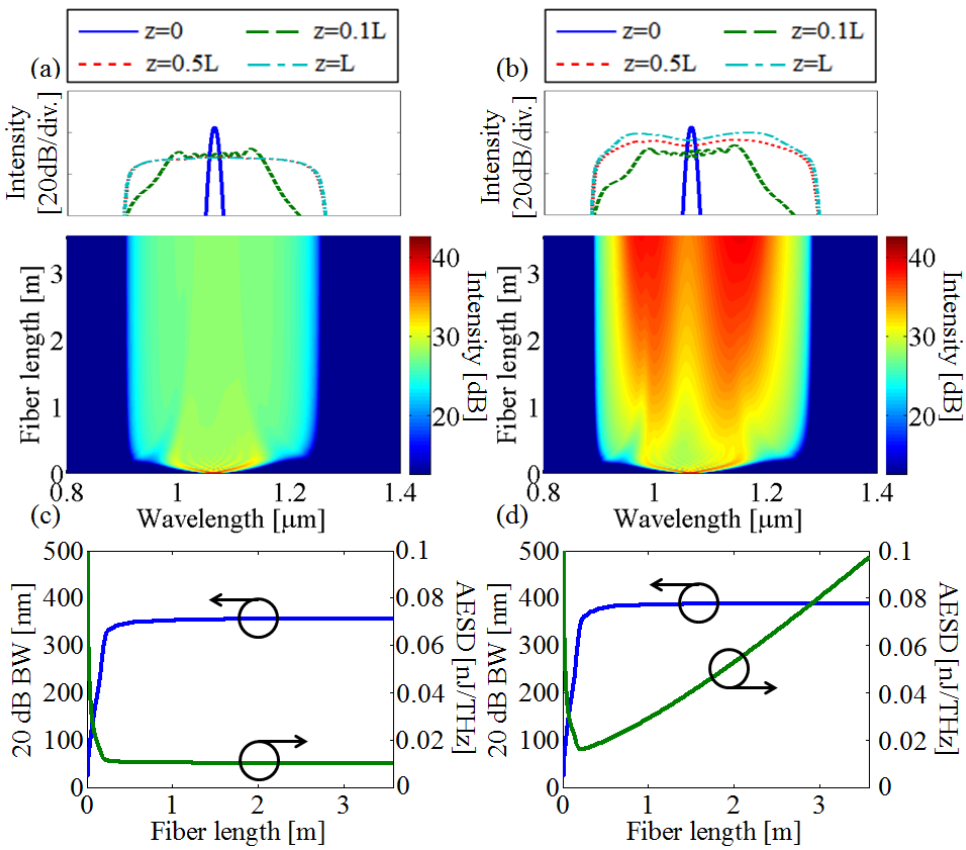


Fig. 2.2.3. Top: spectral evolution of 1 nJ input pulse through the HNL−PCF with (a) zero−gain and (b) 20−dB/m gain. Bottom: 20−dB BW (blue) and AESD (green) of the pulse along the fiber length for (c) zero−gain and (d) 20−dB/m gain.

In Fig. 2.2.3(a), one can see that even with the relatively low,

initial pulse energy of 1 nJ, the generated SC spectrum is already broadened to 360 nm of 20−dB BW thanks to the sufficiently high nonlinearity of the HNL−PCF even in the passive operating condition (see Ref. [65]). In Fig. 2.2.3(b), it is worth noting that even when the pump is turned on to the maximum rate, the spectral evolution of the signal remains similar to the former case up until $z$ = 0.2 m. This is mainly due to the fact that the amplification effect is not so feasible at the initial stage. However, once it starts to pick up the gain effect, it continuously undergoes a significant level of amplification even after having the nonlinear broadening process initiated by the SPM in the fiber. This makes a clear distinction in contrast to the case with no gain. In fact, if the HNL−PCF functions as a passive fiber with no gain, as shown in Fig. 2.2.3(c), one can see that the AESD rapidly decreases as the nonlinear spectral broadening occurs and is quickly saturated within the first meter of the fiber, which is obvious, because the total energy of the signal pulse that is fixed from the incident condition should be redistributed over the broad spectral range that the signal pulse would eventually have. In contrast, if the gain is turned on in the HNL−PCF, the spectral components at the center wavelength and its vicinity, which must be within the gain BW of the active ions, are continuously amplified, so that the power level of the spectral components of the signal within the gain BW can be maintained and even boosted up along the whole fiber length. Consequently, this effect makes the signal pulse overcome the depletion of the pulse energy at the center wavelength and its vicinity incurred by the

nonlinear spectral broadening process, as if the spectral contents within the gain BW of the fiber were supplied from "a source never running out" via the continuous amplification process. Emphatically, this novel mechanism makes it possible to keep increasing the AESD with the fiber length without unnecessarily increasing the BW of the generated SC, as can be seen in Fig. 2.2.3(d). In fact, with the fiber length of 3.6 m, the pulse energy is substantially scaled up by 10 dB to 10 nJ whereas the 20-dB spectral BW is still maintained within 400 nm. In other words, in comparison with the case with no gain, the case with gain does not lead to too much increase in the spectral BW of the overall SC, whereas the pulse energy is scaled up by 10 times. As a result, the AESD is significantly enhanced by means of the gain effect and eventually reaches 0.1 nJ/THz at the output, as shown in Fig. 2.2.3(d).

Such a distinctive feature of the SC evolution in the active HNL-PCF can also be reflected in the temporal domain as shown in Figs. 2.2.4(a) and (b), in which I plot the corresponding temporal evolutions the signal pulses in the same conditions to Figs. 2.2.3(a) and (b). We also present the evolutions of the peak powers and pulse-widths for both cases in Figs. 2.2.4(c) and (d).

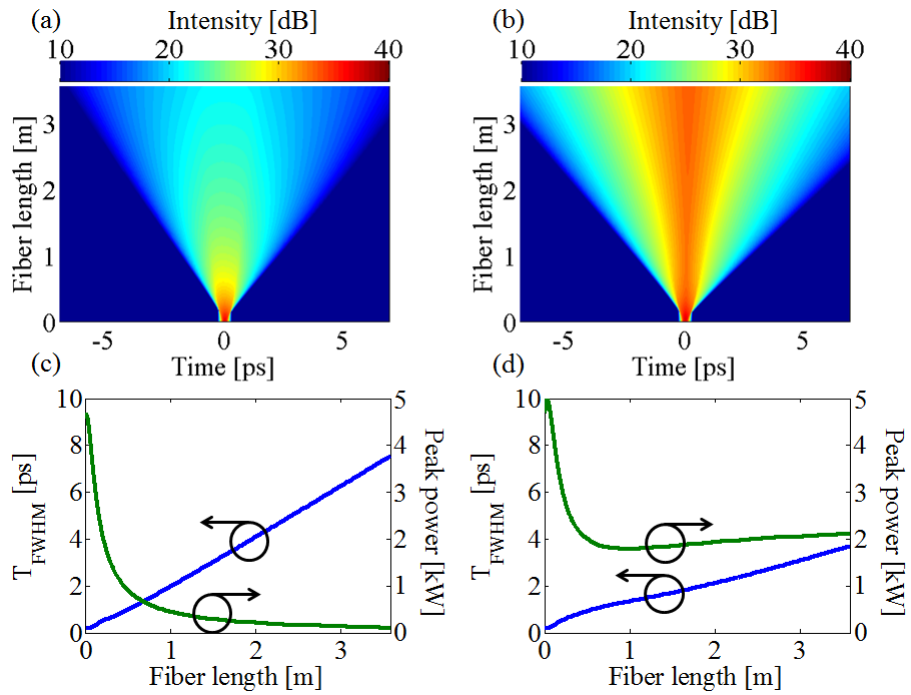


Fig. 2.2.4. Top: temporal evolution of 1 nJ input pulse through the HNL-PCF with (a) zero-gain and (b) 20-dB/m gain. Bottom: FWHM width (blue) and peak power (green) of the pulse along the fiber length for (c) zero-gain and (d) 20-dB/m gain.

In fact, one can see that the overall pulse shapes are preserved without undergoing any break-up, which is because in an all-normal condition soliton fission or MI is entirely absent. The dominant cause for the temporal broadening of the signal pulse is the dispersion effect. It is worth noting that the GVD at the central wavelength and its vicinity is not so considerable as the given fiber length is only a few meters. Thus, the GVD effect starts to appear significantly only when the signal spectrum is sufficiently broadened by SPM. This subsequently gives rise to the rapid depletion of the peak power of the signal unless it is maintained by

the amplification process in the fiber. As shown in Fig. 2.2.4(c) where there is no gain, the initial peak power of 4.7 kW decreases to 0.12 kW as the initial pulse width of 200 fs increases to 7.5 ps at the end of the fiber. Such a tendency of the peak power depletion is maintained afterwards. Thus, the nonlinear interaction length is considerably shortened by the peak power depletion if the HNL-PCF functions as a passive fiber with no gain. In contrast, as shown in in Fig. 2.2.4(d) where the gain is turned on, the peak power depletion is compensated after $z$ = 0.5 m via the amplification process by the doped ions. In fact, the peak power is gradually recovered to 2.1 kW at the end of the fiber. Thus, the nonlinear effects are retained for the nearly whole fiber length. The extended nonlinear interaction length means that the nonlinear spectral broadening at the central-wavelength contents occurs repeatedly and stacks up over the whole fiber length. Consequently, as shown in Fig. 2.2.3(b) and (d), the AESD continuously grows. Moreover, another interesting point is that the pulse evolves like a similariton [55] after $z$ = 0.5 m, in spite of its broad spectral BW of ~400 nm. It is worth noting that temporal broadening by the dispersion and the peak power increase by the amplification occur simultaneously, so that the overall pulse shape and its temporal width are relatively preserved well. In this regard, the SC pulse becomes more robust against the dispersion-induced temporal broadening and peak power depletion by means of the gain effect.

As discussed above, a novel active-type HNL-PCF can be utilized for efficient SCG with excellent output characteristics,

which include the fact that the AESD can readily be scalded up with pump and the temporal pulse shape is well preserved. On the other hand, one can also think about an alternative way to scale up the AESD while utilizing a passive-type fiber, which is to use a separate lumped amplifier to scale up the pulse energy of the incident signal before the passive-type fiber that is prepared for SCG. In this case, the amplification process and the nonlinear broadening process are completely separate in contrast to the case based on an active-type fiber. In fact, one can raise a question about how different the resultant SC spectrum would be if the SCG is realized by a lumped amplifier plus a passive-type HNL-PCF or by an active-type HNL-PCF, assuming that the total pulse energy remains the same in each case. For the fair comparison between them, we assume the following: (1) In the former, the lumped amplifier operates as an ideal amplifier, so that the peak power of the incident signal pulse to the passive-type HNL-PCF can vary from 4.7 to 47 kW without having any changes in its temporal and spectral properties, which corresponds the variation of the incident pulse energy from 1 to 10 nJ. (2) In the latter case, the optical gain by the doped ions is adjusted from 0 to 20 dB/m, while the peak power of the incident signal pulse is fixed at 4.7 kW, which implies that the energy of the signal pulse at the end of the fiber varies from 1 to 10 nJ, depending on the given gain parameter. It is worth noting that the initial pulse width is fixed at 200 fs (FWHM) for both cases, and all the other parameters for the calculations are the same as given in Table 2.2.1. The spectral evolutions of the signal

pulses in the two different schemes and their corresponding 20-dB BWs and AESDs are plotted in Fig. 2.2.5.

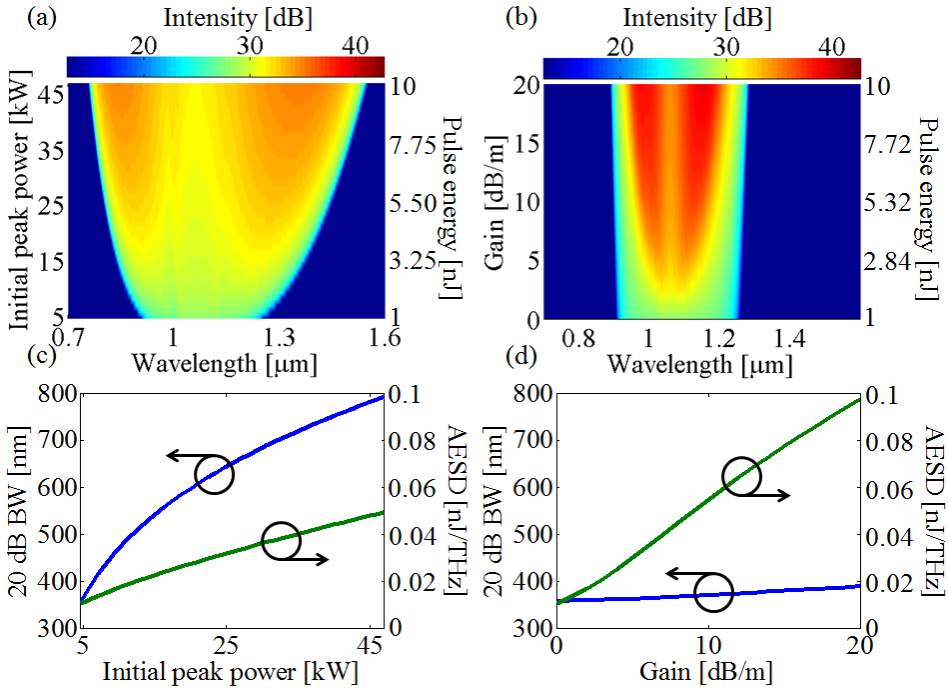


Fig. 2.2.5. Top: spectral evolution along the increase of (a) initial peak power and (b) gain. Bottom: 20-dB BW (blue) and AESD (green) of the SC spectra along the increase of (c) initial peak power and (d) gain.

In Fig. 2.2.5(a) and (b), it is worth noting that the energy of the signal pulse at the output end of the passive- or active-type HNL-PCF is presented on the right axes in accordance with the given conditions shown on the left axes, which are the initial peak power of the incident signal pulse for the passive-type HNL-PCF and the nominal gain per unit length for the active-type HNL-PCF, respectively. In fact, one can see that although the resultant output pulse energies are the same for both cases, they clearly exhibit

distinct features in terms of the BW and AESD characteristics. It is worth noting that although the passive case offers much broader emission spectra than the active case, the active case is capable of presenting substantially higher AESD than the passive case. In fact, in the active case, the BW of the output signal pulse does not noticeably change with the gain strength, so that the AESD of the active case can dramatically increase with it. Consequently, the active case eventually allows for a twice higher AESD than that the passive case, even though the total pulse energies obtained from the output ends of the fibers should be identical. Thus, from the view point of the AESD-scaling of the SC radiation, the active-fiber scheme may well be very attractive and advantageous.

In the preceding, I have shown that the peak-power depletion of the signal pulse incurred by the nonlinear spectral broadening can effectively be recovered by via the in-situ amplification in the fiber if the gain effect is turned on. Subsequently, one can expect a dramatic enhancement in the ESD (or PSD) via the combined process of the nonlinear spectral broadening and the amplification in contrast to the conventional passive-fiber-based SCG scheme. In this section, I further exploit this novel scheme, demonstrating that the active-type HNL-PCF can be used as an external platform for amplifying SC radiation. Such a case is often required when the pulse energy of the existing SC source is in short supply. For example, let me suppose that one has a SC source constructed based on a passive-fiber-based scheme, in which the resultant SC spectrum is shown in Fig. 2.2.3(a). This source already has very

broad spectral radiation, which is as broad as 360 nm in terms of 20−dB BW; however, its power or the energy per pulse may not be as high as desired. In this case, one may want to amplify the SC radiation using an external fiber amplifier. Unfortunately, no fiber amplifiers can amplify the SC radiation without losing its spectral BW, because the gain BWs of conventional fiber amplifiers are normally limited to a few tens of nm, which is much narrower than the BW of a typical SC source. In this circumstance, one can consider to exploit an active−type HNL−PCF, because it is capable of scaling up the pulse energy without noticeably modifying its BW as have been verified in Fig. 2.2.3(b).

In the following, we analyze the aforementioned features of an active−type HNL−PCF as a broadband amplifier for SC radiation in comparison with the case when a conventional Yb−doped fiber (YDF) is used instead. The pulse parameters of the input SC radiation that is supposed to be amplified via a conventional YDF or an active−type HNL−PCF are set by those of the SC radiation obtained from the output end of the passive−type HNL−PCF discussed in Fig. 2.2.2(a), which, in fact, has 1−nJ pulse energy and 360−nm 20−dB BW (240 nm in terms of 3−dB BW). It is worth noting that we assume for the conventional YDF that its nonlinear coefficient is simply reduced to a moderate value of silica−based fibers, i.e., $\gamma = 1\ \mathrm{W^{-1} \cdot km^{-1}}$, and that the dispersion properties remains the same as specified in Table 2.2.1. This is done purposely to justify the distinct features induced by the high nonlinearity of the active−type HNL−PCF. In addition, each fiber

length is determined such that it allows for 10−dB gain in terms of pulse energy, which results in 1.9 m and 3.4 m for the conventional YDF and the active−typed HNL−PCF, respectively. In addition, we estimate the SF of the amplified SC radiation along the fiber, which is quantified by the SFM parameter given by [23]

$$\mathrm{SFM} = \frac{\exp\left[\frac{1}{(\omega_2-\omega_1)}\int_{\omega_1}^{\omega_2}\ln S(\omega)d\omega\right]}{\frac{1}{(\omega_2-\omega_1)}\int_{\omega_1}^{\omega_2}S(\omega)d\omega}, \qquad 2.2.(7)$$

where S(ω) is the ESD (or PSD). In fact, the spectral range of our interest is the effective BW of the SC radiation, which is normally determined by the 20−dB BW. Thus, it is worth noting that the integration is carried out within the 20−dB BW of the resultant SC radiation. We show the evolutions of the SC radiations spectra with respect to the fiber length for both cases in Fig. 2.2.6(a) and (b), from which we calculate the 20−dB BW and the SFM within the 20−dB BW and also show them in Fig. 2.2.6(c) and (d).

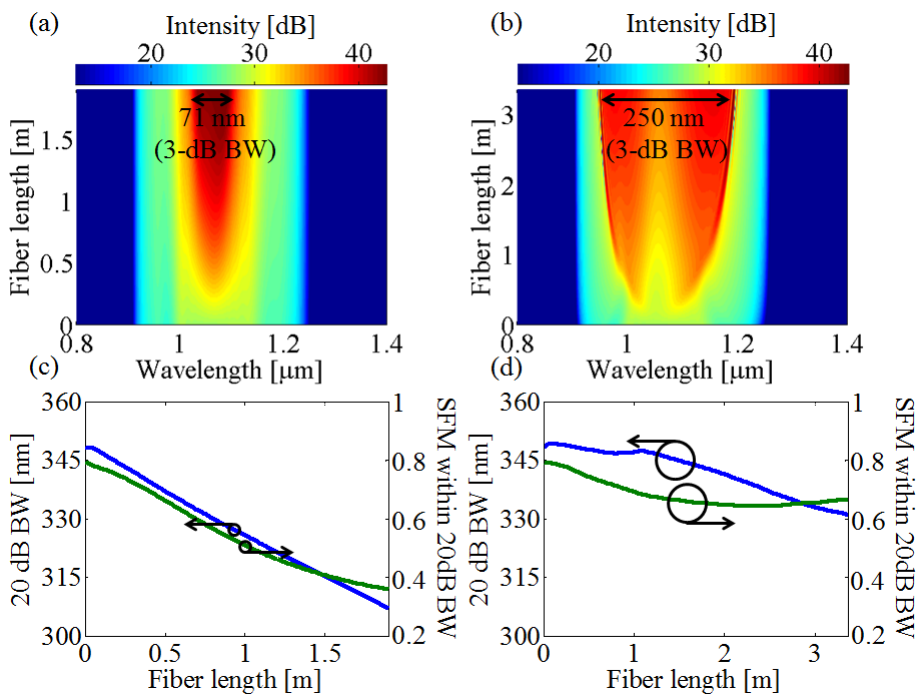

Fig. 2.2.6. Top: spectral evolution of 1−nJ SC input pulse through (a) the active PCF of 1.9 m with moderate nonlinearity and (b) the active PCF of 3.4 m with high nonlinearity. Bottom: 20−dB BW (blue) and SFM (green) of the pulse along the fiber length for (c) the active PCF of 1.9 m with moderate nonlinearity and (d) the active PCF of 3.4 m with high nonlinearity.

In the amplification process in the conventional YDF that has a moderate nonlinearity, the spectral range of the amplification is limited by the gain BW of the YDF, as can be verified in Fig. 2.2.6(a). Thus, one can see that the BW of the amplified radiation is substantially reduced to 307 nm in terms of 20−dB BW or to 71 nm in terms of 3−dB BW. Subsequently, it also gives rise to a severe degradation in the SF. It is worth noting that the initial SFM of 0.80 decreases to 0.36 after the amplification process in the conventional YDF. In this regard, one can say the characteristic features of the incident SC radiation have substantially been lost after the amplification process.

In contrast, the nonlinear amplification scheme with the active−type HNL−PCF brings in substantially distinct features, in which the nonlinearity of the fiber is set to a sufficiently high level, i.e., $\gamma$= 37 $W^{-1} \cdot km^{-1}$. In this case, the nonlinear spectral broadening readily accompanies the amplification process by the doped ions, so that the combined process make it possible to scale up the ESD nearly evenly over the whole spectral range of the incident SC radiation, as shown in Fig. 2.2.6(b). In result, the BW of the amplified

radiation remains nearly the same as that of the incident SC radiation. In fact, it becomes 330 nm in terms of 20-dB BW or to 250 nm in terms of 3-dB BW at the end of the fiber. Moreover, its SFM is relatively well maintained to 0.67, which is much superior to that of the conventional YDF, so that the amplified SC radiation still keeps the top-hat-shaped spectrum. These features make the proposed active-type HNL-PCF very attractive platform for a booster amplifier for a relatively low ESD SC radiation.

# Chapter 3

# Nonlinear dynamics in cavity configuration: Quasi-mode-locked operation

When a fiber laser cavity accompanies huge amount of nonlinearity, its stable operation generating a coherent pulse can be altered. The nonlinear effects tend to either split or distort the pulse, resulting in so-called QML operation regimes. In this study, I consider two kinds of nonlinear fiber ring cavity, having different net-cavity-dispersion (NCD). In this section, for both AD and ND cavities, I simulate the QML operation regimes and analyze the pulse stability, adjusting the cavity conditions. Then, I discuss the effects of the cavity nonlinearity on the various QML operation regimes.

## 3.1 Quasi-mode-locked operation in an anomalous dispersion cavity

Via the advances in fiber laser technology and ultrafast optics, passively mode-locked fiber lasers (PMLFLs) have been established as stable ultrafast sources for a variety of scientific and industrial applications [81-86]. From a theoretical point of view, PMLFLs can be regarded as nonlinear dissipative systems,

incorporating saturable absorption, SPM, dispersion, amplification, spectral filtering, and higher-order nonlinearities [87]. Depending on how significant the impact of each effect is, various types of ultrashort pulses can be generated, i.e. solitons, similaritons, and dissipative solitons [23]. In contrast to such PMLFLs generating a coherent single pulse per RT, if the cavity conditions become extraordinary, i.e., the cavity is highly pumped or amplitude-modulated, PMLFLs also start to operate in various QML regimes, generating multiple pulses per RT [59,60,88-103]. For example, Komarov et al. theoretically investigated the periodically-spaced stable multi-pulse operation in a fiber ring cavity [88], where they showed that the cavity could operate in a QML regime based on the nonlinear polarization rotation technique, depending on the angles of the polarization controllers. Soto-Crespo et al. reported the chaotic evolution of multiple pulses in a fiber ring cavity [90], where they showed that the cavity operation could be switched from a single-pulse regime to a randomly fluctuating multi-pulse regime, depending on the level of pump power. In particular, they also showed that with the pump power higher than a certain level, the multiple pulses turned into forming a bunched wave packet, operating in the so-called noise-like pulse (NLP) regime. In fact, NLPs have been observed experimentally in a variety of different types of PMLFLs [59,60,91-102]. In recent years, there have been a handful of reports that were aimed to resolve the complex dynamics of the NLP formation and their shot-to-shot characteristics, utilizing the dispersive Fourier transform technique

or the single-shot measurement technique [97,100,101]. I have also extensively investigated the formation of NLPs in various cavity conditions, including the degree of polarization rotation, the level of pump power, and the net dispersion of the cavity [60].

Despite the aforementioned reports, the overall dynamics and origins of the various QML regimes have yet to be clarified: First, it is unclear what cavity conditions crucially lead to the distinctions in terms of the operation regimes, whilst some previous works tried to identify them from a limited perspective of the level of pump power [60,90] or of the transmission characteristics of the SA [60,93,97,102]. This remains an issue for the so-called symbiotic regime as well, in which NLPs and solitary pulses coexist [95-99]. Second, the phase stability of multiple pulses in QML regimes has not been investigated extensively, whilst for some specific cavity conditions the degrees of phase coherence between consecutive shots in NLP [60,100,101] or multi-soliton [103] regimes were separately discussed.

To fill these insufficiencies, I here present a phenomenological numerical study on the formation of multiple pulses and the interplays of various cavity parameters for all the constitutively different QML regimes. In this study, I adjust both the saturation power of the SA element and the length of the SMF section in the laser cavity under the condition of high pump intensity and high output coupling ratio (OCR), in order to alter the type of the QML regime. This eventually leads to the changes in the amounts of NPS and net cavity dispersion (NCD) per RT. I also analyze the phase

stability of the output signal for the individual QML regimes via quantifying the MDOC of the output signal and present its contour map as a function of the cavity parameters. Relying on the MDOC contour map, I discuss the classification of the constitutively different QML regimes and their criteria.

### 3.1.1. Numerical model

The fiber ring laser cavity I consider for this study is depicted in Fig. 3.1.1, which is conceptual but general enough for investigating the evolution of multiple pulses in QML regimes. The cavity consists of an erbium-doped fiber (EDF), an SMF section, and a fast SA element. In addition, a fixed portion of the intracavity power is extracted at each RT through the output coupler (OC) located after the SA element. The unidirectional propagation of the signal in the cavity is obtained by means of inserting an optical isolator (ISO) in the cavity. The theoretical modeling of each element of the laser cavity is given as follows: The nonlinear propagation of the signal through the EDF and SMF sections are modeled by the Ginzburg-Landau equation, expressed as [77]

$$\frac{\partial A}{\partial z} = \left(\frac{g}{\omega_g^2} - j\frac{\beta_2}{2}\right)\frac{\partial^2 A}{\partial t^2} + (g + j\gamma|A|^2)A, \qquad 3.1.(1)$$

where $A$ is the field envelope, $z$ the propagation distance, $t$ the time measured in the frame moving at the same velocity with the signal, $\beta_2$ the GVD parameter, $\gamma$ the SPM coefficient, $g$ the saturated gain coefficient, and $\omega_g$ the gain BW. Depending on the signal energy inside the cavity, the saturated gain is modeled by the

following equation [77]

$$g = g_0 \frac{1}{1+E_{tot}/E_{sat}}, \quad 3.1.(2)$$

where $g_0$ is the small signal gain, $E_{tot}$ the total energy inside the cavity per RT, and $E_{sat}$ the gain saturation energy [90]. For the SMF section, $g_0$ is set to zero. In this numerical model, Eq. 3.1.(1) is solved by means of the SSFM [6]. The SA element is characterized by its intensity transfer function that is given by [90]

$$T = T_0 + \Delta T \frac{P(t)}{P_{sat}+P(t)}, \quad 3.1.(3)$$

where $P(t) = |A(t)|^2$, $T_0$ the small signal transmission level, $\Delta T$ the transmission contrast, and $P_{sat}$ the saturation power. To account for the OC, the signal amplitude is reduced based on the given OCR after the SA element. The parameters used in the simulation are summarized in Table 3.1.1, where the ranges of $P_{sat}$ and $L_{SMF}$ are also given, which are the two key parameters adjustable to determine the type of QML regime, and the other parameters are, in fact, given according to the experimental setup given in Ref. [60]. It is worth noting that the laser cavity has net AD without incorporating any ND section. Thus, the fundamental form of the pulses generated in the cavity will eventually be solitonic [23].

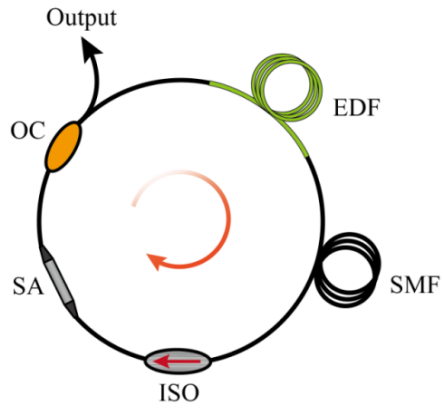


Fig. 3.1.1. Schematic of the PMLFL under consideration. EDF: erbium-doped fiber, SMF: single mode fiber, ISO: isolator, SA: saturable absorber, and OC: output coupler.

As for the initial condition of the simulation, I apply a 20-ps time-BW-limited $sech^2$-shaped pulse with 1 μW of peak power rather than applying a noise signal with random amplitude and phase. This method is to accelerate the convergence of the simulation without loss of generality [102]. After a cavity RT, the resulting signal is then used as a new initial value for the next RT calculation. The final convergence to the quasi-steady-state (QSS) solution is determined by the criterion such that the relative deviation of the total energy stored inside the cavity over a single iteration remains below 0.01, i.e., $\frac{|E_{tot_n} - E_{tot_{n-1}}|}{E_{tot_{n-1}}} < 0.01$, for at least 50 RTs. It is worth noting that whilst I repeat the iteration for 1000 RTs, the QSS solution is normally obtained well before the maximum number of the RT times.

In addition, the phase stability of the output signal is quantified by the shot-to-shot spectral coherence via the MDOC calculated in

the spectral-domain as [23]

$$\left|g_{1,2}^{(1)}(\lambda,\tau)\right| = \left|\frac{|\langle A^*(\lambda,t)A(\lambda,t+\tau)\rangle|}{\sqrt{\langle|A(\lambda,t)|^2\rangle\langle|A(\lambda,t+\tau)|^2\rangle}}\right|, \quad 3.1.(4)$$

where $\lambda$ is the wavelength of the optical radiation in the cavity, and $\tau$ is the time delay between two field quantities. For the shot-to-shot spectral stability, the time delay is given by $\tau = 1/f_{rep}$ where $f_{rep}$ is the repetition rate of output signal. In fact, this coherence measure corresponds to the fringe visibility between two consecutive pulses from the laser cavity [60,100]. The angle-brackets in Eq. 3.1.(4) represent the ensemble average over the last 500 RTs.

Table 3.1.1. Simulation parameters of the AD PMLFL.

| Component | Parameter | Value |
|---|---|---|
| EDF | $L_{EDF}$ | 15 m |
| | $\beta_{2,EDF}$ | $-12.78\times10^{-3}$ ps$^2$/m |
| | $E_{sat}$ | 1 nJ |
| | $g_0$ | 1.333dB/m |
| | $\omega_g$ | 10 THz |
| | $\gamma$ | 0.0013 W$^{-1}$·m$^{-1}$ |
| SMF | $L_{SMF}$ | 12.5 ~ 150 m |
| | $\beta_{2,SMF}$ | $-22.94\times10^{-3}$ ps$^2$/m |
| | $\gamma$ | 0.0013 W$^{-1}$·m$^{-1}$ |
| SA | $T_0$ | 0.4 |
| | $\Delta T$ | 0.6 |
| | $P_{sat}$ | 500 ~ 2000 W |
| OC | $OCR$ | 0.7 |

### 3.1.2. Simulation results & Discussion

With the given parameters specified in Table 3.1.1, I numerically characterize the dynamics of the laser cavity, initially paying attention to the formation of NLPs. It is worth noting that the given values for the gain per RT (20 dB) and the OC (70%) are substantially high, in contrast with the case supporting a stable

single-soliton regime [60]. This means that the energy built up inside the cavity becomes to undergo large amounts of accumulation and dissipation in turn repeatedly during RTs. In such a condition of extreme gain and loss, the laser cavity tends to become unstable and will eventually restart to operate in the so-called QML regimes.

As a typical example, I present in Fig. 3.1.2 the temporal and spectral behaviors of the optical signal generated from the laser cavity operating in a QML regime, where the saturation power and the length of the SMF section are given by $P_{sat}$= 1 kW and $L_{SMF}$= 100 m, respectively. One can see that the optical signal forms a packet of bunched ultrashort pulses randomly evolving in terms of amplitude and width at every RT. A distinct feature of the optical signal generated under these conditions, is that a packet of pulses remains isolated from all other parasitic pulses. In fact, the parasitic pulses tend to drift and fade away from the main packet or merge again into it after several RTs. These phenomena are highlighted with the white dashed arrows in Fig. 3.1.2(a) that shows the evolution of the optical signal in the time-domain with respect to the cavity RT time. It is worth noting that the evolution of the optical signal becomes to satisfy the condition for the QSS solution after 100 RTs. The packet of pulses consists of multiple sub-picosecond pulses with random widths and heights. A quantitative measure of the complex signal intensity is given by the RT-averaged auto-correlation (RTA-AC) trace shown in Fig. 3.1.2(d). The RTA-AC trace presents a coherent-spike on top of a broader pedestal, the time durations of which are 900 fs and 120 ps,

respectively. The former indicates the duration of the sub-pulses constituting the packet, whereas the latter corresponds to the overall packet duration. The shape of the given RTA-AC trace is a very typical form of a QML pulse, commonly observed in the experimental multi-shot AC measurements of NLP lasers [60,91-94]. The complex dynamics seen in the temporal domain subsequently gives rise to a highly structured spectrum in the spectral-domain, which also evolves stochastically at every RT as shown in Fig. 3.1.2(b). Nevertheless, the spectrum becomes to have a 20-dB BW of 14.8 nm after the first 100 RTs. I classify this operating regime into an NLP regime on account of its exact similarity with the characteristic features of the NLPs observed in many experimental reports [91-96]. On the other hand, it is worth noting that, besides the aforementioned NLP regime, different combinations of $P_{sat}$and $L_{SMF}$ can also result in other types of QML regimes, in which the multiple pulses are generated in the civility but fail to form any isolated packet. To distinguish these types of regimes from the NLP regime, I classify them into multi-soliton (MS) regimes. Since an RTA-AC trace cannot provide detailed information on the complex intensity structure of the bunched multiple pulses and its temporal evolution, I take a zoomed-in snapshot of the random temporal evolution of the multiple pulses within a few RTs as shown in Fig. 3.1.2(c). The noticeable horizontal lines crossing the figure correspond to the significant changes in the optical signal while passing through the SA and OC elements shown in Fig. 3.1.1. A close investigation of the result

shown in this figure is important in that it clearly reveals various distinct features of the temporal evolution of the multiple pulses in QML regimes. In particular, one can note that some pulses propagate without undergoing strong fluctuations but others do not if one limits the number of RTs to a small number, as depicted in Fig 3.1.2(c). For example, pulse a, located at t = 23 ps, propagates as a soliton without undergoing substantial fluctuations for at least 5 RTs, whilst pulse b splits and merges repeatedly for 4 RTs, but finally splits into two pulses owing to the interaction with pulse c between RT# 403 and RT# 404. On the contrary, pulse d is dispersed after 4 RTs and a part of the pulse energy merges into pulse e. After having a phenomenological observation on the various distinct pulse evolutions for a small number of RTs, a "question" that arises is that if a QML regime embodies a fraction of such pulses that can propagate without undergoing significant fluctuations within a few RTs, can it contribute to enhancing the degree of spectral coherence of the output signal? Thus, in the next section, I will find the answer to it, investigating the degree of spectral coherence in conjunction with the distinct behaviors of the multiple pulses generated in various QML regimes.

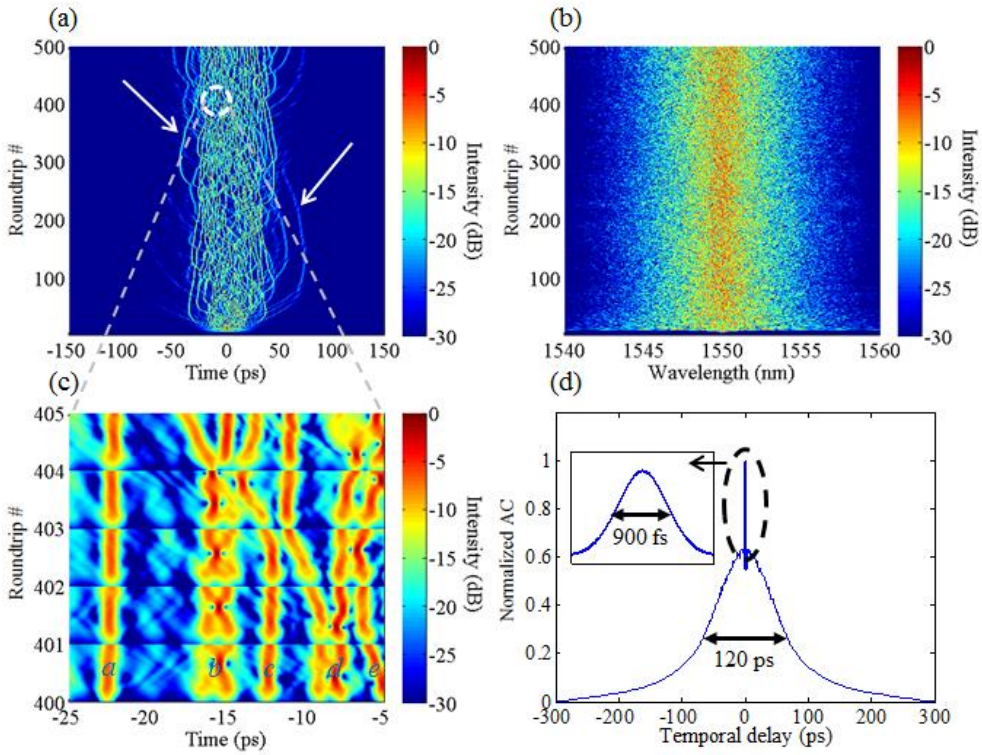


Fig. 3.1.2. (a) Temporal and (b) spectral evolutions of a time−BW−limited $sech^2$−shaped input pulse with $P_{sat}$= 1 kW and $L_{SMF}$= 100 m with respect to the number of RTs. (c) Intracavity evolution of bunched sub−pulses shown in (a) for 5 RTs. (d) RTA−AC trace of the pulses shown in (a).

Now I identify constitutively distinct QML regimes obtainable from the laser cavity specified in Fig. 3.1.1 and Table 3.1.1, while varying $P_{sat}$and $L_{SMF}$,and investigate their overall characteristics in conjunction with their wavelength−dependent MDOC characteristics. In fact, the whole simulation result that will be discussed in detail in the following indicates that one can classify them into 5 constitutive regimes: (1) the incoherent NLP regime, (2) the partially−coherent NLP regime, (3) the symbiotic regime, (4) the partially−coherent

MS regime, and (5) the coherent MS regime, which are named according to their multi-pulse dynamics and spectral coherence properties, as represented in Fig. 3.1.3, where the temporal-evolution characteristics, RTA-AC traces, spectral characteristics, and wavelength-dependent MDOCs of the generated multiple pulses are illustrated individually for the 5 constitutive regimes. It is worth noting that the RTA-ACs, spectra and MDOCs are obtained via ensemble-averaging the corresponding parameters over the last 500 RTs.

Let me start with the simulation results with relatively low saturation power combined with different lengths of the SMF section ($P_{sat}$= 700 W; $L_{SMF}$= 125 or 12.5 m), which are shown in Fig. 3.1.3(a) and (b), respectively. As can be seen in the first column of the figure, it is clear that in both cases the multiple pulses tend to form a packet of bunched ultrashort pulses and parasitic pulses isolated from the packet are not allowed to grow. The RTA-AC traces in the second column show the double-scaled structure that is one of the characteristic features of NLPs as shown in Fig. 3.1.2(d). Thus, the QML regimes for the multiple pulses illustrated in Fig. 3.1.3(a) and (b) are classified into the NLP regimes. Although these two regimes have similar temporal characteristics, there is a noticeable difference in terms of shot-to-shot stability. The insets of the first column of Fig. 3.1.3(a) and (b) show the magnified images illustrating the evolutions of the multiple pulses for 100 RTs. For the long cavity length condition (i.e., $L_{SMF}$= 125 m) shown in Fig. 3.1.3(a), the evolution of the

sub−pulses located inside the packet is significantly more chaotic and complex than those for the short cavity length condition (i.e., $L_{SMF}$= 25 m) shown in Fig. 3.1.3(b). Whilst I admit that it is not straightforward to justify the origin of the chaotic nature at this stage, I would like to explain it from the following two perspectives, focusing on the consequence by increasing $L_{SMF}$: First, the increase of the cavity length implies the increase of the NPS, which potentially tends to give rise to the collapse of solitons [92,104,105]. Thus, the long cavity length provides a harsh environment for the sub−pulses to survive as a stationary single entity. The complex sub−pulse dynamics incurred by the collapsed solitons can eventually lead to the chaotic evolution of the multiple pulses within an NLP packet, as having been verified in the previous reports [60,92]. Second, the increase of the cavity length provides more chances for sub−pulses to interact with other sub−pulses. Depending on the phase differences between the sub−pulses, they can attract or repel each other [6], and the amounts of the interactions depend on the amplitudes of the sub−pulses. Since the phases and amplitudes of the sub−pulses within an NLP packet are nearly random, the interactions with the neighboring pulses tend to result in irregular temporal shifts and amplitude fluctuations. The consequence of such dynamics has already been observed in Fig. 3.1.2(c). The increase of $L_{SMF}$ means that the longer interaction length is provided before most of the pulse energy is lost by the SA and OC elements. Thus, for each RT, the temporal locations of the sub−pulses and their strengths tend to evolve as irregularly as

shown in Fig. 3.1.3(a). I note that this cavity-length-dependent, characteristic feature is in accordance with the previous result [103].

The aforementioned two kinds of sub-pulse dynamics subsequently degrade the shot-to-shot stability of the NLPs. As a result, in the third column of Fig. 3.1.3(a), the MDOC becomes close to zero within the 20-dB BW, which means that in this QML regime, two consecutive NLPs have nearly no phase correlation, thereby leading to a considerable level of shot-to-shot fluctuations. In particular, this incoherent NLP regime is in accordance with the experimental result reported in Ref. [100]. On the other hand, if $L_{SMF}$ is significantly shortened as in the case of $L_{SMF}$ = 25 m, the NPS per RT and the interaction between sub-pulses are correspondingly reduced, resulting in producing relatively more regular multiple pulses, as shown in the first column of Fig. 3.1.3(b). In particular, from the inset, one can see that some of the sub-pulses propagate even for a few tens of RTs without undergoing a considerable level of disruption. As a result, the MDOC of the multiple pulses in this regime is noticeably boosted up, in comparison with the incoherent NLP regime. Thus, this phenomenological evidence indicates that one should not completely exclude the existence of an NLP regime having a partial-coherence feature. I think this is an important numerical confirmation that can justify the different spectral coherence properties reported in Refs. [60] and [100]. Interestingly, the calculated MDOC shows that the partial coherence mainly arises from the spectral range slightly

deviated from the center wavelength, whereas the spectral contents near the center wavelength still bear a low MDOC. I emphasize that this spectrally structured, partial-coherence characteristic of QML multiple pulses has also been analyzed experimentally [97].

Next, when I increase the saturation power of the SA element a bit more and take an intermediate length of the SMF section such that $P_{sat}$ = 1200 W and $L_{SMF}$ = 50 m, respectively, I encounter a very intriguing QML regime as shown in Fig. 3.1.3(c), which is the so-called symbiotic regime [95-99]. In this regime, the sub-pulses bunched in a packet like an NLP and the coherent pulses isolated from the packet can coexist. I note that the moderate increase in $P_{sat}$ in comparison with that for the previous NLP regimes eventually reduces the tendency of grouping of sub-pulses, so that as shown in the first column of Fig. 3.1.3(c), a few of sub-pulses can escape from the main NLP packet and form individual pulses that are temporally stable enough to coexist with the NLP packet. In contrast, if we increase $P_{sat}$ even higher such as shown in Fig. 3.1.3(d) and (e), the tendency of grouping of sub-pulses into a packet completely disappears, and thus, the sub-pulses gradually spread out in the time domain. In fact, the laser cavity becomes to operate in the MS regimes. In this sense, the symbiotic regime can be regarded as the intermediate, transitional regime between the NLP and MS regimes, such that the sub-pulses bunched in the main packet behave like NLPs whereas the isolated sub-pulses behave like coherent MSs. This consequence is also reflected in its MDOC property shown in the third column of Fig.

3.1.3(c), where one can see a considerably high partial coherence, higher than that of the partially−coherent NLP regime. We attribute this increase to the coexistence of the individual coherent pulses.

When I increase the saturation power of the SA element even higher to $P_{sat}$= 1700 W, I observe that the QML operation switches into MS regimes as already shown in Fig. 3.1.3(d) and (e), in which the lengths of the SMF section are set by $L_{SMF}$= 125 m and $L_{SMF}$= 12.5 m, respectively. It is worth noting that the main distinct feature of the MS regimes from the NLP regimes is the fact that sub−pulses tend to keep spreading out in the time domain without forming any stationary packet of bunched sup−pulses. In fact, one can justify that the extinction of a stationary packet of sub−pulses in the laser cavity is owing to the substantial increase in $P_{sat}$, because as for the lengths of the SMF section there are no significant differences between the MS regimes and the NLP regimes. Since the sub−pulses are not tightly packed in the cavity, the interactions between them become less significant for the MS regimes than for the NLP or symbiotic regimes, thereby leading to the significant increase in the MDOC as shown in the third column of Fig. 3.1.3(d) and (e). In addition to the reduction of the sub−pulse interactions, the substantial increase in $P_{sat}$ can drastically alter the amount of the NPS that all the sub−pulses undergo in the cavity per RT. I note that the increase of $P_{sat}$ means the increase of the cavity loss, thereby resulting in the decreases of the peak power levels of the individual sub−pulses. Thus, the NPSs that all the sub−pulses in the MS regimes undergo per RT tend to decrease

significantly, so that the soliton-collapse effect cannot be apparent [104], as verified in Fig. 3.1.3(d) and (e). Thus the lower NPS per RT via the alleviation of the soliton collapse effect can be another reason for the increase of the MDOCs in the MS regimes. Actually, I think the amount of the NPS per RT is closely correlated with the shot-to-shot stability of multiple pulses. This issue will be discussed in more detail soon.

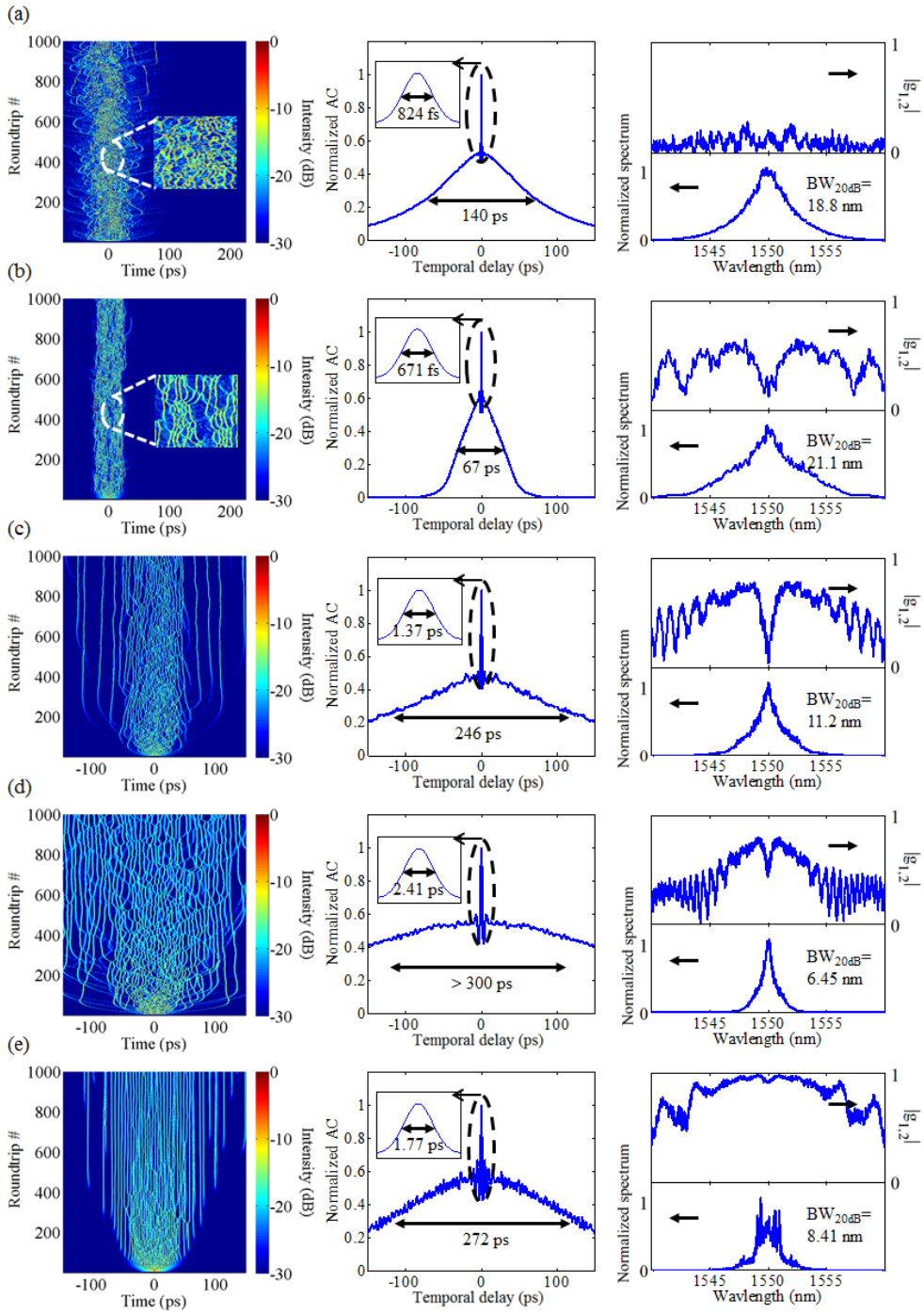


Fig. 3.1.3. Temporal evolution (left), AC trace (middle), spectrum (right; lower), and MDOC (right; upper) in (a) the incoherent NLP regime with $P_{sat}$ = 700 W and $L_{SMF}$ = 125 m, (b) the partially-coherent NLP regime with $P_{sat}$ = 700 W and $L_{SMF}$ = 12.5 m, (c) the

symbiotic regime with $P_{sat}$ = 1200 W and $L_{SMF}$ = 50 m, (d) the partially−coherent MS regime with $P_{sat}$ = 1700 W and $L_{SMF}$ = 125 m, and (e) the coherent MS regime with $P_{sat}$ = 1700 W and $L_{SMF}$ = 12.5 m.

In addition, the difference between the partially−coherent MS regime and the coherent MS regime is similar to the relationship between the incoherent NLP regime and the partially−coherent NLP regime. For the long SMF section (i.e., $L_{SMF}$ = 125 m), as shown in Fig. 3.1.3(d), the evolution of the sub−pulses becomes relatively more irregular and chaotic, thereby resulting in the partially−coherent MS regime. In contrast, for the short SMF section (i.e., $L_{SMF}$ = 12.5 m), the interactions between the sub−pulses are substantially diminished, forming stable and coherent multiple pulses, as shown in Fig. 3.1.3(e).

As discussed above, I have verified that the two cavity parameters of $P_{sat}$ and $L_{SMF}$ play a pivotal role in determining the type of the QML regime and also the shot−to−shot stability of the corresponding multiple pulses. In order to visualize their characteristic relations, I present a contour map in Fig. 3.1.4(a), plotting the averaged MDOC with respect to $P_{sat}$ and $L_{SMF}$ and also indicating the whereabouts of the 5 constitutive QML regimes on it. It is worth noting that the averaged MDOC is quantified via the following equation:

$$\left|g^{(1)}\right|_{ave} = \frac{\int_{-\infty}^{\infty}|g^{(1)}(\omega)|S(\omega)d\omega}{\int_{-\infty}^{\infty}S(\omega)d\omega}, \qquad 3.1.(5)$$

where $S(\omega)$ is the normalized PSD.

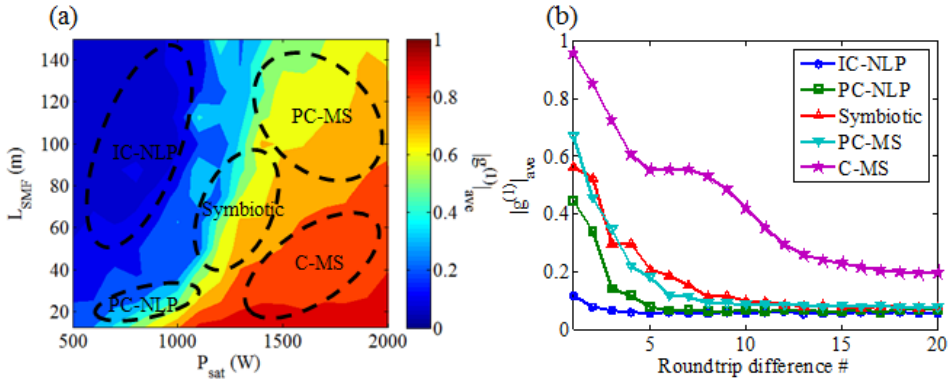


Fig. 3.1.4. (a) Contour map of the averaged MDOC for 1 RT difference as a function of $P_{sat}$ and $L_{SMF}$ in conjunction with the specified locations of the 5 constitutive QML regimes. (b) Averaged MDOC as a function of the RT difference number between pulses for the 5 constitutive QML regimes. IC: incoherent; PC: partially-coherent; and C: coherent.

In fact, I justify five different regions for the five different constitutive QML regimes that include the incoherent NLP, partially-coherent NLP, symbiotic, partially-coherent MS, and coherent MS regimes on the contour map, considering the characteristic features of the multiple pulses obtainable at the given location of $P_{sat}$ and $L_{SMF}$, whilst I cannot distinctly classify every location into a specific regime, because the transitional and intermediate status of the multiple pulses soon becomes apparent in the border areas across the different regimes. Nevertheless, I can still say that the incoherent NLP regime, in which the averaged MDOC is below 0.2, is obtained with $P_{sat}$ < 1000 W and $L_{SMF}$ > 50 m. While either decreasing $L_{SMF}$ or increasing $P_{sat}$ from the

incoherent NLP regime, I can expect the improvement of the shot-to-shot stability into the three partially-coherent regimes that include the partially-coherent NLP, symbiotic, and partially-coherent MS regimes. The partially-coherent NLP regime is obtained by decreasing the $L_{SMF}$ below 25 m, in which the averaged MDOC varies from 0.3 to 0.5. The symbiotic regime is obtained with the conditions of 1100 W < $P_{sat}$ < 1500 W and 40 m < $L_{SMF}$ < 90 m, in which the averaged MDOC varies from 0.3 to 0.7, depending on the portion of the isolated coherent pulses in comparison with the NLP packet having significant shot-to-shot fluctuations. The partially-coherent MS regime is obtained with the conditions of $P_{sat}$ > 1500 W and $L_{SMF}$ > 80 m, in which the averaged MDOC varies from 0.5 to 0.8. By increasing $P_{sat}$ higher than 1500 W and decreasing $L_{SMF}$ shorter than 60 m, the QML regime finally turns into the coherent MS regime. As having been shown in Fig. 3.1.3(e), the shot-to-shot stabilities of the multiple pulses are well maintained, thereby resulting in the averaged MDOC higher than 0.8 in this regime.

In addition, I illustrate the averaged MDOC with respect to the RT difference number between the shots in Fig. 3.1.4(b). It is worth noting that $\tau$ in Eq. 3.1.(4) can be given by $n/f_{rep}$ with an integer $n$, and that all the previous results shown in Fig. 3.1.3 and Fig. 3.1.4(a) were obtained with $n$= 1, which means the MDOC was evaluated between the two consecutive pulses. In contrast, I pay my attention to how the averaged MDOC evolves if $n$ increases, i.e., the RT difference number increases. In the incoherent NLP regime,

the averaged MDOC for $n$= 1 is about 0.12, and decreases further down below 0.1 for $n$ = 2. In contrast, in the three partially-coherent regimes that include the partially-coherent NLP, symbiotic, and partially-coherent MS regimes, the partial coherence natures are maintained to a considerable level until $n$ become 5 to 10, although they decrease to the similar level as the incoherent NLP regime afterwards. In this regard, the coherence length of the multiple pulses is around the cavity length for the incoherent NLP regime and about 5 to10 times of the cavity length for the three partially-coherent regimes. In further contrast, the decreasing rate of the averaged MDOC in the coherent MS regime is much slower than the others. I have verified that the averaged MDOC eventually decreases to below 0.1 when $n$ = 194, which means the coherence length of the multiple pulses operating in the coherent MS regime is exceptionally long relative to the other regimes.

As shown in Fig. 3.1.3 and 3.1.4, the shot-to-shot coherence of the QML multiple pulses is critically affected by the cavity conditions that are parameterized by $P_{sat}$ and $L_{SMF}$. I believe that the coherence property is closely linked with the amount of the NPS that the QML multiple pulses undergo per RT, because the multi-pulse dynamics is presumably determined by the soliton collapse effect and the sub-pulse interactions inside a packet if any. Thus, I rework the contour plot of the shot-to-shot coherence shown in Fig. 3.1.4(a) in terms of the amount of the NPS per RT and illustrate it in Fig. 3.1.5(a), which is quantified by the following

equation:

$$\varphi_{NL} = \int_0^{L_{cav}} \left[ \int_0^{T_{RT}} \gamma |A(t,z)|^4 dt / \int_0^{T_{RT}} |A(t,z)|^2 dt \right] dz, \qquad 3.1.(6)$$

where $L_{cav}$ and $T_{RT}$ denote the length of the laser cavity and the unit RT time, respectively. In fact, this value is the time-averaged B-integral of the whole QML multiple pulses per RT in the given cavity condition. It is worth noting that the field envelope $A$ is obtained when the laser cavity has entered a QSS condition or the RT reaches 1000.

In fact, I emphasize that the reworked contour plot shown in Fig. 3.1.5(a) is greatly analogous to the one shown in Fig. 3.1.4(a). In other words, the averaged MDOC is directly related with the amount of the NPS per RT. Then, I can reinterpret the mechanism of how the type of the QML regime is eventually determined in terms of the NPS per RT as the following: The NPS per RT below 0.2π assures the coherent MS regime, resulting in a high degree of shot-to-shot coherence. I note that the contour lines for $\varphi_{NL}$= 0.2$\pi$ and $\varphi_{NL}$= 0.4π are nearly perfectly matched with those for $\left|g^{(1)}\right|_{ave}$=0.9 and $\left|g^{(1)}\right|_{ave}$=0.8, respectively. The $\varphi_{NL}$ ranging from 0.4π to 2π corresponds to the averaged MDOC ranging from 0.3 to 0.8. We note that in this range the three partially-coherent regimes are obtained. For $\varphi_{NL}$ > 2π, the QML regime turns into the incoherent NLP regime, in which the averaged MDOC becomes lower than 0.2. In particular, in the case of the incoherent NLP regime shown in Fig. 3.1.3(a), the NPS per RT has reached 6.5π, thereby leading to exhibiting a very typical chaotic feature of NLPs. In fact, the close

correlation between the averaged MDOC and the NPS per RT is well verified in Fig. 3.1.5(b). Actually, the data points can be fitted by

$$\left|g^{(1)}\right|_{ave} = \frac{1}{\left(\frac{\varphi_{NL}}{\alpha}\right)^2 + 1}\ , \qquad 3.1.(7)$$

where $\alpha$ is a fitting parameter that is approximately given by $\sim 1.15\pi$ in the given condition. It is worth noting that if I calculate the correlation coefficient [106] between the MDOC and the NPS per RT, its magnitude becomes as large as 0.8305, which gives that the correlation between those two quantities is statistically meaningful. I intuitively interpret this Lorentzian relationship between the MDOC and the NPS per RT such that the former is homogenously broadened with the latter [107]. From this perspective, I can also deduce that the effective strength of the NPS per RT that destroys the shot-to-shot coherence is characteristically quantified by $\alpha$. Interestingly, I note that the estimated value for $\alpha$ is quite close $\pi$, which means that the QML multiple pulses tend to undergo consecutive, destructive interference effects with the background noise signals particularly when they become to lose the shot-to-shot coherence.

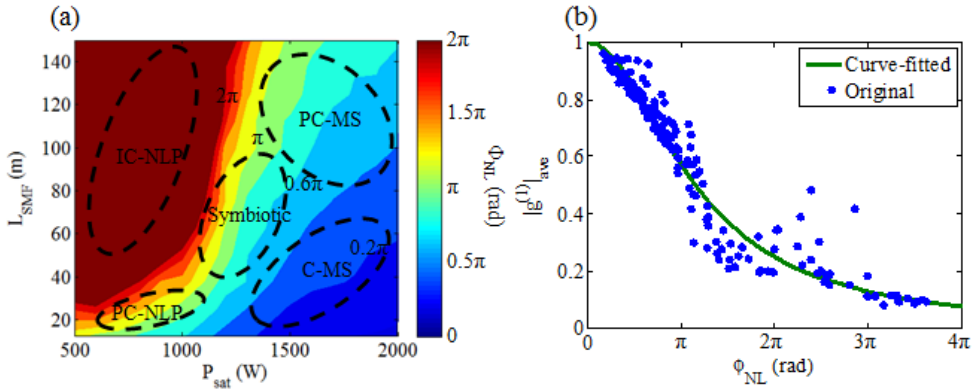

Fig. 3.1.5. (a) Contour map of the NPS per RT as a function of $P_{sat}$ and $L_{SMF}$ in conjunction with the specified locations of the 5 constitutive QML regimes. (b) Averaged MDOC as a function of the NPS per RT. The blue dots and the green curve represent the original data set and the fitted curve with a Lorentzian distribution function, respectively. IC: incoherent; PC: partially−coherent; and C: coherent.

In addition to the NLP per RT, I here consider another critical parameter that determines the type of the QML regime in the given condition, which is the NCD. Since the NCD is simply given by the following relation, NCD= $\beta_{2,\mathrm{EDF}}L_{\mathrm{EDF}}+\beta_{2,\mathrm{SMF}}L_{\mathrm{SMF}}$, the y−axis of Fig. 3.1.5(a) can be reinterpreted into the amount of the NCD, because the first term of the relation is fixed in our case. Then, one can say that the incoherent NLP and coherent MS regimes are mainly determined by the amount of the NPS per RT. In contrast, in the cases of the other three partially−coherent regimes, i.e., the partially−coherent NLP, symbiotic, and partially−coherent MS regimes, the amount of the NCD plays a critical role in precisely determining the type of the QML regime in addition to the amount of the NPS per RT. In other words, the 5 constitutive QML regimes are now determined by the two general cavity parameters of the NPS per RT and the NCD, instead of $P_{sat}$ and $L_{SMF}$. In a quantitative manner, the cavity operation can be classified into three cases in terms of the amount of the NCD: (1) If the NCD is over $-1$ ps$^2$, the QML regime turns into either the partially−coherent NLP regime or

the coherent MS regime. (2) If the NCD is below $-2$ ps$^2$, the QML regime turns into either the incoherent NLP regime or the partially-coherent MS regime. (3) If the NCD is between $-1$ ps$^2$ and $-2$ ps$^2$, various QML regimes, including the symbiotic regime, can appear, depending on the detailed conditions of the NPS per RT and the NCD. On this foundation, we would like to add two more points on the alternation of the QML regime: First, the symbiotic regime that is located approximately at the center of the contour map has very intermediate characteristic features that can also be quantified in the middle of both the NPS per RT and the NCD, so that it can evolve into any of the other four regimes, depending on the amounts of nonlinearity and dispersion. In this regard, the symbiotic regime can be thought as a 4-way saddle point. Second, the MS regimes can somehow turn into the NLP regimes by increasing the NPS per RT regardless of the amount of the NCD. In other words, the formation of an NLP packet is critically related with the amount of the nonlinearity in the given cavity regardless of the amount of the NCD as having been verified experimentally in Refs. [60,90,97].

## 3.2 Quasi-mode-locked operation in a normal dispersion cavity

In this section, I study the QML dynamics in the fiber ring cavity in which the NCD is normal. Up to date, various QML regimes have been investigated in ND fiber ring cavities, including the NLP regime [97,102], multiple dissipative solitons [102] and so on. For

example, S. Smirov et al. verified three key regimes in a ND cavity: stable dissipative soliton regime, NLP regime and an intermediate regime between two former regimes [97]. Recently, Z. Cheng et al. reported more advanced results indicating that the intermediate state between the dissipative soliton regimes and the NLP regime include the dissipative soliton resonance effect [102]. They also verified that there exist a critical point of the SA power changing the cavity operation regime from the dissipative soliton resonance regime to the NLP regime. In addition my group revealed that the NLP regime is also directly obtained from the stable dissipative soliton regime via increasing only pump power [60].

Despite the aforementioned research, there still exists unexplored research area in the QML dynamics in the ND fiber ring cavity. For example, the existence of the symbiotic regime that has been recently observed in the AD cavities has not yet been verified in the ND case. Furthermore, shot-to-shot phase stability of the QML pulses has not been investigated in the ND cavities. Thus, to fill these insufficiencies, I here present a phenomenological numerical study on the formation of QML pulses and the interplays of various cavity parameters for all the constitutively different QML regimes. As similar as the analysis in the section 3.1, I investigate the QML dynamics while adjusting the saturation power of the SA element and the length of the passive fiber section, eventually leading to the changes in the amounts of NPS and NCD per RT. I verify the distinctive QML operation regimes and also analyze the phase stability of the output signal for the individual QML regimes

via quantifying the MDOC of the output signal. Relying on the MDOC contour map, I discuss the classification of the constitutively different QML regimes and their criteria.

### 3.2.1. Numerical model

As similar as the AD case introduced in the section 3.1.1, I here consider the ND fiber ring cavity depicted in Fig. 3.2.1, which is conceptual but general enough for investigating the QML operation regimes. The cavity consists of an EDF, dispersion compensation fiber that induces strong ND, SFT and OC. Comparing with the schematic in Fig. 3.1.1, I note that the SMF section was replaced with the DCF for the normal NCD. In addition, SFT was applied to help mode-locking of the fiber ring cavity by means of compensating the pulse broadening. The pulse propagation through each component is modelled in the same manner as explained in the section 3.1.2. In addition, the transmittance of the SFT is approximated by Lorentzian profile in the frequency domain. The simulation parameters are presented in Table 3.2.1. I note that, except for the DCF parameters, the saturation energy of the EDF and the SFT-BW, all of the cavity parameters are same as the AD case. The characteristics of the employed DCF are given by Ref. [60]. The saturation energy of the EDF and the BW of the SFT were empirically chosen to support QML regimes.

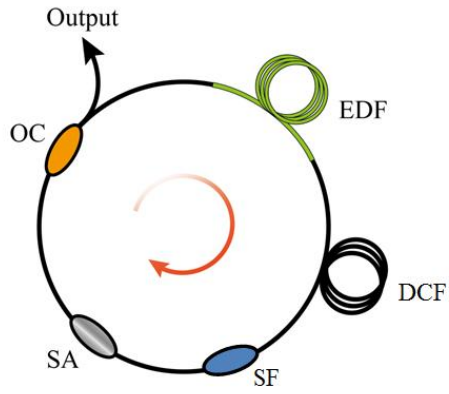


Fig. 3.2.1. Schematic of the PMLFL under consideration. EDF: erbium−doped fiber, DCF: dispersion−compensating fiber, SFT: spectral filter, SA: saturable absorber, and OC: output coupler.

Table 3.2.1. Simulation parameters of the ND PMLFL.

| Component | Parameter | Value |
|---|---|---|
| EDF | $L_{EDF}$ | 15 m |
| | $\beta_{2,EDF}$ | $-12.78\times10^{-3}$ ps$^2$/m |
| | $E_{sat}$ | 10 nJ |
| | $g_0$ | 1.333dB/m |
| | $\omega_g$ | 10 THz |
| | $\gamma$ | 0.0013 W$^{-1}$·m$^{-1}$ |
| DCF | $L_{DCF}$ | 4 ~ 10 m |
| | $\beta_{2,\,DCF}$ | $136\times10^{-3}$ ps$^2$/m |
| | $\gamma$ | 0.0013 W$^{-1}$·m$^{-1}$ |
| SA | $T_0$ | 0.4 |
| | $\Delta T$ | 0.6 |
| | $P_{sat}$ | 500 ~ 2000 W |
| OC | $OCR$ | 0.7 |
| SFT | $BW$ | 45 nm |

### 3.2.2. Simulation results & Discussion

With the given parameters specified in Table 3.1.1, I numerically simulate the QML dynamics in the ND cavity, initially focusing on the formation of the NLP. It is noteworthy that the saturation energy of the EDF is 10 times higher than the chosen value in the

AD cavity, which means that much higher intra-cavity energy is involved for the QML operation in the ND case. As a typical example of the QML operation of the ND cavity, I present the temporal and spectral features of the NLP regime in Fig. 3.2.2, where the saturation power of the SA and the length of the DCF were chosen by 700 W and 9 m, respectively.

In Fig. 3.2.2(a), after 400 RTs, the NLP packet maintains its width, whereas the amplitude within the packet irregularly evolves. In addition, in the regime, isolation of any signal from the packet is not allowed. Similarly, in Fig. 3.2.2(b), the spectral evolution of the signal also shows that the spectrum has significant shot-to-shot fluctuation within its 20-dB BW (14.2 nm). Thus, as we already discussed in the section 3.1.2, the signal can be regarded as the NLP. In Fig. 3.2.2(d), the AC trace also shows a typical structure of the NLPs having narrow spike on the broad shoulder. Fig. 3.2.2(c) shows the intracavity dynamics of the NLP for 5 RTs. Interestingly, contrasting to the case of the AD cavity, the signal contents are not apparent to be a pulse and seem to be noise. Thus, if there exist shot-to-shot coherence in the NLP regime, the origin of the coherence can not be found in the coherent subpulse inside the packet.

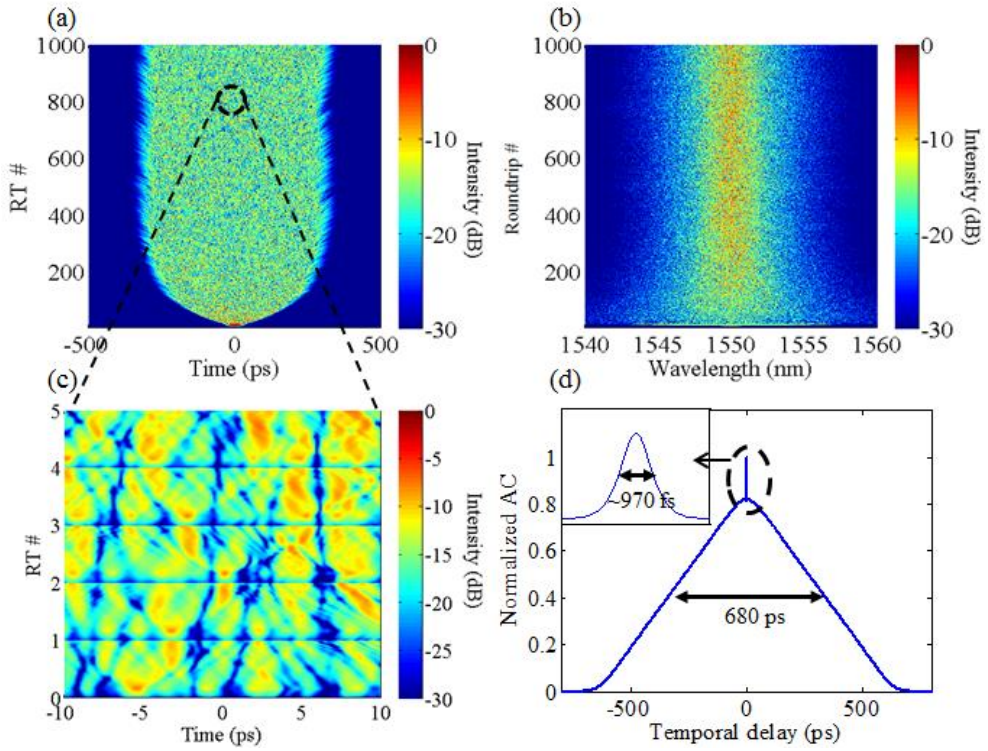


Fig. 3.2.2. (a) Temporal and (b) spectral evolutions of a time−BW−limited $sech^2$−shaped input pulse with $P_{sat}$= 700 W and $L_{DCF}$= 9 m with respect to the number of RTs. (c) Intracavity evolution of bunched sub−pulses shown in (a) for 5 RTs. (d) RTA−AC trace of the pulses shown in (a).

Focusing on the difference of NLP structure between the AD and the ND cavities, I present the temporal evolution of the NLPs in the AD and ND regimes in Fig. 3.2.2 (a) and (b), respectively. It is noteworthy that the substructure inside the NLP is different between two NCD cases. In the AD case, the appearance of the sub−ps solitons inside the NLP packet is clearly shown. Whereas, in the ND case, such sub−pulse structure is not apparent. From the substructure inside the NLP packet, I can hypothesize the different

process of the NLP formation in two NCD cases. With the anomalous NCD, the extraordinary cavity conditions cause multiple solitons inside the cavity and the multiple solitons form a group in a certain cavity conditions, resulting in a NLP. Whereas, with the normal NCD, sub-ps solitons are not supported and a relatively long dissipative soliton in either ps or ns regime is generated. Then, by increasing the internal cavity energy, the dissipative soliton is collapsed, accompanying noisy structure on the pulse. Although the amplitude of the ND-NLP seems to be noisy, the envelope under the noisy component maintains its pulse characteristics. This fact can be found in Fig. 3.2.2(d), showing that the ratio of the spike over the AC-shoulder is quite small, compared with the AD case in Fig. 3.1.2(d). In this regard, the NLP in the ND cavities can be thought as a broken version of a dissipative soliton.

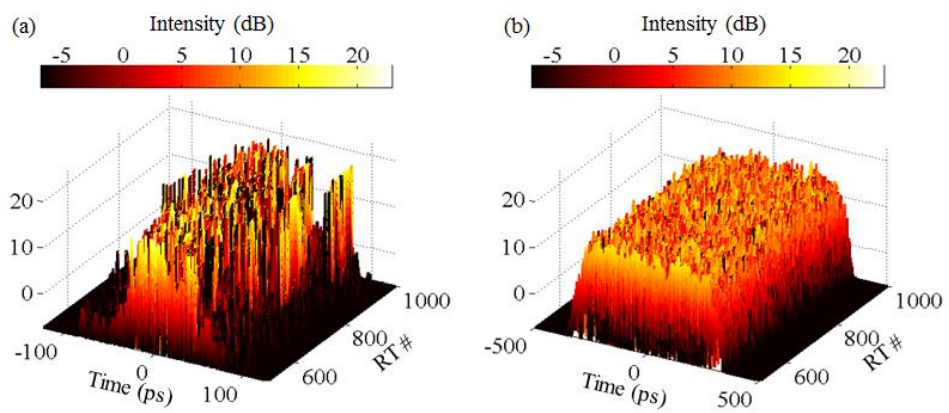


Fig. 3.2.3. Temporal evolutions of (a) AD-NLPs with $P_{sat}$= 700 W and $L_{SMF}$= 125 m and (b) ND-NLPs with $P_{sat}$= 700 W and $L_{DCF}$= 9 m.

Now, I identify constitutively different QML regimes from the

ND cavity specified in Fig. 3.2.1 and Table 3.2.1, adjusting the two chosen cavity parameters: $P_{sat}$ and $L_{DCF}$. As a result, the cavity operation regimes can be categorized into three distinctive QML regimes: (1) NLP regime, (2) transient regime, and (3) symbiotic regime. The alternation of the QML regimes depending on the cavity conditions are presented in Fig. 3.2.4 and the temporal evolutions in three QML regimes are presented in Fig. 3.2.5.

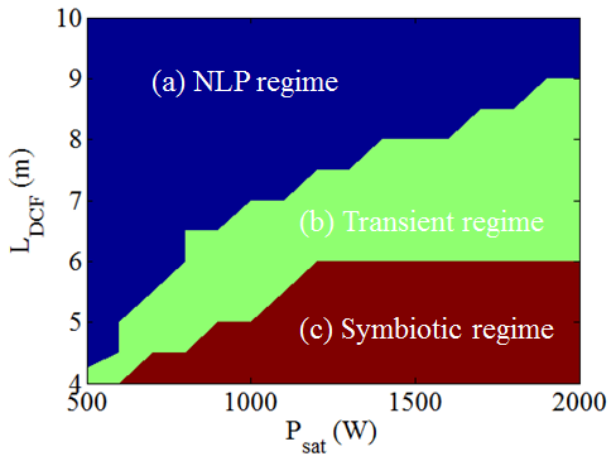


Fig. 3.2.4. Contour map of operation regimes as a function of $P_{sat}$ and $L_{DCF}$.

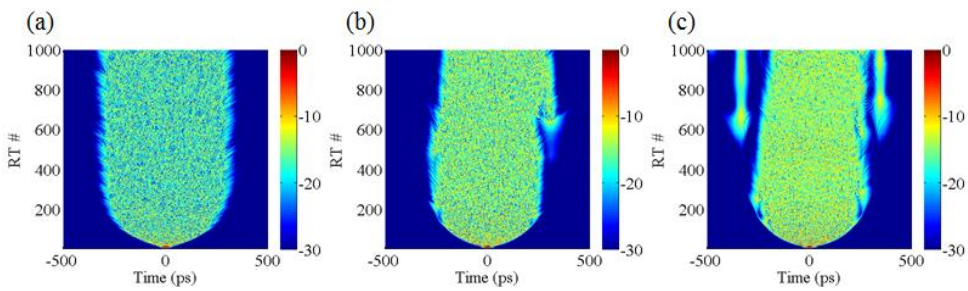


Fig. 3.2.5. Temporal evolution in (a) the NLP regime with $P_{sat}$ = 700 W and $L_{DCF}$ = 8 m, (b) the transient regime with $P_{sat}$ = 1100 W and $L_{DCF}$ = 6 m, and (c) the symbiotic regime with $P_{sat}$ = 2000 W and $L_{DCF}$ = 5.5 m.

According to the overall simulation results, the NLP regime is supported by relatively low saturation power and long DCF length, which is in accordance with the IC-NLP regime in the case of the AD cavity. In other words, for the higher NCN and NCD, the cavity operates in the NLP regime without any isolated pulse. Whereas, with the lower DCF length and the higher saturation power, a part of the signal escape from the NLP packet and the isolated pulses copropagate with the NLP packet. Thus, the results show that as similar as the case of the AD cavity, there exists a symbiotic regime in the ND cavity. In Fig. 3.2.5(c), the isolated pulses maintain their stable and coherent characteristics. However, according to our simulation results, the isolated pulses can also evolve into the NLP packet, resulting in the multiple NLP evolution. In this thesis, such multiple NLP regimes are not considered because the simulation of those regimes requires more extended simulation conditions such as the wider temporal window. Between the NLP and the symbiotic regimes, there exists a transient regime. In the regime, a part of the signal tries to escape from the packet, as shown in Fig. 3.2.5(b). From those results, the isolation from the NLP packet is determined by the amounts of the NCD and the NCN.

For the simulated QML dynamics for two cavity parameters, I characterize the phase stability of the QML pulse by means of the calculation of the averaged MDOC quantified by the Eq. 3.1.(5). In addition, to explore the relation between the phase stability and the NCN, I calculate the NPS per RT quantified by the Eq. 3.1.(6). The

contour map of the MDOC and the NPS per RT are presented in Fig. 3.2.6.

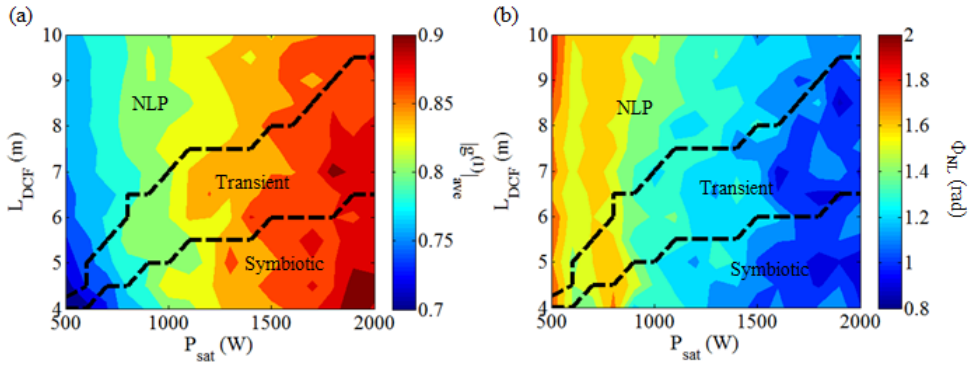


Fig. 3.2.6. Contour map of (a) the averaged MDOC and (b) the NPS per RT as a function of $P_{sat}$ and $L_{DCF}$.

From the contour maps in Fig. 3.2.6(a) and (b), first I note that the relation between the MDOC and the NPS per RT discussed in the section 3.1.2 is still valid for the ND cavity. The contour plot of the NPS per RT is analogous to the one of the MDOC. In other words, the large amount of the nonlinearity degrades the phase stability of the QML pulse, as similar as the case of the AD cavity. Whereas, the amount of the MDOC degradation is not as significant as that in the AD cavity. I hypothesize that it is related with the substructure of the NLP. As discussed above, the NLP in the ND case does not have clear internal sub-pulses and maintains the relatively stable envelope under the noisy components. Thus, the stable envelope originates the partial coherence between the neighboring pulses. In addition, the amount of the NPS per RT is also relatively small compared with the AD case. It means that the peak power of the NLP is the smaller than the solitons in the AD cavity. It is because

the increase of the pulse energy leads to the temporal broadening of the pulse rather than the increase of the peak power, in accordance with the dissipative soliton resonance effect [102].

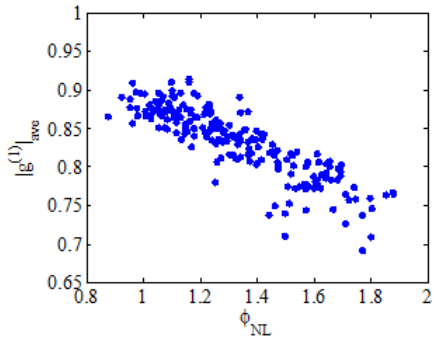


Fig. 3.2.7. Averaged MDOC as a function of the NPS per RT.

To quantify the relation between the MDOC and the NPS per RT, I plot the MDOC as a function of the NPS per RT, presented in Fig. 3.2.7. We emphasize that although the range of the NPS per RT is not as broad as the case in the AD cavity, it is clear that the MDOC is consistently decrease with the increase of the NPS per RT. According to the calculation, the correlation coefficient reaches 0.86, meaning that the relation between two quantities is statistically significant.

From Fig. 3.2.6, I emphasize another noticeable point that the alternation of the operation regimes is not correlated with the either MDOC or NPS per RT. Taking account of the fact that the pulse characteristics inside a ND cavity is critically affected by the NCD in addition to the NCN, I hypothesize that the operation regime is altered by both the NCD and the NCN. To verify this, I calculate the total phase shift (TPS) per RT defined by the following equation:

$$\varphi_{tot} = \int_0^{L_{cav}} \beta_2 \omega(z) dz, \qquad 3.2.(1)$$

where $\omega(z)$ is the length-dependent 3dB-BW of the QML pulse. It is noteworthy that the amount of the NCN determines the spectral BW, thus the calculated TPS includes both the linear and nonlinear phase shift. As analogous to Fig. 3.2.6, I present the calculated TPS per RT depending on the cavity parameters in Fig. 3.2.8.

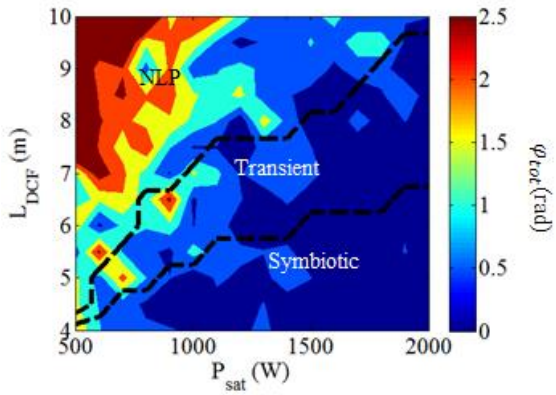


Fig. 3.2.8. Contour map of (a) the TPS per RT as a function of $P_{sat}$ and $L_{DCF}$.

From Fig. 3.2.8, the alternation of the cavity operation regimes is clearly related with the amount of the TPS per RT. In particular, the TPS per RT higher than unity leads the cavity to support only the NLP regime without any isolated pulse and the TPS per RT lower than 0.5 makes the cavity operate in the symbiotic regime. Thus, as different with the case of the AD cavity discussed in section 3.1, the ND cavity operation regime depends on the TPS per RT including both the NCD and NCN.

In Fig. 3.2.6, the MDOC is not correlated with the alternation of the operation regimes. In other words, the isolated pulses make

insignificant contribution on the shot-to-shot coherence. In fact, the shot-to-shot coherence is dominantly determined by the noise fluctuation on a relatively stable pulse envelope. It is in contrast with the case the AD cavity, in which the subpulse dynamics diversified the MDOC and QML regimes together. Whereas, in the ND cavity, the amount of the noise fluctuating for every RT is the main factor to determine the shot-to-shot coherence. To verify this issue, I plot the MDOC values for the saturation power of the SA and the length of the DCF, separately, presented in Fig. 3.2.9.

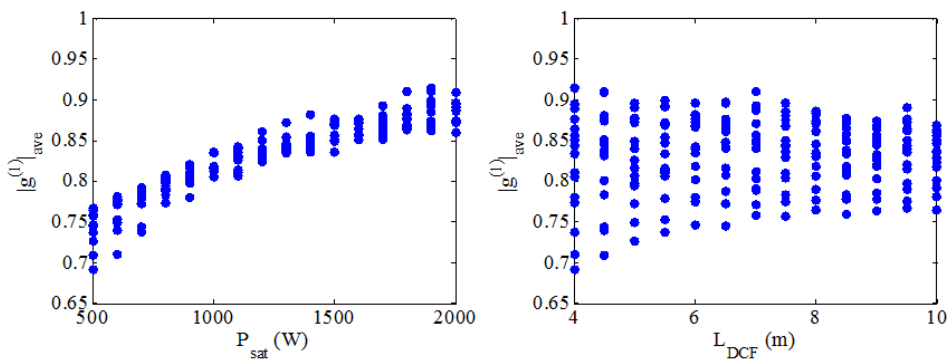


Fig. 3.2.9. Averaged MDOC as a function of (a) the saturation power of the SA and (b) the length of the DCF.

In Fig. 3.2.9(a), the MDOC is proportionally increase with the saturation power of the SA, where the correlation coefficient between two quantities reaches 0.91. Whereas, in Fig. 3.2.9(b), the MDOC has no clear relation with the DCF length, where the correlation coefficient between them is only 0.16. Thus, the shot-to-shot coherence of the NLP in the ND cavity is determined with only the saturation power of the SA. It clearly shows that the origin of the coherence degradation in the ND NLP regime. The lower

saturation power allows to transmit the more noise components and the transmitted noise participate the intracavity dynamics such as the amplification, dispersion and so on. Thus, regardless of the DCF length, the saturation power of the SA, determining the amount of the transmitted noise components for every RT, is the main factor of the coherence degradation.

# Chapter 4

# Conclusion

Throughout this dissertation, I numerically studied output characteristics of nonlinear fiber laser systems covering both the noncavity configurations and cavity configurations. For the noncavity configurations, by applying the ultrashort pulse to either passive or active HNL-PCFs, I quantitatively analyzed the output SC spectra. For the cavity configurations, I modelled MLFLs where the cavity dispersion is either normal or anomalous. While adjusting the cavity conditions, I numerically verified various QML operation regimes and analyzed the phase stability and cavity nonlinearity.

In the first part of Chapter 2, I numerically investigated the SCG by means of a combinatorial approach amongst a variety of different types of passive-type PCFs and ultrafast fiber lasers for the first time. After making qualitative and quantitative comparisons amongst them, particularly, in terms of the spectral BW, flatness, and degree of spectral coherence, I have eventually reached three main conclusions: (1) With regard to spectral BW, the combination of AD fibers (PCF1-like) and CDS pulses is most desirable. This is mainly caused to the enhanced frequency down-shift acting on the FES due to its higher peak power and shorter pulse width. (2) With

regard to SF and degree of spectral coherence, the combination of FAND fibers (PCF2-like) and Gaussian pulse leads to the best performance. (3) The combination of FAD fibers (PCF3-like) and CS pulse offers a balanced performance in terms of spectral BW, flatness and degree of spectral coherence. This is mainly due to the fact that the inclusion of the RSPs in the CS pulse plays a critical role in the improvement of the SFM by forming new spectral components near the input pulse wavelength. Thus, this combinatorial study has unveiled the most viable options for fine-tuning the characteristics of SC radiation and its dynamics, building upon the existing fiber and fiber laser technologies. I hope that my research presented here will offer a useful guide to the related research and application fields.

In Chapter 2.2, I numerically investigated the SCG in the sub-ps regime through a purposely designed HNL-PCF that can be either in a passive type or in an active type. By comparatively analyzing the SC evolution in temporal and spectral domains, I distinctly verified potential benefits from the addition of the gain effects as following: (1) In the spectral domain, the combined effects of the amplification and nonlinear spectral broadening yield that the formation of the spectral contents near the central wavelength and the spectral broadening of them continuously take place. The repetition of this process contributes the enhancement of the PSD (or ESD) without significant change of the spectral BW. (2) In the temporal domain, the amplification process mitigates the pulse-peak-power depletion due to the ND and SPM. As a result,

the peak power was maintained to be in kW-level that can still induce considerable nonlinear effects, i.e. the nonlinear interaction length was extended over the whole fiber length. Consequently, by exploiting the active HNL-PCF, the SC pulse energy was amplified by 10 dB, while achieving the enhancement of the AESD. Such energy-scaled SC characteristic from the active HNL-PCF is in contrast with the case of another energy-scaling approach in which the pulse is separately amplified before passive HNL-PCF. According to my comparative analysis, the SC BW was substantially increased along the SC energy in the passive case, whereas the SC BW was nearly fixed in the active case, resulting in that the AESD from the active case reached twice of that from the passive case. Thus, if one aims to increase the PSD (or ESD) rather than the increase of the BW, the active HNL-PCF can be an attractive option for the SCG. In addition, as an utilization of the novel characteristics of the active HNL-PCF, I numerically analyzed the amplification of a SC input spectrum. Contrasting to conventional amplifiers that amplify only the spectral contents within the gain BW, the proposed active HNL-PCF enabled the amplification of the SC spectrum over the almost whole spectral range of the incident radiation. Consequently, the incident SC spectrum is amplified by 10 dB without significant degradation of the output BW and the SFM. Emphatically, the results tell me that the active HNL-PCF can be utilized as a broadband amplifier for the external energy-scaling of SC spectra, while overcoming the gain BW limit of conventional amplifiers. Thus, my numerical study discussed the detailed SC

behaviors through the nonlinear fiber amplifier and revealed the potential benefits of the scheme. I believe my research will open new opportunities to enhance the SCG in the sub-ps regime.

In Chapter 3.1, I have numerically studied the multi-pulse dynamics in an AD fiber ring laser cavity. By applying a large amount of gain and loss per RT to the laser cavity, I could make it operate in QML regimes. Adjusting two key cavity parameters of $P_{sat}$ and $L_{SMF}$, I could trigger 5 distinct constitutive QML regimes, which include the incoherent NLP, partially-coherent NLP, symbiotic, partially-coherent MS, and coherent MS regimes. I paid particular attention to analyzing the shot-to-shot stabilities of the QML regimes, in order to figure out the justification and identification of the dynamics and origins of the individual regimes. I found that the generated NLPs could be either incoherent or partially coherent, and that the generated MSs could be either coherent or partially coherent, depending on the cavity conditions parameterized by $P_{sat}$ and $L_{SMF}$. In particular, I numerically clarified and confirmed that the existence of the symbiotic regime recently observed experimentally [18-22], in which NLPs and MSs could coexist stably at the same time. Based on the whole numerical investigations extensively carried out here, I quantified the shot-to-shot coherence characteristics of all the QML regimes in terms of the averaged MDOC, and presented them in a contour map with respect to $P_{sat}$ and $L_{SMF}$. Reinterpreting the contour map, I drew the relationship between the shot-to-shot coherence and the amount of NPS per RT, and verified that both characteristics are strongly

correlated. In addition, I justified the origins of the individual QML regimes in terms of the NPS per RT and the NCD, instead of $P_{sat}$ and $L_{SMF}$, and showed that the NCD plays a very critical role in determining which QML regime the laser cavity would operate in, particularly when the NPS per RT is in an intermediate level, whereas the NPS per RT itself mainly determines the shot-to-shot coherence characteristics, which are all in consistent with the previous, experimental observations [17]. Furthermore, I verified that the symbiotic regime is a 4-way saddle point, on which the QML regimes could evolve and switch into any of the other 4 QML regimes, depending on the degree of the modification of the cavity parameters.

In Chapter 3.2, I have numerically studied the QML dynamics in a ND fiber ring laser cavity. Adjusting two key cavity parameters of $P_{sat}$ and $L_{DCF}$, I demonstrated three distinctive QML regimes, classified into the NLP, transient and symbiotic regimes. In particular, I found that even in the ND cavity, the symbiotic regime exists in which the isolated dissipative solitons copropagate with the NLP packet. For the overall numerical simulation results, I quantified the phase stability and cavity nonlinearity by means of the MDOC and the NPS per RT, respectively. As a result, the relation between the MDOC and the NPS per RT was also valid in the ND cavity. However, unlike the case of the AD cavity, the shot-to-shot stability is mainly determined by only the saturation power of the SA. In this regard, the coherence degradation in the ND cavity is dominated by the amount of the noise contents

transmitting the SA.

To conclude, I investigated nonlinear effects in both types of nonlinear fiber lasers systems by means of numerical simulation: SCG in noncavity configurations and QML operation in cavity configurations. Through these studies, (1) I carried out the optimization of the SCG based on passive PCFs and ultrashort pulses, (2) I verified the potential benefits of utilizing an active-type HNL-PCF for the SCG in the sub-ps regime, (3) I verified the 5 QML regimes and the relation between the shot-to-shot stability and the cavity nonlinearity in an AD fiber ring cavity, and (4) I extended the analysis in the AD cavity to the ND case, in which I verified the 3 QML regimes and discussed the phase-stability in the QML regimes. Thus, I broadened the current research area of the nonlinear fiber laser systems. I believe these studies will help to design various fiber lasers systems and utilize them for the related applications.

# Bibliography


1. R. J. Bates, "Optical switching and networking handbook," (2001).
2. V. Alwayn, "Fiber-optic technologies," Optical Network Design and Implementation (Cisco Press, Indianapolis, IN, 2004) (2004).
3. W. Spillman, D. Patriquin, and D. Crowne, "Fiber optic linear displacement sensor based on a variable period diffraction grating," Appl. Opt. **28**(17), 3550-3553 (1989).
4. K. Okamoto, *Fundamentals of Optical Waveguides*, 2nd ed. (Academic Press, 2006).
5. J. A. Buck, *Fundamentals of Optical Fibers*, 2nd ed. (Wiley, 2004).
6. G. P. Agrawal, *Nonlinear Fiber Optics*, 4th ed. (Academic Press, 2007).
7. http://www.nufern.com/pam/optical_fibers/
8. E. F. Chillcce, E. Rodriguez, O. L. Alves, and C. L. Cesar, "Fabrication of photonic optical fibers from soft glasses," J. Am. Ceram. Soc. **93**(2), 456-460 (2010).
9. H. W. Lee, M. A. Schmidt, R. F. Russell, N. Y. Joly, H. K. Tyagi, P. Uebel, and P. St. J. Russell, "Pressure-assisted melt-filling and optical characterization of Au nano-wires in microstructured fibers," Opt. Express **19**(13), 12180-12189 (2011).
10. B. E. A. Saleh and M. C. Teich, *Fundamentals of Photonics*, 2nd ed. (Wiley, 2007).
11. J. R. Taylor, *Optical Solitons: Theory and Experiment*, 1st ed. (Cambridge University Press, 1992).
12. J. M. Dudley, and J. R. Taylor, *Supercontinuum Generation in Optical Fibers*, 1th ed. (Cambridge University Press, 2010).
13. Y. Kwon, L. A. Vazquez-Zuniga, S. Lee, H. Kim, and Y. Jeong, "Numerical study on multi-pulse dynamics and shot-to-shot coherence property in quasi-mode-locked regimes of a highly-pumped anomalous dispersion fiber ring cavity," Opt. Express 25(4), 4456-4469 (2017).
14. J. W. Nicholson, M. F. Yan, P. Wisk, J. Fleming, F. Dimarcello, E. Monberg, A. Yablon, C. Jørgensen, and T. Veng, "All-fiber, octave-spanning supercontinuum," Opt. Lett. **28**(8), 643-645 (2003).
15. P. H. Pioger, V. Couderc, P. Leproux, and P. A. Champert, "High spectral power density supercontinuum generation in a nonlinear fiber amplifier," Opt. Express, **15**(18), 11358-11363 (2007).
16. R. Song, J. Hou, S. Chen, W. Yang, and Q. Lu, "High power supercontinuum generation in a nonlinear ytterbium-doped fiber amplifier," Opt. Lett., **37**(9), 1529-1531 (2012).
17. C. L. Chang, Y. Y. Lin, P. Y. Lai, Y. Y. Li, S. H. Chen, and S. L. Huang, "High power broadband continuum source based on an all-PM fiber master oscillator nonlinear power amplifier," Laser Phys., **24**(4), 045101 (2014).

18. A. Roy, P. Leproux, P. Roy, J.-L. Auguste, and V. Couderc, "Supercontinuum generation in a nonlinear Yb-doped, double-clad, microstructured fiber," J. Opt. Soc. Am. B, **24**(4), 788-791 (2007).
19. H. Chen, S.-P. Chen, Z.-F. Jiang, and J. Hou, "Enhanced supercontinuum generation in nonlinear Ytterbium-doped fiber amplifier by seeding at short wavelength," IEEE J. Quant. Electron., **51**(11), 6800207 (2015).
20. L. A. V.-Zuniga, X. Feng, Y. Kwon, H. Kim, J. Shi, W. Loh, and Y. Jeong, "W-type highly erbium-doped active soft-glass fibre with high nonlinearity," Electron. Lett., **52**(12), 1047-1048 (2016).
21. J.-H. Lin, Y.-W. Lee, T.-C. Lin, B.-C. Lai, M. Pal, S. Das, A. Dhar, and M. C. Paul, "Near-infrared supercontinuum generation in single-mode nonlinear Yb-doped fiber amplifier," Opt. Express, **22**(13), 16130-16138 (2014).
22. B. Tobias, T. Christopher, N. Bryan, L. F. Andres, H. Peter, "Experimental study of supercontinuum generation in an amplifier based on an Yb3+ doped nonlinear photonic crystal fiber," Proc. SPIE, **9731**, 97310L (2016).
23. Y. Kwon, L. A. V.-Zuniga, K. Park, S. Lee, H. Chang, and Y. Jeong, "Combinatorial study of supercontinuum generation dynamics in photonic crystal fibers pumped by ultrafast fiber lasers," IEEE J. Quant. Electron., **52**(6), 6400311 (2016)
24. K. Shi, P. Li, S. Yin, and Z. Liu, "Chromatic confocal microscopy using supercontinuum light," Opt. Express **12**(10), 2096-2101 (2004).
25. G. Humbert, W. J. Wadsworth, S. G. Leon-Saval, J. C. Knight, T. A. Birks, P. St. J. Russel, M. J. Lederer, D. Kopf, K. Wiesauer, E. I. Breuer, and D. Stifter, "Supercontinuum generation system for optical coherence tomography based on tapered photonic crystal fibre," Opt. Express **14**(4), 1596-1603 (2006).
26. D. J. Jones, S. A. Diddams, J. K. Ranka, A. Stentz, R. S. Windeler, J. L. Hall, and S. T. Cundiff, "Carrier-envelope phase control of femtosecond mode-locked lasers and direct optical frequency synthesis," Sc. **28**(5466), 635-639 (2000).
27. S. V. Smirnov, J. D. Ania-Castanon, T. J. Ellingham, S. M. Kobtsev, S. Kukarin, and S. K. Turitsyn, "Optical spectral broadening and supercontinuum generation in telecom applications," Opt. Fiber Technol. **12**(2), 122-147 (2006).
28. A. Labruyére, A. Tonello, V. Couderc, G. Huss, and P. Leproux, "Compact supercontinuum sources and their biomedical applications," Opt. Fiber Technol. **18**(5), 375-378 (2012).
29. N. K. M. N. Srinivas, S. S. Harsha, and D. N. Rao, "Femtosecond supercontinuum generation in a quadratic nonlinear medium," Opt. Express **13**(9), 3224-3229 (2005).
30. M. Kolesik, E. M. Wright, A. Becker, and J. V. Moloney, "Simulation of third-harmonic and supercontinuum generation for femtosecond pulses in air," Appl. Phys. B **85**(4), 531-538 (2006).

31. J. Liu, H. Schroeder, S. L. Chin, R. Li, and Z. Xu, "Nonlinear propagation of fs laser pulses in liquids and evolution of supercontinuum generation," Opt. Express **13**(25), 10248-10259 (2005).
32. V. P. Kandidov, I. S. Golubtsov, and O. G. Kosareva, "Supercontinuum sources in a high-power femtosecond laser pulse propagating in liquids and gases," Quantum Electron. **34**(4), 348-354 (2004).
33. V. P. Kandidov, I. S. Golubtsov, W. Liu, A. Becker, N. Akozbek, C. M. Bowden, S. L. Chin, and O. G. Kosareva, "Self-transformation of a powerful femtosecond laser pulse into a white-light laser pulse in bulk optical media (or supercontinuum generation)," Appl. Phys. B **77**(2), 149-165 (2003).
34. A. Saliminia, S. L. Chin, and R. Vallée, "Ultra-broad and coherent white light generation in silica glass by focused femtosecond pulses at 1.5 $\mu$m," Opt. Express **13**(15), 5731-5738 (2005).
35. Z. Wang, J. Liu, R. Li, and Z. Xu, "Supercontinuum generation and pulse compression from gas filamentation of femtosecond laser pulses with different durations," Opt. Express **17**(16), 13841-13850 (2009).
36. A. Bozolan, C. J. S. de Matos, C. M. B. Cordeirom E. M. dos Santos, and J. Travers, "Supercontinuum generation in a water-core photonic crystal fiber," Opt. Express **16**(13), 9671-9676 (2008).
37. A. M. Zheltikov, "Let there be white light: supercontinuum generation by ultrashort laser pulses," Physics-Uspekhi **49**(6), 605-628 (2006).
38. L. A. Vazquez-Zuniga, H. S. Kim, Y. Kwon, and Y. Jeong, "Adaptive broadband continuum source at 1200-1400 nm based on an all-fiber dual-wavelength master-oscillator power amplifier and a high-birefringence fiber," Opt. Express **21**(6), 7712-7725 (2013).
39. J. K. Ranka, R. S. Windeler, and A. J. Stentz, "Visible continuum generation in air-silica microstructure optical fibers with anomalous dispersion at 800 nm," Opt. Lett. **25**(1), 25-27 (2000).
40. J. M. Dudley, G. Genty, and S. Coen, "Supercontinuum generation in photonic crystal fiber," Rev. Mod. Phys. **78**(4), 1135-1184 (2006).
41. T. A. Birks, W. J. Wadsworth, and P .St. J. Russell, "Supercontinuum generation in tapered fibers," Opt. Lett. **25**(19), 1415-1417 (2000).
42. B. Kibler, J. M. Dudley, and S. Coen, "Supercontinuum generation and nonlinear pulse propagation in photonic crystal fiber: influence of the frequency-dependent effective mode area," Appl. Phys. B **81**(2), 337-342 (2005).
43. J. M. Dudley, L. Provino, N. Grossard, H. Maillotte, R. S. Windeler, B. J. Eggleton, and S. Coen, "Supercontinuum generation in air-silica microstructured fibers with nanosecond and femtosecond pulse pumping," J. Opt. Soc. Am. B **19**(4), 765-771 (2002).
44. G. Genty, S. Coen, and J. M. Dudley, "Fiber supercontinuum sources," J. Opt. Soc. Am. B **24**(8), 1771-1785 (2007).

45. T. Schreiber, J. Limpert, H. Zellmer, A. Tünnermann, and K. P. Hansen, "High average power supercontinuum generation in photonic crystal fibers," Opt. Commun. **228**, 71–78 (2003).
46. Y. Kwon, L. A. Vazquez–Zuniga, S. Hong, H. Kim, and Y. Jeong, "Numerical study on fiber based supercontinuum generation in anomalous dispersion pumping regimes," CLEO PR 2013, Kyoto, Japan, 30 Jun–4 Jul, 2013.
47. P. Falk, M. H. Frosz, and O. Bang, "Supercontinuum generation in a photonic crystal fiber with two zero–dispersion wavelengths tapered to normal dispersion at all wavelengths," Opt. Express **13**(19), 7535–7540 (2005).
48. K. M. Hilligsøe, T. V. Anderson, H. N. Paulsen, C. K. Nielsen, K. Mølmer, S. Keiding, R. Kristiansen, K. P. Hansen, and J. J. Larsen, "Supercontinuum generation in a photonic crystal fiber with two zero dispersion wavelengths," Opt. Express **12**(6), 1045–1054 (2004).
49. A. M. Heidt, "Pulse preserving flat–top supercontinuum generation in all–normal dispersion photonic crystal fibers," J. Opt. Soc. Am. B **27**(3), 550–559 (2010).
50. L. E. Hooper, P. J. Mosley, A. C. Muir, W. J. Wadsworth, and J. C. Knight, "Coherent supercontinuum generation in photonic crystal fiber with all–normal group velocity dispersion," Opt. Express **19**(6), 4902–4907 (2011).
51. M. L. V. Tse, P. Horak, F. Poletti, N. G. R. Broderick, J. H. V. Price, J. R. Hayes, and D. J. Richardson, "Supercontinuum generation at 1.06 $\mu$m in holey fibers with dispersion flattened profiles," Opt. Express **14**(10), 4445–4451 (2006).
52. P. St. J. Russell, "Photonic–crystal fibers," IEEE J. Lightwave Technol. **24**(12), 4729–4749 (2006).
53. L. E. Nelson, D. J. Jones, K. Tamura, H. A. Haus, E. P. Ippen, "Ultrashort–pulse fiber ring lasers," Appl. Phys. B **65**(2), 277–294 (1997).
54. M. Matsumoto, "Theory of stretched–pulse transmission in dispersion–managed fibers," Opt. Lett. **22**(16), 1238–1240 (1997).
55. F. Ö. Ilday, J. R. Buckley, W. G. Clark, and F. W. Wise, "Self–similar evolution of parabolic pulses in a laser," Phys. Rev. Lett. **92**, 213902 (2004).
56. V. I. Kruglov, A. C. Peacock, J. D. Harvey, and J. M. Dudley, "Self–similar propagation of parabolic pulses in normal–dispersion fiber amplifiers," J. Opt. Soc. Am. B **19**(3), 461–469 (2002).
57. F. W. Wise, A. Chong, and W. H. Renninger, "High–energy femtosecond fiber lasers based on pulse propagation at normal dispersion," Laser & Photon. Rev. **2**, 58–73 (2008).
58. W. H. Renninger, A. Chong, and F. W. Wise, "Dissipative solitons in normal–dispersion fiber lasers," Phys. Rev. Lett. A **77**, 023814 (2008).
59. L. A. Vazquez–Zuniga and Y. Jeong, "Super–broadband noise–like pulse erbium–doped fiber ring laser with a highly nonlinear fiber

for Raman gain enhancement," IEEE Photon. Technol. Lett. **24**(17), 1549-1551 (2012).
60. Y. Jeong, L. A. Vazquez-Zuniga, S. Lee, and Y. Kwon, "On the formation of noise-like pulses in fiber ring cavity configurations," Opt. Fiber Technol. **20**(6), 575-592 (2014).
61. L. A. Vazquez-Zuniga and Y. Jeong, "Wavelength-tunable, passively mode-locked erbium-doped fiber master-oscillator incorporating a semiconductor saturable absorber mirror," J. Opt. Soc. Kor. **17**(2), 117-129, (2013).
62. D. Lorenc, D. Velic, A. N. Markevitch, and R. J. Levis, "Adaptive femtosecond pulse shaping to control supercontinuum generation in a microstructure fiber," Opt. Communications **276**(2), 288-292 (2007).
63. S. Xu, D. H. Reitze, and R. S. Windeler, "Controlling nonlinear process in microstructured fibers using shaped pulses," Opt. Express **12**(20), 4731-4741 (2004).
64. C. Ament, P. Polynkin, and J. V. Moloney, "Supercontinuum generation with femtosecond self-healing Airy pulses," Phys. Rev. Lett. **107**, 243901 (2011).
65. http://www.nktphotonics.com/files/files/NL-1050-NEG-1.pdf
66. http://www.nktphotonics.com/files/files/NL-1050-ZERO-2.pdf
67. C. Liu, E. J. Rees, T. Laurila, S. Jian, and C. F. Kaminski, "Periodic interactions between solitons and dispersive waves during the generation of non-coherent supercontinuum radiation," Opt. Express **20**(6), 6316-6324 (2012).
68. W. J. Tomlinson, R. H. Stolen, and A. M. Johnson, "Optical wave breaking of pulses in nonlinear optical fibers," Opt. Letters **10**(9), 457-459 (1958).
69. G. P. Agrawal, "Temporal and spectral effects of cross-phase modulation on copropagating ultrashort pulses in optical fibers," Phys. Rev. A **40**, 5063-5072 (1989).
70. J. Hansryd, P. A. Andrekson, M. Westlund, J. Li, and P.-O. Hedekvist, "Fiber-based optical parametric amplifiers and their applications," IEEE J. Sel. Topics Quantum Electron. **8**(3), 506-520 (2002).
71. M. H. Frosz, P. Falk, and O. Bang, "The role of the second zero-dispersion wavelength in generation of supercontinua and bright-bright soliton-pairs across the zero-dispersion wavelength," Opt. Express **13**(16), 6181-6192 (2005).
72. S. Dubnov, "Generalization of spectral flatness measure for non-Gaussian linear processes," IEEE Sig. Proc. Letters **11**(8), 698-701 (2004).
73. G. A. Nowak, J. Kim, and M. N. Islam, "Stable supercontinuum generation in short lengths of conventional dispersion-shifted fiber," Appl. Opt., **38**(6), 7364-7369 (1999).
74. J. C. Travers, W. Chang, J. Nold, N. Y. Joly, P. S. J. Russsell, "Ultrafast nonlinear optics in gas-filled hollow-core photonic crystal fibers," J. Opt. Soc. Am. B, **28**(12), A11-A26 (2011).

75. V. V. R. K. Kumar, A. K. George, W. H. Reeves, J. C. Knight, P. S. J. Russell, F. G. Omenetto, and A. J. Taylor, "Extruded soft glass photonic crystal fiber for ultrabroad supercontinuum generation," Opt. Express, **10**(5), 1520–1525 (2002).
76. M. A. Foster, J. M. Dudley, B. Kibler, Q. Cao, D. Lee, R. Trebino, and A. L. Gaeta, "Nonlinear pulse propagation and supercontinuum generation in photonic nanowires: experiment and simulation," Appl. Phys. B, **81**(2), 363–367 (2005).
77. G. P. Agrawal, *Applications of Nonlinear Fiber Optics*, 1st ed. (Academic Press, 2001).
78. D. J. Richardson, J. Nilsson, and W. A. Clarkson, "High power fiber lasers: current status and future perspectives," J. Opt. Soc. Am. B, **27**(11), B63–B92 (2010).
79. C. A. Codemard, J. K. Sahu, and J. Nilsson, "Tandem cladding-pumping for control of excess gain in ytterbium-doped fiber amplifiers," IEEE J. Quant. Electron., **46**(12), 1860–1869 (2010).
80. M. Olivier and M. Piché, "Vector similariton erbium-doped all-fiber laser generating sub-100-fs nJ pulses at 100 MHz," Opt. Express, **24**(3), 2336–2349 (2016).
81. L. Shah and M. E. Fermann, "High power femtosecond fiber chirped pulse amplification system for high speed micromachining," J. Laser Micro/nanoeng. **1**(3), 176–180 (2006).
82. H. Lim, Y. Jiang, Y. Wang, Y.-C. Huang, Z. Chen, and F. W. Wise, "Ultrahigh-resolution optical coherence tomography with a fiber laser source at 1 $\mu$m," Opt. Lett. **30**(10), 1171–1173 (2005).
83. T. R. Schibli, K. Minoshima, F.-L. Hong, H. Inaba, A. Onae, H. Matsumoto, I. Hartl, and M. E. Fermann, "Frequency metrology with a turnkey all-fiber system," Opt. Lett. **29**(21), 2467–2469 (2004).
84. J. R. Unruh, E. S. Price, R. G. Molla, L. S.-Bittel, C. K. Johnson, and R. Hui, "Two-photon microscopy with wavelength switchable fiber laser excitation," Opt. Express **14**(21), 9825-9831 (2006).
85. J. Clowes, "Next generation light sources for biomedical applications," Optik & Photonic. **3**(1), 36–38 (2008).
86. N. Nishizawa and J. Takayanagi, "Octave spanning high-quality supercontinuum generation in all-fiber system," J. Opt. Soc. Am. B **24**(8), 1786–1792 (2007).
87. M. E. Fermann and I. Hartl, "Ultrafast fiber lasers," Nat. Photonics **7**, 868–874 (2013).
88. A. Komarov, H. Leblond, and F. Sanchez, "Multistability and hysteresis phenomena in passively mode-locked fiber lasers," Phys. Rev. A **71**(5), 053809 (2005).
89. S. Chouli and P. Grelu, "Soliton rains in a fiber laser: An experimental study," Phys. Rev. A **81**(6), 063829 (2010).
90. J. M. S.-Crespo, Ph. Grelu, and N. Akhmediev, "Dissipative rogue waves: Extreme pulses generated by passively mode-locked lasers," Phys. Rev. E **84**(1), 016604 (2011).

91. M. Horowitz, Y. Barad, and Y. Silberberg, "Noiselike pulses with a broadband spectrum generated from an erbium-doped fiber laser," Opt. Lett. **22**(1), 799-801 (1997).
92. D. Y. Tang, L. M. Zhao, and B. Zhao, "Soliton collapse and bunched noise-like pulse generation in a passively mode-locked fiber ring laser," Opt. Express **13**(7), 2289-2294 (2005).
93. S. Smirnov, S. Kobtsev, S. Kukarin, and A. Ivanenko, "Three key regimes of single pulse generation per round trip of all-normal-dispersion fiber lasers mode-locked with nonlinear polarization rotation," Opt. Express **20**(24), 27447-27453 (2012).
94. L. M. Zhao, D. Y. Tang, T. H. Cheng, H. Y. Tam, and C. Lu, "120 nm bandwidth noise-like pulse generation in an erbium-doped fiber laser," Opt. commun. **281**(1), 157-161 (2008).
95. D. V. Churkin, S. Sugavanam, N. Tarasov, S. Khorev, S. V. mirnov, S. M. Kobtsev, and S. K. Turitsyn, "Stochasticity, periodicity and localized light structures in partially mode-locked fibre lasers," Nat. Commun. **6**, 1-6 (2015).
96. H. S.-Hernandez, O. Pottiez, M. D.-Sanchez, R. I. A.-Tamayo, J. P. L.-Cruz, J. C. H.-Garcia, B. I.-Escamilla, and E. A. Kuzin, "Dynamics of noise-like pulsing at sub-ns scale in a passively mode-locked fiber laser," Opt. Express **23**(15), 18840-18849 (2015).
97. Y. Kwon, S. Lee, L. A. V.-Zuniga, H. Chang, K. Park, and Y. Jeong, "Temporal dynamics and shot-to-shot stability characteristics of three distinctive partially-mode-locked operation regimes in a fiber ring cavity," ASSL 2016, Boston, USA, 30 Oct.-3 Nov., 2016, paper AM5A.14.
98. Y.-Q. Huang, Z.-A. Hu, Z.-C. Luo, A.-P. Luo, and W.-C. Xu, "Coexistence of harmonic soliton molecules and rectangular noise-like pulses in a figure-eight fiber laser," Opt. Lett. **41**(17), 4056-4059 (2016).
99. Y. E. B.-Rodriguez, O. Pottiez, E. G. Sánchez, J. L.-Cruz, H. I.-Villalón, J. C. H.-Garcia, M. B.-Jimenez, G. B. Pérez, B. I.-Escamilla, and E. Kuzin, "Dual noise-like pulse and soliton operation of a fiber ring cavity," J. Opt. (in press).
100. A. F. J. Runge, C. Aguergaray, N. G. R. Broderick, and M. Erkintalo, "Coherence and shot-to-shot spectral fluctuations in noise-like ultrafast fiber lasers," Opt. Lett. **38**(21), 4327-4330 (2013).
101. L. Gao, T. Zhu, S. Wabnitz, M. Liu, and W. Huang, "Coherence loss of partially mode-locked fibre laser," Sci. Rep. **6**, 24995 (2016).
102. Z. Cheng, H. Li, and P. Wang, "Simulation of generation of dissipative soliton, dissipative soliton resonance and noise-like pulse in Yb-doped mode-locked fiber lasers," Opt. Express **23**(5), 5972-5981 (2015).
103. D. Y. Tang, B. Zhao, L. M. Zhao, and H. Y. Tam, "Soliton interaction in a fiber ring laser," Phys. Rev. E **72**(1), 016616 (2005).
104. D. E. Pelinovsky, V. V. Afanasjev, and Y. S. Kivshar, "Nonlinear theory of oscillating, decaying, and collapsing solitons in the generalized

nonlinear schrödinger equation," Phys. Rev. E **53**(2), 1940–1953 (1996).
105. A. I. Chernykh and S. K. Turitsyn, "Soliton collapse regimes of pulse generation in passively mode–locking laser systems," Opt. Lett. **20**(4), 398–400 (1995).
106. R. D. Yates and D. J. Goodman, *Probability and Stochastic Process*, 2nd ed. (Wiley, 2005).
107. K. Park and Y. Jeong, "A quasi–mode interpretation of acoustic radiation modes for analyzing Brillouin gain spectra of acoustically antiguiding optical fibers," Opt. Express **22**(5), 7932–7946, (2014).

# 한글 초록

본 논문은 초단 펄스 영역에서 비선형 광섬유 레이저 시스템의 수치 해석 연구를 다룬다. 본 논문에서 다루는 비선형 광섬유 레이저 시스템은 크게 비공진기 시스템 (noncavity system)과 공진기 시스템 (cavity system)으로 나눌 수 있다. 전자에서 비선형성이 충분히 증대될 경우 광대역 스펙트럼을 형성하는 소위 슈퍼컨티늄 발진 (supercontinuum generation, SCG) 현상이 야기되며, 후자에서 비선형성이 증대될 경우 다중 펄스를 발진하는 준모드잠금 (quasi-mode-locked, QML) 동작이 야기된다. 본 논문은 비선형 슈뢰딩거 방정식에 기반한 모델링을 통해 두 유형의 비선형 광섬유 레이저 시스템에 대한 대한 수치 해석을 수행한다. 수치 해석 결과를 분석해, 본 저자는 시스템의 성능의 최적화 및 시스템 디자인의 가이드를 제공하고자 한다.

논문의 첫 부분에서는 비공진기 구조 시스템에서 발생하는 SCG에 대한 연구를 다룬다. 먼저 본 저자는 현 기술이 제공하는 초단 광섬유 레이저 펄스와 광결정형 광섬유 (photonic crystal fiber, PCF)의 다양한 조합에 따른 SCG을 수치해석을 수행한다. 본 연구를 위해 세 유형의 PCF와 4 유형의 초단 광펄스가 고려된다. 이를 통한 12 종의 조합에 대한 SCG이 수치해석 된다. 또한 12 종의 SC 출력에 대해 본 저자는 스펙트럴 대역폭, 스펙트럴 평평도 (flatness), 코히런스를 기준으로 성능을 정량화하고, 차트를 구성한다. 본 연구를 통해, 저자는 가장 다양한 목적에 맞게 유리한 광결정형 광섬유와 초단 광펄스의 조합을 제안한다.

논문의 두 번째 부분에서 저자는 초단 펄스 영역에서 이터븀첨가

고비선형 PCF를 이용한 SCG을 논한다. 기존의 수동형 광섬유와 비교해, 본 저자는 제안된 능동형 광섬유를 통해 에너지 스펙트럴 밀도의 향상 및 펄스 첨두 출력의 회복에 기반한 향상된 SCG을 수치해석적으로 시연한다. 또한 제안된 고비선형 능동형 PCF를 활용해, SC 입력 스펙트럼을 대역폭과 평평도의 저하를 수반하지 않고, 10−dB만큼 에너지를 증폭할 수 있음을 보인다. 해당 수치해석 결과는 초단 펄스 영역에서 SCG 분야의 새로운 지평을 열 것으로 기대된다.

다음으로 본 논문은 공진기 구조의 비선형 현상에 대해 다룬다. 먼저 저자는 비이상 분산 (anomalous dispersion, AD) 광섬유 링 공진기에서 QML 동작에 대한 수치 해석을 수행한다. 저자는 포화 흡수체 (saturable absorber, SA)의 포화 출력과 수동형 광섬유의 길이에 따라 다양한 QML 동작 영역이 5 유형으로 구분될 수 있음을 보인다. 특히 저자는 유사 잡음 펄스 (noise−like pulse, NLP)와 다수의 솔리톤이 공존하는 공생 체제 (symbiotic regime)을 수치해석적으로 입증한다. 나아가 각 QML 동작 영역에서 공진기의 비선형성에 대한 코히런스 특성을 분석하고 정량적인 관계를 입증한다. 또한 저자는 공진기의 분산 정도에 따라 부분적으로 코히런트한 세 QML 동작 영역이 구분될 수 있음을 보인다. 저자는 모든 수치해석 결과는 등고도를 통해 시각화하며, 이는 복잡한 QML 동작을 해석하고 논하는데 유용할 것으로 기대된다.

본 논문의 네 번째 부분에서, 저자는 AD 공진기에서 수행한 연구를 정상 분산 (normal dispersion, ND) 공진기에 대해 확장한다. SA의 포화 출력 및 수동형 광섬유 길이를 조절하며, 저자는 ND 공진기에서 세 유형의 QML 동작 영역을 수치해석적으로 보인다. 각 동작 영역에서 저자는 QML 펄스의 코히런스 특성과 공진기의 비선형성에 대한 관계를 분석하고, 이를 등고도를 통해 시각화한다. 나아가 ND QML 공진기에서

코히런스의 저하에 대한 원인을 논의한다.

주요어: 비선형 광학, 광섬유 레이저, 극초단 펄스, 광섬유 증폭기, 모드잠금 레이저

학 번: 2011-20791